UNIVERSITÀ DI PARMA

UNIVERSITA' DEGLI STUDI DI PARMA

DOTTORATO DI RICERCA IN
Scienza e Tecnologia dei Materiali

Ciclo XXXII

Sintering and characterization of high hardness/ high toughness/ high entropy structural ceramics for severe environments

Coordinatore:
Chiar.mo Prof. Enrico Dalcanale

Tutor:
Dott.ssa Diletta Sciti

Dottorando: Simone Failla

Anni 2016-2019

TABLE OF CONTENTS

Abstract

High-Tech ceramics offer a variety of outstanding physical and mechanical properties but their behavior critically depend on the thermal treatments that consolidate their microstructure. Sintering of highly refractory ceramics is usually carried out at very high-temperature and application of mechanical pressures to obtain density close to the theoretical one. This limits their widespread application due to limitation in size and shape and excessive costs of production.

The aim of this work is the achievement of bulk and composite materials characterized by **high hardness**, **high toughness** and **high entropy** values that can be efficiently sintered by different sintering techniques such as: hot pressing, pressureless sintering, gas pressure sintering or arc-melting.

Materials under study include:

- B_4C and B_4C-based composites, a class of ultra-hard materials specifically suited for ballistic applications.
- Fiber-reinforced composites ceramic materials (UHT-CMC), a class of damage tolerant materials specifically suited for aerospace application.
- Ultra high temperature ceramics (UHTC) with high entropy structure a novel class of advanced structural ceramic materials specifically suited for harsh environment.

The PhD activity was divided into three parts:

- The first part was focused on the development and characterization of light weight bulk material for the fabrication of ballistic protection systems. Sintering additives or others agents (α-SiC, nano-SiC, Si_3N_4, TiO_2, WC) are used to improve the densification with conventional methods, avoiding if possible the application of mechanical pressure. In particular B_4C-TiB_2 composites were contaminated with WC to study the effect on densification, microstructure and properties. WC was introduced through a mild or a high energy milling with WC-6 wt% Co spheres or directly as sintering aid to 50 v% B_4C / 50 v% TiB_2 mixtures. High energy milling was very effective in improving the densification thanks to the synergistic action of WC impurities, acting as sintering aid, and size reduction of the starting B_4C-TiB_2 powders. As a result, the sintering temperature necessary for full densification decreased to 1860 °C and both strength and hardness benefited from the microstructure refinement, 860 ± 40 MPa and 28.5 ± 1.4

GPa respectively. High energy milling was then adopted for producing mixture of B_4C-TiB_2 that spanning from 100 v% B_4C and 100 v% TiB_2 studying the effect of different sintering technique such as hot pressing, pressureless sintering and gas pressure sintering. The B_4C-rich composition showed the highest hardness and strength value in all sintering technique ~30 GPa and ~800 MPa respectively whilst the TiB_2-rich composition showed the highest value of toughness, ~5 $MPa \cdot m^{0.5}$.

- The second part of this thesis was focused on fabrication of ultra-high temperature ceramic composites (UHT-CMCs) observing the influence of different coatings on carbon fibers through electrophoretic deposition technique.
Different configurations of continuous carbon fiber-reinforced ultrahigh temperature ceramics (UHTCs), by combining coatings and matrix, were produced via electrophoretic deposition (EPD) and slurry infiltration. The toughening of non-periodic fiber distribution induced by the EPD process was investigated through work of fracture analysis. The results show that a non-periodic fiber distribution results in toughness increase from 8 $MPa \cdot m^{0.5}$ to 11 $MPa \cdot m^{0.5}$ with respect to a periodic fiber distribution. This toughness improvement does not strongly affect the flexural strength, which is mainly related to the fiber volumetric amount. It is shown that the assembling of carbon fibers into bundles (i.e. by dispersing the fibers with a non-periodic distribution) increases the crack propagation energy dissipated on the crack-wake from 0.5 kJ/m^2 to 1 kJ/m^2, which can be mainly ascribed to the fiber/bundle pull-out. On the other hand, the energy dissipated on the crack-tip (as fiber/matrix debonding) is fiber distribution-independent and increases from 0.3 kJ/m^2 to 0.4 kJ/m^2 with increasing the fiber amount from 33 vol% to 40 vol%. Finally, work of fracture (WoF) analysis is proposed as test to evaluate pull-out toughening instead of push-in and push-out tests.

- The third part of this thesis was focused on the production of High entropy metal diboride (HEMB). This novel class of ceramic materials represent a radically new approach to extend the chemical composition window of ultra-high temperature ceramics (UHTCs). In this work, arc-melting was used to produce dense HEMBs starting from UHTC powders. In order to understand the influence of each individual diboride within the quinary system (HfB_2, ZrB_2, TiB_2, TaB_2 and CrB_2), we investigated five quaternary equimolar solid solutions *e.g.* Hf-Zr-Ti-Ta, Hf-Zr-Ti-Cr, Hf-Zr-Ta-Cr, Hf-Ti-Ta-Cr, Zr-Ti-Ta-Cr and the overall quinary equimolar combination. Arc-melting allowed a rapid screening of favorable and unfavorable combinations. The produced

HEMBs were free from undesired oxides and characterized by linear variation of lattice parameters typical of diborides and binary solid solutions. Because of evaporation during arc melting, CrB_2 was hardly found in the solid solution, suggesting that vapor pressure should be taken into account when designing HEMB compositions especially for operating temperatures exceeding 2000 °C. Finally, Vickers microhardness ranged between the typical values of starting diborides.

1. Introduction

Research in "*advanced ceramic materials*" sector has recently taken on an important role in the field of materials science and technology, occupying a position of absolute importance in the context of the relative industrial production. While on the one hand this activity was based on the development of new applications, on the other it necessarily led to the evolution of existing products in subsequent generations with ever better performance. In this context, it is significant to underline how technical development has always been linked to a simultaneous progress in the sectors that are part of materials science and technology. Along with engineering problems, the need to identify and design materials and their structure in relation to the specific application for which they are destined has soon become essential. This approach led to definition of new classes of materials, generally referred to as advanced materials. Based on the combination or coupling of two or more fundamental elements in highly controlled structures and stoichiometry, advanced ceramic materials exhibit much higher properties and characteristics than conventional materials. Among these, it is useful to remember for example ultra-high temperature ceramics (UHTCs) and ceramic matrix composites (CMCs), which represent a wide class of materials particularly important for the high tech application. The high mechanical properties and the ability to withstand high temperatures make them suitable for use as structural materials in aerospace field and military applications. Their use allows a good reduction of the structural weight and, in some cases, makes it possible to design complex shape. For these reasons, "*advanced ceramic materials*" are used also in other industrial sectors such as: transport, energy, communications, biotechnology, chemical and metallurgical industry, electrical and mechanical engineering industry. However, large scale production in the industrial sector is made difficult by the high costs associated both with the starting materials and the characteristics of the processes for obtaining the final product. The reduction of production costs of advanced materials, to reach levels comparable with those of the production of conventional materials, is therefore one of the main objectives to be achieved for their full exploitation. For this reason, with the study of the properties of these materials it is necessary to develop appropriate technologies and synthesis processes.

Advanced ceramics can be **oxides** or **non-oxides**. Depending on performance, advanced ceramics can be divided into two large groups:

- **functional ceramic materials:** electro-ceramics, ceramics with magnetic function, bio-ceramics, ceramics with chemical functions, ceramics with optical functions, ceramics with thermal functions, ceramics with nuclear functions
- **structural ceramic materials:** thermomechanical ceramics, wear-resistant ceramics, bullet-proof armor plates.

The aim of this thesis is the development of three different **advanced non-oxide structural ceramics**, respectively, characterized by (i) high hardness, (ii) high toughness and (iii) high entropy properties. Their characteristics depending: on function required, on the compounds, the starting compositions and the introduction of suitable reinforcements, on the reactions that may occur during the process to form specific solid solutions, on the desired lattice alterations of crystal structure. In particular, for composites, the reinforcement components, in the form of particles and/or fibers, can induce microstructural characteristics suitable to satisfy structural and functional performance at the same time. The microstructure of the material of interest is a function of the type of the proposed use (distribution and grain size, porosity size and flaws). The achievement of complex microstructures, capable of conferring superior properties, require the setting up and control of the processes. In fact, ceramic materials retain the memory of the microstructural evolution that follows from the various stages of the process (mixing, grinding, forming, sintering). Innovation in ceramic materials is carried out through the process innovation. The studied materials are summarized in the following:

i. **[High hardness structural ceramics]**

   In the first section the effect of appropriate quantities of sintering additives in a B_4C-TiB_2 matrix were investigated. It was explored the effect of WC addition studying different processing methods using hot pressing as a consolidation method in order to obtain the best densification and optimized microstructural features. After that, was selected the most promising process and was investigated the dependence of properties on the material composition, spanning from B_4C-rich compositions to TiB_2-rich compositions studying different sintering technique such as hot pressing, pressureless sintering and gas pressure sintering.

ii. **[High toughness structural ceramics]**

In the second section the fabrication and characterization of continuous fibre reinforced ultra-high temperature ceramics (UHT-CMC) by electrophoretic deposition (EPD) to produce ZrB_2 and TiB_2 coatings on carbon fabrics was studied. The mechanical properties of the final components are investigated and compared to a similar UHT-CMCs in terms of fiber volume content and porosity, but characterized by uniformly distributed carbon fibers without coating.

iii. **[High entropy structural ceramics]**

In the third section was demonstrate the formation of high entropy borides (HEB), mixing equimolar composition of HfB_2, ZrB_2, TiB_2, TaB_2 and CrB_2, through the arc-melting technique. Six compositions (one quinary and five quaternaries) have been prepared to study the effect of each single boride on the formation of HEB solid solution.

This work was carried out at the National Research Council - Institute of Science and Technology for Ceramics (CNR - ISTEC) in Faenza. The high entropy borides activity was carried out at “Southwest Jiaotong University” at Chengdu (China).

The results obtained during the PhD activity have also been published and/or presented at international conferences:

PEER-REVIEWED ARTICLES

1. Galizia, P., **Failla, S.**, Zoli, L. & Sciti, D. Tough salami-inspired Cf/ZrB_2 UHTCMCs produced by electrophoretic deposition. *J. Eur. Ceram. Soc.* **38**, 403–409 (2018).

2. Silvestroni, L., **Failla, S.**, Neshpor, I. & Grigoriev, O. Method to improve the oxidation resistance of ZrB2 -based ceramics for reusable space systems. *J. Eur. Ceram. Soc.* **38**, 2467–2476 (2018).

3. Monteverde, F., Melandri, C., **Failla, S.**, Grohsmeyer, R.J., Hilmas, G.E. & Fahrenoholtz, W. G. Escape from the strength-to-toughness paradox: Bulk ceramics through dual composite architectures. *J. Eur. Ceram. Soc.* **38**, 2961–2970 (2018).

4. **Failla, S.**, Melandri, C., Zoli, L., Zucca, G. & Sciti, D. Hard and easy sinterable B_4C-TiB_2 -based composites doped with WC. *Journal of the European Ceramic Society* **38**, (Elsevier, 2018).

5. Silvestroni, L., **Failla, S.**, Vinokurov, V., Neshpor, I. & Grigoriev, O. Core-shell structure: An effective feature for strengthening ZrB2 ceramics. *Scr. Mater.* **160**, 1–4 (2019).
6. **Failla, S.**, Galizia, P., Zoli, L., Vinci, A. & Sciti, D. Toughening effect of non-periodic fiber distribution on crack propagation energy of UHTC composites. *J. Alloys Compd.* **777**, 612–618 (2019).
7. Silvestroni, L., Vinci, A., **Failla, S.**, Zoli, L., Rubio, V., Binner, J. & Sciti, D. Ablation behaviour of ultra-high temperature ceramic matrix composites: role of MeSi2 addition. *J. Eur. Ceram. Soc.* **39**, 2771–2781 (2019).
8. Sani, E., **Failla, S.** & Sciti, D. Dark alumina for novel solar receivers. *Scr. Mater.* **176**, 58–62 (2020).

9. **Failla, S.**, Galizia, P., Fu, S., Grasso, S. & Sciti, D. Formation of high entropy metal diborides using arc-melting and combinatorial approach to study quinary and quaternary solid solutions. *J. Eur. Ceram. Soc. (in press).*

ORAL PRESENTATIONS

1. **S. Failla,** P. Galizia, S. Fu, S. Grasso, D. Sciti; "Observing the formation of high entropy metal diborides and studying the influence of single boride in the solid solution using arc-melting as consolidation technique" 10th International conference on High Temperature Ceramic Matrix Composites (HT-CMC), Bordeaux, France, September 22-26, 2019
2. **S. Failla**, L. Zoli, D. Sciti; "Studying the incorporation of WC to make B_4C-TiB_2 system more interesting for armour applications" 43th International Conference & Exposition on Advanced Ceramics & Composites (ICACC), Daytona Beach, Florida, January 28–February 01, 2019
3. **S. Failla**, L. Zoli, P. Galizia, D. Sciti; "Novel UD UHTCMCs Produced by EPD and Sintering" 14th International Ceramics Congress (CIMTEC), Perugia, Italy, June 4-8, 2018

POSTER

1. **S. Failla**, L. Zoli, P. Galizia, A. Vinci, D. Sciti: " Electrophoretic deposition of ZrB_2 and TiB_2 on carbon fibers: A process for novel UD UHTCMCs", 69th Annual Meeting of International Society of Electrochemistry, September 2-7 2018, Bologna, Italy
2. **S. Failla**, L. Zoli, P. Galizia, D. Sciti: " Electrophoretic deposition of dispersion of ZrB_2 and SiC powders on woven carbon fibers for the processing of novel UHTCMCs", ECerS 2017 15th Conference & Exhibition of the European Ceramic Society July 9-13, 2017/ Budapest, Hungary
3. **S. Failla**, C. Baldisserri, A. Costa, A. Vinci, D. Sciti: " Electrophoretic deposition of dispersion ZrB_2 and SiC powder on woven carbon fiber for the processing of novel UHTCMCs", Materials.it, Materials Science and Technology, Aci Castello (CT) Italy, December 12 - 16, 2016

2. State of the art

2.1 High hardness structural ceramics for ballistic application

Due to the many wars occurred throughout history, man has had great interest to find protection systems to defend himself against various weapons threats. It can be said that the evolution of weapons over the centuries has been carried out together with the evolution of protection systems such as armor or shields. For example, just think of the role of the heavy metal armor of medieval knights who had to defend themselves from swords and arrows compared to light armor made of composite material for the policemen who must defend themselves from gun bullets. The fundamental properties for the production of materials for new defense protection systems are to possess high mechanical properties and to be as lightweight as possible.

The challenge in this field of research is not only to identify the most appropriate materials for this application, but also to find a more economical process in terms of production and time to perform all the necessary analyzes to identify the actual efficiency of the final product. One of the most direct and expensive methods for studying ballistic protection systems can be described as "build it, shoot it and look at it"[1]. When referring to a modern armor, we have to refer to a complex structure of different assembled materials with a very specific configuration. The properties and the assembly of the materials used for the ballistic structure depend mainly on how the armor is to be used. Currently there is no exact correlation between the properties and the behavior that a material must have for a ballistic protection system. What is now established is that high hardness and high Young's modulus are often one of several indicator of good ballistic performance.

One of the most direct methods to understand if a reinforcement is suitable as ballistic protection is the measure of the penetration, partial or total, by a threat. This test and other all specific features that an armor have to possess to be classified according to the threat from which it is struck, are described extensively by the standard techniques established by the National Institute of Justice (NIJ) [2]. Table 2.1 shows the ballistic protection levels of the NIJ standards.

Table 2.1 National Institute of Justice (NIJ) Ballistic threat standards[2]

Level	Projectile	Weight, g	Velocity, m/s	Kinetic Energy (Relative to Type IIA)
Type IIA	9 mm full metal-jacketed round nose (FMJ RN) .40 S&W FMJ	8.0 11.7	373 ± 9.1 352 ± 9.1	1.0 1.3
Type II	9 mm FMJ RN .357 magnum jacketed soft point (JSP)	8.0 10.2	398 ± 9.1 436 ± 9.1	1.1 1.7
Type IIIA	.357 SIG FMJ flat nose (FN). 44 magnum semijacketed hollow point (SJHP)	8.1 15.6	448 ± 9.1 436 ± 9.1	1.5 2.7
Type III (rifles)	7.62 mm FMJ, steel jacketed bullets (U. S. military designation M80)	9.6	847 ± 9.1	6.2
Type IV (armor-piercing rifles)	.30 caliber armor-piercing (AP) bullets (U.S. military designation M2 AP)	10.8	878 ± 9.1	7.5

The first three levels- IIA, II e IIIA - are usually soft armor. The two remaining levels, III and IV, are generally hard armors. The Fig 2.1 shows the different type of bullet associated with the corresponding NIJ level. Even the material of which the bullet is made helps to design the ballistic protections. In general, when a projectile has a high hardness and high density it is necessary to use a panel of hard ceramic material in order to break the bullet during the impact.

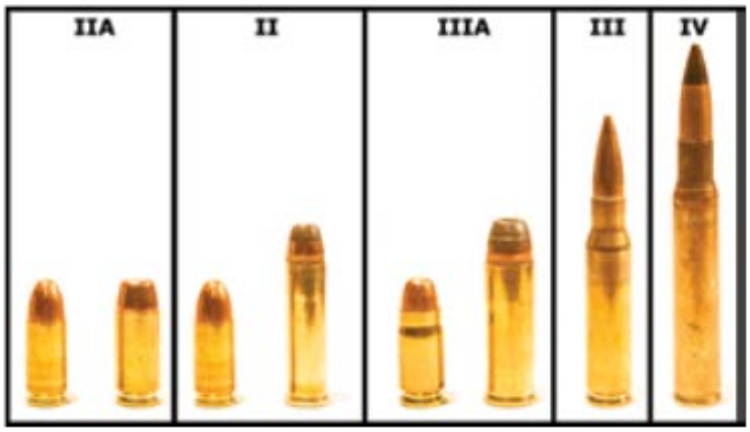

Figure 2.1 Type IIA: 9mm FMJ RN; 40 Smith and Wesson (S&W) FMJ; Type II: 9mm FMJ RN; 357Magnum JSP.; Type IIIA: 357 SIGFMJ FN; 44 Magnum SJHP; Type III: 7.62mm FMJ (M80) (Rifle); Type IV: 30 Cal AP (M2 AP) (Rifle).

From table 2 it is possible to notice that a type IV projectile has more than 7.5 times the energy of an IIA type bullet.

During the design of ballistic protections it is very important to take into account that in addition to stopping the threat, the armor does not deform itself so that to create possible damage to the wearer or who repair behind it. Fig. 2.2 shows a clear example of how a vehicle ballistic protection can be transformed, itself, as a further threat to the personnel inside the vehicle once it suffers a blow. This example shows how it is necessary to have a combination of different materials depending on the type of situation. In this case a hard and rigid material serves to stop the threat and a flexible and toughness material serves to absorb energy by minimizing the explosive effects due to the impact on the rigid material.

Figure 2.2 Influence of the backing material [3]

In the last century, thanks to the discovery of new materials with low density and high resistance, it has been significantly possible to reduce the weight of the ballistic protection for personnel and vehicles.

Fig. 2.3 shows a schematic representation of the cross-section of an advanced ballistic protection. It is possible to note the different materials that are present: polymers, metals and ceramics. This structure, in addition to being designed to withstand threats, have to guarantee the structural integrity of the armor.

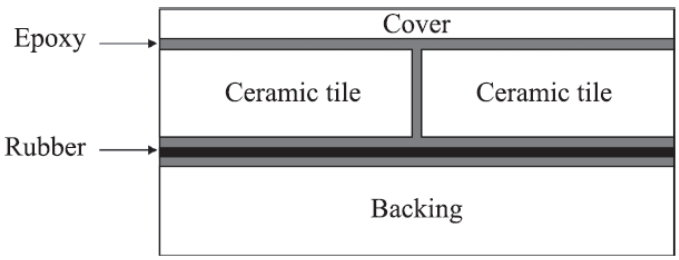

Figure 2.3 Schematic presentation of cross section of an armour tile typically used for armored vehicles showing the complexity of the armor architecture.

Advanced structural ceramics offer a unique combination of physical and mechanical properties which in turn can offer favorable protection against high-speed armor-piercing projectiles. The ceramics have high hardness, high Young's modulus, low density, good compression resistance but a relatively low fracture toughness. Properties such as hardness and elastic modulus are determined by chemical compositions and the microstructure of the material. In addition to the composition, many of ceramic material properties can be influenced by the relative amount of the different phases, mean grain size, and grain morphologies. One of the most important behavior of ceramic materials, that make them suitable for ballistic protection, is the strong covalent bond between light atoms. Light elements include beryllium, boron, carbon, oxygen, magnesium, aluminum and silicon.

Currently, the ceramic materials used for ballistic protection are Alumina (Al_2O_3), Silicon Carbide (SiC) and Boron Carbide (B_4C). The densities of B_4C (2.52 g/cm^3) and SiC (3.29 g/cm^3) are considerably lower than Al_2O_3 (3.98 g/cm^3). However, due to its easy sinterability and the lower cost of commercial powder, alumina is still preferred for use in vehicle applications, where the extra weight can be tolerated, while the lighter ceramics B_4C and SiC are now used in armor for individual use. Ceramic materials designed for individual protection are Silicon Nitride (Si_3N_4), Aluminum Nitride (AlN), Sialon, fiber-reinforced materials, CERMET (TiN, TiCN) and Titanium Diboride (TiB_2). These last materials are not widespread on the market for technical and economic reasons.

2.1.1 Boron Carbide / Titanium diboride (B_4C/TiB_2)

Boron carbide is one of the lightest and hardest ceramics with a unique combination of physical and mechanical properties that make it suitable for application in various industrial sectors, such as cutting tools, reinforcement materials, nuclear and thermoelectric applications [4–7]. The full potential use of B_4C is limited due to its poor sinterability (sintering temperature above 2200 °C) and the high susceptibility to brittle fracture (toughness 2-3 MPa·m$^{0.5}$) [8] .

The sintering of ceramic materials with covalent bonds is generally much more difficult than ceramic oxides. This is not only due to the low self-diffusion of atoms (low tendency to diffusion to grain boundaries) but also to their extreme sensitivity to environmental factors such as sintering atmosphere, traces of contaminants, size,

distribution and shape of particles etc.[9,10] . Sintering of pure boron carbide with high relative densities is always difficult.

Specific additives (sintering aids such as Carbon, Al_2O_3 or TiB_2) or sintering with the aid of pressure (HP), have been used to obtain an almost full dense material [1112]. B_4C powders are typically subjected to hot pressing at about 2100 °C and 30-40 MPa to obtain dense materials[13]. After hot pressing, Hot Isostatic Pressing (HIP) was applied to B_4C contaminated with carbon to reach 100 % of the theoretical density, which led to improvements in bending strength, Young's modulus and wear resistance of the final product[14]. The limitation of HP and HIP is that they are applicable only to rather simple shape.

The pressureless sintering (PLS) of B_4C, on the other hand, is often favored to avoid the expensive processing of diamond cutting tools required to obtain complex shapes.

The best known additive for pressureless sintering of B_4C is carbon. Dole et al.[15,16] observed B_4C sintered without carbon shown grain overgrowth (about 100 μm) after heat treatment at 2000 °C, while the carbon-doped samples maintained a finer microstructure. The authors suggested that the oxide layer (B_2O_3) present on the surface of the B_4C particles, would form a liquid phase leading to a rapid diffusion path along the surfaces of the particles, facilitating the grain growth due to evaporation - condensation phenomena. On the contrary, the addition of carbon acts by transforming the residual B_2O_3 on the surface of the boron carbide particles or volatile compounds during sintering step [15–17]. Several studies have shown that the addition of carbides or borides in B_4C [18–24] significantly improves densification, lowering the sintering temperature, and consequently improving properties such as oxidation and thermal shocks resistance. Furthermore the addition of other elements can hinder the grain growth and therefore improve the mechanical properties. The sintering additives used to manufacture the B_4C can be: Carbon; pure metals such as: Mg, Al, V, Cr, Fe, Co, Ni, Si, Ti; non oxide ceramics such as: BN, W_2B_5 ,SiC [25], TiC, TiB_2, CrB_2 etc; oxide ceramics: MgO, TiO_2, ZrO_2, Cr_2O_3, Y_2O_3, La_2O_3, Al_2O_3 [26], Fe_2O_3, AlF_3 [4].

Carbon is very effective as additive but residues on the grain boundary can significantly reduce the hardness. Likewise, residual metal phases at the grain boundaries, caused by metallic sintering additives, generally deteriorate the properties of hard ceramic materials. Although a detailed description of all possible additives for B_4C and their effect on final properties is outside the scope of this thesis, it is very important to emphasize that the addition of TiB_2 [27–36] is particularly studied for several reasons.

Titanium Diboride is a hard and stiff ceramic, particularly suitable for high temperature structural applications. It has a very high melting point (~3200 °C) and is an excellent electrical conductor with a resistivity of the order of 10-20 μΩ cm[37,38]. This feature can be used to work ceramic pieces by electro discharge machine (EDM), a less expensive technique than conventional diamond tool machining.

However, even in this case, B_4C-TiB_2 remain difficult to sinter, requiring temperatures above 2000 °C and/or the application of mechanical pressure.

For a good knowledge of the properties of TiB_2, Golla et al.[37], Munro[39] and Basu et al. [40] have collected a large number of informations about the synthesis, development and properties of TiB_2 such as: preparation with metallic and non-metallic sinter additives by different sintering technique, physical, tribological, mechanical and thermal properties.

The boron carbide can be obtained by different routes[8]:

- carbothermic reduction: this process consists in the carbothermic reduction of boric acid with graphite.

$$4H_3BO_3 + 7C \rightarrow B_4C + 6CO + 6H_2O \quad (1)$$

The reaction mechanism of (1) is the following:

$$4H_3BO_3 \rightarrow 2B_2O_3 + 6H_2O \quad (2)$$

$$B_2O_3 + 3CO \rightarrow 2B + 3CO_2 \quad (3)$$

$$4B + C \rightarrow B_4C \quad (4)$$

This process is strongly endothermic and required 16800 KJ mol^{-1} and temperature above 2000 °C

- magnesiothermic reduction: this is alternative method to obtain boron carbide and consists in the reduction of boron anhydride in presence of carbon

$$2B_2O_3 + 6Mg + C \rightarrow B_4C + 6MgO \quad (5)$$

The reaction mechanism of (5) is:

$$2B_2O_3 + 6Mg \rightarrow 4B + 6MgO \quad (6)$$

$$4B + C \rightarrow B_4C \quad (7)$$

The reaction is exothermic and the heat released is sufficient enough for self-high temperature synthesis rout. The products of the reaction are processed by aqueous methods to remove magnesium oxide from boron carbide. This reduction technique yields very fine amorphous powder, which is well suited for use in the fabrication of sintered products.

- synthesis from elements: for synthesis from elements, boron and carbon are thoroughly mixed to form uniform powder mixture and the reaction can carried out through arc-melting technique at 2500°C or self-propagating synthesis above 1100 °C by the reaction (6). To achieve a high purity product of B_4C, high purity elemental boron powder produced by fused salt electrolytic process is often used.

$$4B + C \rightarrow B_4C \quad (6)$$

- vapour phase reactions: in this synthesis is carried out the reaction between boron and carbon containing gaseous species. BCl_3 is suitable boron source due to its ready availability and low cost. Borane (B_6H_6) and oxide (B_2O_3) are also useful boron sources. Light hydrocarbons gas are employed as carbon source. Synthesis of boron carbide takes place in the reactor with the hydrogen in the atmosphere of reaction

$$4BCl_3 + CCl_4 + 8H_2 \rightarrow B_4C + 16HCl \quad (7)$$

Ridgeway[41] was the first to suggest the stoichiometric formula "B_4C" in 1934 but this formula is still under controversial discussion.

A lot of phase diagrams were proposed[31] and one of the most accepted is shown in Fig 2.4 The phase diagram showed that the boron carbide phase exist in the range from 9 to 21.6 at% of C. This phase melt congruently at 2450 °C at the composition $B_{13}C_2$

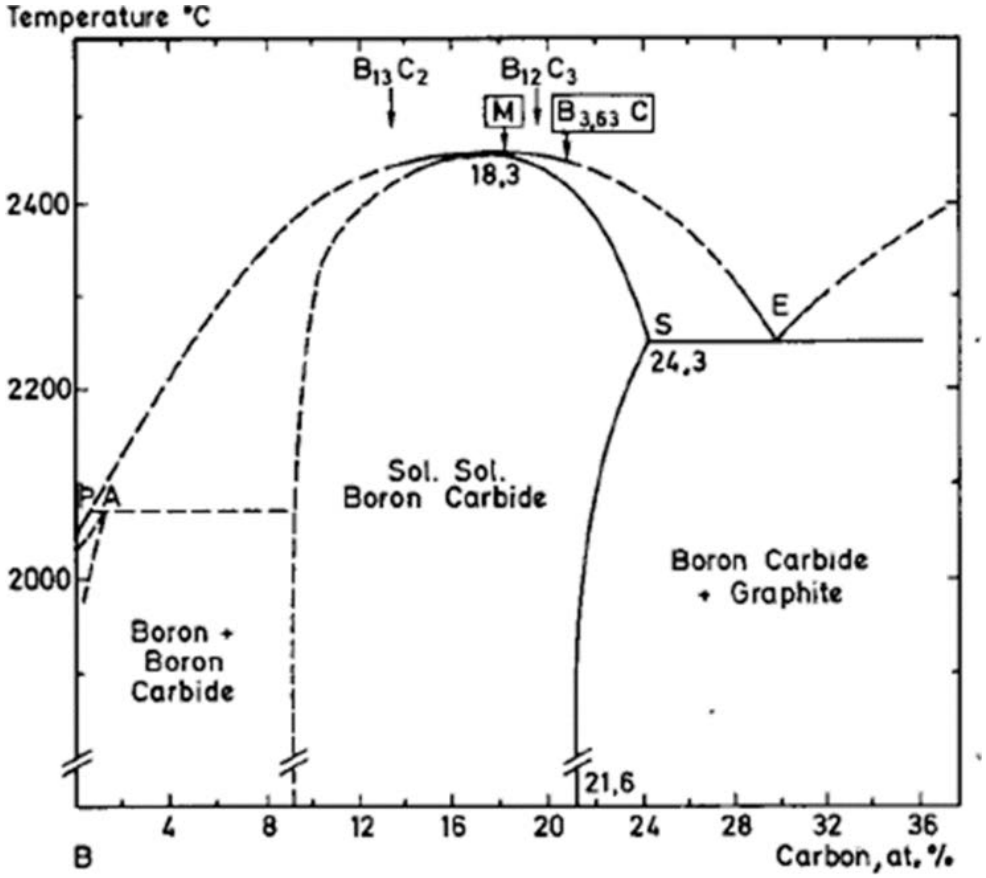

Figure 2.4 Phase diagram of boron-carbon system [42]

The crystal structure, showed in Fig. 2.5, consist in rhombohedral unit cell containing 12-B atom icosahedral cross-linked by 3 atom chains connected direct covalent bond in different method such as C-B-C or C-C-C. In this way the configuration can be $B_{12}C_3$ or $B_{11}C$. The lattice parameters are a_0= 5.60 Å and c_0= 12.09 Å with space group R3m.[43]

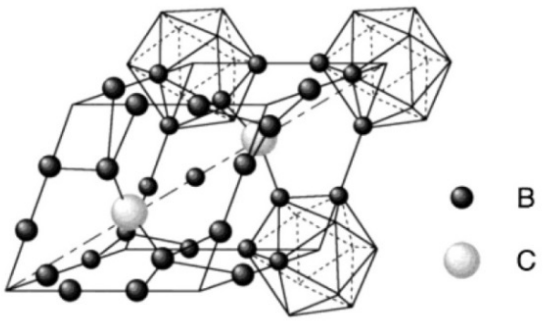

Figure 2.5 Crystal structure of boron carbide

The main physical properties are collected in the table 2.2

Table 2.2 Physical properties of boron carbide[43]

Property	Unit	
Density	g/cm^3	2.52
Crystal structure	Space group	R3m
Lattice constant a, c	nm	0.5607, 1.2095
Cell volume	nm^3	0.32894
Melting point	°C	2450
Thermal expansion coefficient α	10^{-6}/K	4.6 (25-800 °C)
Thermal conductivity λ	W/m·K	35(25 °C) 23(400 °C) 19(600 °C) 16(800 °C)
Thermal diffusivity α	$cm^2 s^{-1}$	1.0 X 10-1 (400 K) 3.0 X 10-2 (600 K) 2.1 X 10-2 (800 K)
Electric resistivity ρ	Ωcm	0.1-100
Self diffusion coefficient	cm^{-2}	5.18 X 10^{-10} (1000 °C)
Hardness HV1.0	GPa	35
Strength (4-pt. bending)	MPa	450-550
Fracture Toughness CNB	$MPa \cdot m^{0.5}$	2.5-3
Young's modulus E	GPa	400-450

2.2 High toughness structural ceramics

Developing both strong and tough materials is a challenge of the materials science since these properties are mutually exclusive, and are simultaneously required for almost all engineering structural materials [44]. Due to this mutual exclusion, stronger and harder materials cannot be used for safety-critical applications where catastrophic failure is unacceptable. At the state of art, the best compromises between the side properties were achieved with metallic glasses, natural and biological materials, and structural and biomimetic ceramics [44]. The above advanced materials have highly complex architectures (e.g. hierarchical architectures are shown by biological materials and biomimetic ceramics) where the mechanisms that enhance different properties simultaneously can originate from multiple length scales [45]. Each individual contribute results in composite properties that far exceed those of their constituents and their homogeneous mixtures [45,46]. For example, the micro-architectures of nacres − which can

be considered as staggered layers of brittle bricks held together by weak and stretchy mortar − play a key role in providing toughness by various damaging processes including crack deflection, crack bridging, and debonding ahead of the crack tip [47]. The strategies in dealing with strength versus toughness conflict lead to the bioinspired ceramics with 200 MPa of strength and 30 $MPa \cdot m^{0.5}$ fracture toughness, K_{IC} [48]. The strategies are more complex in the case of the developing of materials to be used in harsh environments due to the lower number of suitable materials and the impossibility to mimic the brick-and-mortar structure of nacre.

2.2.1 Materials for harsh environment (UHTCs, CMCs and UHTCMCs)

Ultra-high temperature ceramics (UHTCs) are a class of ceramic refractory materials interesting for their high melting point (> 3200 °C), chemical stability and resistance to erosion and ablation. For this reason, carbides and borides, such as ZrB_2, TiB_2, HfB_2, ZrC, HfC, TaC, are potential candidates components that work in extreme environment condition; thermal protection systems, leading edges in hypersonic flights and nozzles for rockets [49–51]. Among the others, ZrB_2 has the low density, high strength-to-weight ratio and good oxidation resistance if combined with carbides such as B_4C, SiC or metal silicides such as $MoSi_2$ [51,52]. On the other hand, like the others UHTCs, it is susceptible to brittle fracture (K_{IC} < 5 $MPa \cdot m^{0.5}$) and displays low thermal shock resistance. It is well known that monolithic ceramics are not toughened by promoting plasticity, but they can be toughened up to 10 $MPa \cdot m^{0.5}$ by the frictional interlocking of grains (grain bridging) during intergranular fracture [53]. Since UHTCs cannot exploit in situ phase transformations, glassy films, and have not any ferroic order to allow the domains switch at the coercive stress at crack tip, the main strategy to (i) enhance the intergranular fracture [54] rather than the transgranular crack propagation, and (ii) increase the tortuous crack path was the development of large elongated or plate-like grains [55]. In the last years, renewed research efforts improved the damage-tolerance of ZrB_2 by moving from ceramics to Ceramic Matrix Composites (CMCs). The first CMCs enabled a toughness increase by adding short SiC fibers [56,57], and started a novel class of materials called Ultra- High Temperature Ceramic Matrix Composites (UHTCMCs) [58]. UHTCMCs based on carbon fibers dispersed into ZrB_2 matrix, can increase the failure tolerant behavior through damage processes ahead of the crack tip, such as crack deflection mechanisms, and behind of the crack tip, such as fiber bridging and fiber

pull-out. These mechanisms consume energy during the fracture process, provided that the fiber/ matrix interface is well designed and the chemical reactions at the fiber/matrix interface do not degrade the reinforcement properties [44,57,59,60]. By optimizing the production process to achieve an homogeneous dispersion of the UHTC matrix into the fiber preform, a good densification level and a good fiber/matrix adhesion avoiding fiber degradation, the toughness was increased up to 10 $MPa \cdot m^{0.5}$ while keeping a flexural strength of 85–95 MPa [58,61]. The high amount, 65–70%, of well dispersed fibers, the low crack resistance of the fiber/matrix interfaces, and the weak matrix allowed the easy fiber pull-out, delamination, fiber bridging, and hence led to a non-brittle fracture [61]. In these weak matrix composites (WMCs) the matrix is subjected to multiple cracking whilst the fibers provide strength and crack tolerance, in this way after the matrix is completely fractured by multiple microcracking, the total fracture occurs with the failure of the fibers [61]. A further development for UHTCMCs in terms of toughness can be borrowed from strategy behind the solution-polymerized acrylonitrile- butadiene-styrene (ABS): the salami-like particles [62,63]. The dispersed salami-like particles consist in polybutadiene particles (PB) grafted (-g-) by acrylonitrile-styrene copolymer (SAN). The PB rubber particles, in the PB-g-SAN binary phase system, are characterized by a strong residual stress that facilitates the crazing and shearing, reducing the stresses on the crack wake. Thus, the concept of the salami-like particles is that of increasing the extrinsic crack-tip-shielding mechanisms that act behind the crack tip to inhibit its propagation. In the UHTCMCs, the corresponding microstructural features playing a similar role can be the load-bearing fibers, having a non-uniform distribution, and being concentrated in bundles where the fiber density increases at the outer periphery. Such graded structure, similar to the fiber distribution in a bamboo structure, should also enhance the specific flexural rigidity [45]. Hence, the aimed scenario is the promoting of extensive microcracking ahead of the crack tip, primarily between the bundles (in other words, along the weak matrix), which leaves uncracked- bundle bridges (the cross section should be appear like a slice of salami). The uncracked-bundle bridges (as the crazing and shearing phenomena activated by the salami-like particles [62,63]) will act as intact regions spanning the crack wake to inhibit its progress by further microcracking inside the bundles and crack deflection along the transverse orientation to the main fracture surface. At the end of the fracture processes, the salami-inspired UHTCMCs should fail under bundle pull-out mode.

2.3 High entropy materials

In recent years, high entropy alloys (HEA) have attracted growing interest [64–66]. Starting from work on metals, these new alloys are composed of "r"-number of metal specimens, generally $r \geq 5$, to form a high entropy solution having increased entropy of mixing $\Delta S_{mix} = -nR \sum_{i=1}^{r} x_i \ln x_i$,where n is the total number of moles, R is the gas constant, x_i is the mole fraction of component i [65]. The theory supporting these new alloys relies upon the principle of Gibbs free energy minimization, $\Delta G = \Delta H - T \cdot \Delta S$. According to this principle, a system with an enhanced entropy (ΔS) is more stable (ΔG<0) at high temperatures thanks to the contribution of the entropic term (-T·ΔS). HEAs have been shown to have improved properties compared to conventional alloys. Further necessary conditions for the existence of the substitutional solid solutions are set by the Hume-Rothery solid solution rules. Indeed, in order to obtain substitute alloys, two or more metals must meet the following requirements: 1) atomic radii that do not differ by more than 15 %, 2) same crystal structure, 3) similar electronegativity, 4) same valence.

2.3.1 High entropy metal diborides (HEMB)

High entropy oxides [67–70], borides [71–75] , carbides [76–79] and silicides [80] have been obtained using different synthesis/sintering techniques such as spark plasma sintering and pressureless sintering. For instance, Gild et al. [69] have successfully synthesized high-entropy fluorite oxides (HEFO), with hardness comparable to 8 mol. Y_2O_3-stabilized ZrO_2 and low electrical and thermal conductivities. Castel et al. [77] have shown a significant enhancement in hardness of high entropy carbides material compared to the value calculated according to the rule of mixtures from the reference monocarbides and in comparison to the hardest monocarbide. Tallarita et al. [73] have produced high entropy borides starting from the respective oxides and boron, through a two-step processing method of Self-propagating High-temperature Synthesis (SHS) followed by SPS. This approach avoided the need for intense mechanical milling of individual borides. Although reactive sintering by SPS may be faster than hot pressing and pressureless sintering, it still requires costly equipment, high temperatures (>2000 °C) and high pressures (tens of MPa) to promote atomic diffusion of different elements to obtain solid solutions. Alternatively, Zhang et al. [81] have obtained solid solutions of binary and ternary carbides in a very short time (10-20 seconds) using the arc melting

technique. This technique, already known in the metallurgical field, is able to reach very high temperatures, and therefore, melting materials with high melting point, close to 4000 °C, in a short time (a few seconds). In this way it was possible demonstrate the formation of solid solutions of binary, ternary carbides.

2.4 References

1. Thomas, E. L. *Opportunities in Protection Materials Science and Technology for Future Army Applications*. (2012). doi:10.1002/9781118217498.ch13
2. NIJ. *NIJ Standard-0101.06, Ballistic Resistance of Personal Body Armor*. (2008).
3. Ash, R. A. Vehicle armor. in *Lightweight Ballistic Composites: Military and Law-Enforcement Applications: Second Edition* 285–309 (Elsevier Ltd, 2016). doi:10.1016/B978-0-08-100406-7.00009-X
4. Thevenot, F. A Review on Boron Carbide. *Key Eng. Mater.* **56**–**57**, 59–88 (1991).
5. Larsson, P., Axén, N. & Hogmark, S. Improvements of the microstructure and erosion resistance of boron carbide with additives. *J. Mater. Sci.* **35**, 3433–3440 (2000).
6. Zorzi, J. E., Perottoni, C. A. & Da Jornada, J. A. H. Hardness and wear resistance of B4C ceramics prepared with several additives. *Mater. Lett.* **59**, 2932–2935 (2005).
7. Hayun, S. Reaction-bonded boron carbide for lightweight armor: The interrelationship between processing, microstructure, and mechanical properties. *Am. Ceram. Soc. Bullettin* **96**, 20–26 (2017).
8. Suri, A. K., Subramanian, C., Sonber, J. K. & Murthy, T. S. R. C. *Synthesis and consolidation of boron carbide: a review*. *International Materials Reviews* **55**, (2010).
9. Greskovich, C. & Rosolowski, H. J. Sintering of Covalent Solids. *J. Am. Ceram. Soc.* **59**, 336–343 (1976).
10. DeHoff, R. T., Rummel, R. A., LaBuff, H. P. & Rhines, F. N. The Relationship Between Surface Area and Density in the Second-Stage Sintering of Metals. in *Modern Development in Powder Metallurgy* (ed. Hausner, H. H.) 310–330 (1966). doi:10.1007/978-1-4684-7706-1
11. Thévenot, F. Boron carbide- A comprehensive review. *J. Eur. Ceram. Soc.* **6**, 205–225 (1990).
12. Tuff, S., Dubois, J., Fantozzi, G. & Barbier, G. Densification , Microstructure and Mechanical Properties of TiB_2-B_4C Based Composites. *Int. J. Refract. Met. Hard Mater.* **14**, 305–310 (1996).
13. Angers, R. & Beauvy, M. Hot-pressing of boron carbide. *Ceram. Int.* **10**, 49–55 (1984).
14. Schwets, K. A., Grellner, W. & Lipp, A. *Mechanical Properties of HIP-Treated Sintered Boron Carbide*. *Inst. Phys. Conf. Ser. No.* **75**, (1986).
15. Dole, S. L. & Prochazka, S. Densification and Microstructure Development in Boron Carbide. *Proc. 9th Annu. Conf. Compos. Adv. Ceram. Mater. Ceram. Eng. Sci. Proc.* 1151–1160 (2008). doi:10.1002/9780470320280.ch65
16. Dole, S. L., Prochazka, S. & Doremus, R. H. Microstructural Coarsening During Sintering of Boron Carbide. *J. Am. Ceram. Soc.* **72**, 956–966 (1989).
17. Prochazka, S., Dole, S. L. & Hejna, C. I. Abnormal Grain Growth and

Microcracking in Boron Carbide. *J. Am. Ceram. Soc.* **68**, C-235-C–236 (1985).
18. Zhang, Z. *et al.* Microstructures and mechanical properties of B_4C-SiC intergranular/intragranular nanocomposite ceramics fabricated from B_4C, Si, and graphite powders. *J. Eur. Ceram. Soc.* **34**, 2153–2161 (2014).
19. Jianxin, D. & Junlong, S. Microstructure and mechanical properties of hot-pressed B_4C/TiC/Mo ceramic composites. *Ceram. Int.* **35**, 771–778 (2009).
20. Sairam, K. *et al.* Development of B_4C–HfB_2 composites by reaction hot pressing. *Int. J. Refract. Met. Hard Mater.* **35**, 32–40 (2012).
21. Yamada, S., Hirao, K., Yamauchi, Y. & Kanzaki, S. B_4C-CrB_2 composites with improved mechanical properties. *J. Eur. Ceram. Soc.* **23**, 561–565 (2003).
22. Zhang, X. *et al.* Densification behaviour and mechanical properties of B_4C–SiC intergranular/intragranular nanocomposites fabricated through spark plasma sintering assisted by mechanochemistry. *Ceram. Int.* **43**, 1904–1910 (2017).
23. Wen, Q., Tan, Y., Zhong, Z., Zhang, H. & Zhou, X. High toughness and electrical discharge machinable B_4C-TiB_2-SiC composites fabricated at low sintering temperature. *Mater. Sci. Eng. A* **701**, 338–343 (2017).
24. Huang, S. G., Vanmeensel, K. & Vleugels, J. Powder synthesis and densification of ultrafine B_4C-ZrB_2 composite by pulsed electrical current sintering. *J. Eur. Ceram. Soc.* **34**, 1923–1933 (2014).
25. Uehara, M., Shiraishi, R., Nogami, A., Enomoto, N. & Hojo, J. SiC–B_4C composites for synergistic enhancement of thermoelectric property. *J. Eur. Ceram. Soc.* **24**, 409–412 (2004).
26. Kim, H.-W., Koh, Y.-H. & Kim, H.-E. Densification and Mechanical Properties of B_4C with Al_2O_3 as a Sintering Aid. *J. Am. Ceram. Soc.* **83**, 2863–2865 (2000).
27. He, P., Dong, S., Kan, Y., Zhang, X. & Ding, Y. Microstructure and mechanical properties of B_4C-TiB_2 composites prepared by reaction hot pressing using Ti_3SiC_2 as additive. *Ceram. Int.* **42**, 650–656 (2016).
28. Bogomol, I., Nishimura, T., Vasylkiv, O., Sakka, Y. & Loboda, P. Microstructure and high-temperature strength of B_4C-TiB_2 composite prepared by a crucibleless zone melting method. *J. Alloys Compd.* **485**, 677–681 (2009).
29. Qing-Qing, L., Shao-Ming, D., Ping, H., Hai-Jun, Z. & Jian-Bao, H. Microstructure and Property of TiB_2 Reinforced Reaction-bonded B_4C Composites. *J. Inorg. Mater.* **30**, 667 (2015).
30. Li, A., Zhen, Y., Yin, Q., Ma, L. & Yin, Y. Microstructure and properties of (SiC, TiB_2)/B_4C composites by reaction hot pressing. *Ceram. Int.* **32**, 849–856 (2006).
31. Rogl, P. F., Vřešťál, J., Tanaka, T. & Takenouchi, S. The B-rich side of the B-C phase diagram. *Calphad Comput. Coupling Phase Diagrams Thermochem.* **44**, 3–9 (2014).
32. Skorokhod, V. V & Krstic, V. D. Processing, Microstructure, and Mechanical Properties of B_4C-TiB_2 Particulate Sintered Composites I. Pressureless Sintering and Microstructure Evolution. *Powder Metall. Met. Ceram.* **39**, 414–423 (2000).
33. Skorokhod, V. & Krstic, V. D. Processing, Microstructure, and Mechanical Properties of B_4C-TiB_2 Particulate Sintered Composites. II. Fracture and mechanical properties. *Powder m* **39**, 504–513 (2000).
34. Yamada, S., Hirao, K., Yamauchi, Y. & Kanzaki, S. High strength B4C-TiB2 composites fabricated by reaction hot pressing. *J. Eur. Ceram. Soc.* **23**, 1123–1130 (2003).
35. Gao, Y. *et al.* Study of static and dynamic behavior of TiB_2-B_4C composite. *Mater. Des.* **92**, 814–822 (2016).

36. Huang, S. G., Vanmeensel, K., Malek, O. J. A., Biest, O. Van Der & Vleugels, J. Microstructure and mechanical properties of pulsed electric current sintered B_4C-TiB_2 composites. *Mater. Sci. Eng. A* **528**, 1302–1309 (2011).
37. Golla, B. R., Bhandari, T., Mukhopadhyay, A. & Basu, B. Titanium Diboride. in *Ultra-High Temperature Ceramics: Materials for ExtremeEnvironment Applications* (eds. Fahrenholtz, W. G., Wuchina, E. J., Lee, W. E. & Zhou, Y.) 316–360 (2014). doi:10.1002/9781118700853.ch13
38. McLeod, A. D., Haggerty, J. S. & Sadoway, D. R. Electrical Resistivities of Monocrystalline and Polycrystalline TiB2. *J. Am. Ceram. Soc.* **67**, 705–708 (1984).
39. Munro, R. G. Material Properties of Titanium Diboride. *J. Res. Natl. Inst. Stand. Technol.* **105**, 709 (2000).
40. Basu, B., Raju, G. B. & Suri, A. K. Processing and properties of monolithic TiB_2 based materials. *Int. Mater. Rev.* **51**, 352–374 (2006).
41. Ridgway, R. R. BORON CARBIDE. A New Crystalline Abrasive and Wear-Resisting Product. *J. Electrochem. Soc.* **66**, 117–133 (1934).
42. Beauvy, M. Stoichiometric limits of carbon-rich boron carbide phases. *J. Less-Common Met.* **90**, 169–175 (1983).
43. Telle, R., Sigl, L. S. & Takagi, K. Boride-Based Hard Materials. *Handb. Ceram. Hard Mater.* 802–945 (2008). doi:10.1002/9783527618217.ch22
44. Ritchie, R. O. The conflicts between strength and toughness. *Nat. Mater.* **10**, 817–822 (2011).
45. Wegst, U. G. K., Bai, H., Saiz, E., Tomsia, A. P. & Ritchie, R. O. Bioinspired structural materials. *Nat. Mater.* **14**, 23–36 (2015).
46. Daniel, R. *et al.* Grain boundary design of thin films: Using tilted brittle interfaces for multiple crack deflection toughening. *Acta Mater.* **122**, 130–137 (2017).
47. Niebel, T. P., Bouville, F., Kokkinis, D. & Studart, A. R. Role of the polymer phase in the mechanics of nacre-like composites. *J. Mech. Phys. Solids* **96**, 133–146 (2016).
48. Munch, E. *et al.* Tough, Bio-Inspired Hybrid Materials. *Science (80-.).* **322**, 1516–1521 (2008).
49. Fahrenholtz, W. G., Hilmas, G. E., Talmy, I. G. & Zaykoski, J. A. Refractory diborides of zirconium and hafnium. *J. Am. Ceram. Soc.* **90**, 1347–1364 (2007).
50. Guo, S.-Q. Densification of ZrB_2-based composites and their mechanical and physical properties: A review. *J. Eur. Ceram. Soc.* **29**, 995–1011 (2009).
51. Sciti, D., Silvestroni, L., Medri, V. & Monteverde, F. Sintering and densification mechanisms of ultra-high temperature ceramics. in *Ultra-High Temperature Ceramics: Materials for ExtremeEnvironment Applications* (eds. Fahrenholtz, W. G., Wuchina, E. J., Lee, W. E. & Zhou, Y.) 112–143 (2014). doi:10.1002/9781118700853.ch6
52. Silvestroni, L., Meriggi, G. & Sciti, D. Oxidation behavior of ZrB_2 composites doped with various transition metal silicides. *Corros. Sci.* **83**, 281–291 (2014).
53. Gilbert, C. J., Cao, J. J., Jonghe, L. C. & Ritchie, R. O. Crack-Growth Resistance-Curve Behavior in Silicon Carbide: Small versus Long Cracks. *J. Am. Ceram. Soc.* **80**, 2253–2261 (2010).
54. Sveleba, S., Zhmurko, V., Kapustianik, V., Polovinko, I. & Trybula, Z. Influence of Electric Field and Mechanical Stresses on the Properties of Incommensurate in $(N(CH_3)_4)_2ZnCl_4$ and $(N(CH_3)_4)_2CoCl_4$ Crystals. *Annu. Rev. Mater. Res.* **140**, 573–585 (1993).

55. Sciti, D., Guicciardi, S. & Bellosi, A. Effect of annealing treatments on microstructure and mechanical properties of liquid-phase-sintered silicon carbide. *J. Eur. Ceram. Soc.* **21**, 621–632 (2001).
56. Sciti, D. *et al.* From random chopped to oriented continuous SiC fibers-ZrB_2 composites. *Mater. Des.* **63**, 464–470 (2014).
57. Silvestroni, L., Dalle Fabbriche, D., Melandri, C. & Sciti, D. Relationships between carbon fiber type and interfacial domain in ZrB_2-based ceramics. *J. Eur. Ceram. Soc.* **36**, 17–24 (2016).
58. Zoli, L. & Sciti, D. Efficacy of a ZrB_2–SiC matrix in protecting C fibres from oxidation in novel UHTCMC materials. *Mater. Des.* **113**, 207–213 (2017).
59. Yang, F., Zhang, X., Han, J. & Du, S. Processing and mechanical properties of short carbon fibers toughened zirconium diboride-based ceramics. *Mater. Des.* **29**, 1817–1820 (2008).
60. Sha, J. J. *et al.* Toughening effect of short carbon fibers in the ZrB_2-$ZrSi_2$ ceramic composites. *Mater. Des.* **75**, 160–165 (2015).
61. Sciti, D., Natali Murri, A., Medri, V. & Zoli, L. Continuous C fibre composites with a porous ZrB_2 Matrix. *Mater. Des.* **85**, 127–134 (2015).
62. Heckmann, W., McKee, G. E. & Ramsteiner, F. Structure-property relationships in rubber-modified styrenic polymers. *Macromol. Symp.* **214**, 85–96 (2004).
63. Mazidi, M. M., Razavi Aghjeh, M. K. & Abbasi, F. Fractographic analysis of the crack resistance of styrene-acrylonitrile/ polybutadiene-g-styrene-acrylonitrile blends as evaluated by the essential work of fracture method. *J. Appl. Polym. Sci.* **131**, 1–10 (2014).
64. Yeh, J. W. *et al.* Nanostructured high-entropy alloys with multiple principal elements: Novel alloy design concepts and outcomes. *Adv. Eng. Mater.* **6**, 299-303+274 (2004).
65. Zhang, Y. *et al.* Microstructures and properties of high-entropy alloys. *Prog. Mater. Sci.* **61**, 1–93 (2014).
66. Tsai, M. H. & Yeh, J. W. High-entropy alloys: A critical review. *Mater. Res. Lett.* **2**, 107–123 (2014).
67. Rost, C. M. *et al.* Entropy-stabilized oxides. *Nat. Commun.* **6**, 1–8 (2015).
68. Jiang, S. *et al.* A new class of high-entropy perovskite oxides. *Scr. Mater.* **142**, 116–120 (2018).
69. Gild, J. *et al.* High-entropy fluorite oxides. *J. Eur. Ceram. Soc.* **38**, 3578–3584 (2018).
70. Biesuz, M. *et al.* High entropy $Sr((Zr_{0.94}, Y_{0.06})_{0.2}Sn_{0.2}Ti_{0.2}Hf_{0.2}Mn_{0.2})O_{3-x}$ perovskite synthesis by reactive spark plasma sintering. *J. Asian Ceram. Soc.* **0**, 1–6 (2019).
71. Gild, J. *et al.* High-Entropy Metal Diborides: A New Class of High-Entropy Materials and a New Type of Ultrahigh Temperature Ceramics. *Sci. Rep.* **6**, 2–11 (2016).
72. Mayrhofer, P. H., Kirnbauer, A., Ertelthaler, P. & Koller, C. M. High-entropy ceramic thin films; A case study on transition metal diborides. *Scr. Mater.* **149**, 93–97 (2018).
73. Tallarita, G., Licheri, R., Garroni, S., Orrù, R. & Cao, G. Novel processing route for the fabrication of bulk high-entropy metal diborides. *Scr. Mater.* **158**, 100–104 (2019).
74. Zhang, Y. *et al.* Microstructure and mechanical properties of high-entropy borides derived from boro/carbothermal reduction. *J. Eur. Ceram. Soc.* 0–1 (2019). doi:10.1016/j.jeurceramsoc.2019.05.017

75. Feng, L., Fahrenholtz, W. G. & Hilmas, G. E. Two-step synthesis process for high-entropy diboride powders. *J. Am. Ceram. Soc.* 1–7 (2019). doi:10.1111/jace.16801
76. Dusza, J. *et al.* Microstructure of (Hf-Ta-Zr-Nb)C high-entropy carbide at micro and nano/atomic level. *J. Eur. Ceram. Soc.* **38**, 4303–4307 (2018).
77. Castle, E., Csanádi, T., Grasso, S., Dusza, J. & Reece, M. Processing and Properties of High-Entropy Ultra-High Temperature Carbides. *Sci. Rep.* **8**, 1–12 (2018).
78. Yan, X. *et al.* ($Hf_{0.2}$ $Zr_{0.2}$ $Ta_{0.2}$ $Nb_{0.2}$ $Ti_{0.2}$)C high-entropy ceramics with low thermal conductivity. *J. Am. Ceram. Soc.* **101**, 4486–4491 (2018).
79. Sarker, P. *et al.* High-entropy high-hardness metal carbides discovered by entropy descriptors. *Nat. Commun.* **9**, 1–10 (2018).
80. Gild, J. *et al.* A high-entropy silicide: ($Mo_{0.2}Nb_{0.2}Ta_{0.2}Ti_{0.2}W_{0.2}$)$Si_2$. *J. Mater.* **5**, 337–343 (2019).
81. Zhang, Z. *et al.* Arc melting: a novel method to prepare homogeneous solid solutions of transition metal carbides (Zr, Ta, Hf). *Ceram. Int.* **45**, 9316–9319 (2019).

3. Experimental

3.1 Production of advanced ceramics

ISTEC-CNR possesses instruments and wide know-how for the design, process, sintering materials and mechanical characterization of non-oxide structural ceramics.
In this chapter the techniques for the production of advanced ceramics and mechanical tests discussed in this thesis will be illustrated on the basis of previous work[1] where the main experimental activities conducted at ISTEC are explained in more detail.
"In this work, the processing of ceramics is developed in several stages:

- choice of raw materials
- powder treatment
- molding
- sintering process
- finishing

Each of these phases is critical, as can be source of flaws or imperfections in the materials which sum each others up and hinder the achievement of the desired properties"[1].

3.2 Process

3.2.1 Raw material and preparation of mixtures

The starting powders were treated through a suitable mixing process which allows a good homogenization of the different phases: matrix and sintering additives.
The dispersion and mixing of the powders was carried out according to two different procedures: soft ball milling (SB) and high energy milling (HEBM) (Pulverisette 6 Classi Line, Fritsch Planetary Mill).
Commercially available powders were used:

- ZrB_2 (H.C. Starck, grade B, Germany, specific surface area 1.0 m^2/g, particle size range 0.5-6 μm, impurities (wt.%): 0.25 C, 2 O, 0.25 N, 0.1 Fe, 0.2 Hf),
- TiB_2 (H.C. Starck, Grade F, D_{90} 4.0 -7.0 μm, D_{50} 2.5-3.5 μm, impurities (wt. %): 0.4 C, 2.5 O, 0.5 N, 0.1 Fe)

- HfB_2 (Treibacher, D_{50} 2.56 μm, impurities (wt.%): 0.23 C, 0.01 N, 0.23 O, <0.001 S)
- TaB_2 (Materion, purity 99.5%, impurities (wt.%): 0.04 Al, < 0.0007 Cd, < 0.0005 Cr, 0.07 Fe, 0.02 Nb, <0.0004 Pb)
- CrB_2 (H.C. Starck, Grade B, D_{90} 4.0 -6.0 μm, D_{50} 1.5-3 μm, impurities (wt. %): 0.3 C, 0.6 O, 0.5 Fe)
- B_4C (H.C. Starck Grade HS-A, D_{90} 2.0–4.0 μm, D_{50} 0.6–1.2 μm, B:C ratio 3.7, impurities (wt. %): 0.7 N, 1.7 O, 0.05 Fe, 0.15 Si, 0.05 Al)
- WC (Treibacher, Grade 05, purity 99.5%, D_{50} 0.5 μm)

Particles size of commercial TiB_2 and mixture of commercial B_4C and TiB_2 before and after milling was measured by sedimentation analysis (Sedigraph 5100, Micrometrics, Atlanta, USA).

3.2.2 Molding

"During the molding stage the powders were consolidated through different techniques in a green compact. This hand-manufactured piece is characterized by a high degree of porosity that depends on the kind of the utilized powder, on the underwent treatment and on the particular molding technique, it generally goes from 50 to 70% of the theoretical density"[1]. The main techniques used for this work are explained in the following.

- Pressing

- "Uniaxial pressing: the compacting occurs in a stiff steel die through the application of a unidirectional pressure"[1].
- "Cold isostatic pressing (CIP): the pre-compacted powder is placed in a rubber die, immersed in a fluid (glycerine, hydraulic oil, water,…) inside a pressure chamber. The fluid transfers the pressure (more than 400 MPa can be achieved) to every part of the die in a uniform way. Hence, by cold isostatic pressing more complex shapes can be obtained than by uniaxial pressing"[1].

- Electrophoresis deposition

Electrophoresis deposition (EPD, electrophoretic deposition) is a technique that allows the realization of coatings, laminated structures or functional gradient materials starting

from a stable suspension of powder in an aqueous or organic medium[2]. The method involves the use of two electrodes, one of which having the shape of the piece to be obtained, dip in the suspension of the solid to be deposited[3]. Between them an electric potential difference (V) is applied: the particles, which in contact with the dispersion medium assume a positive or negative surface charge, move towards the opposite electrode and settle there (Fig. 3.1)[4,5].

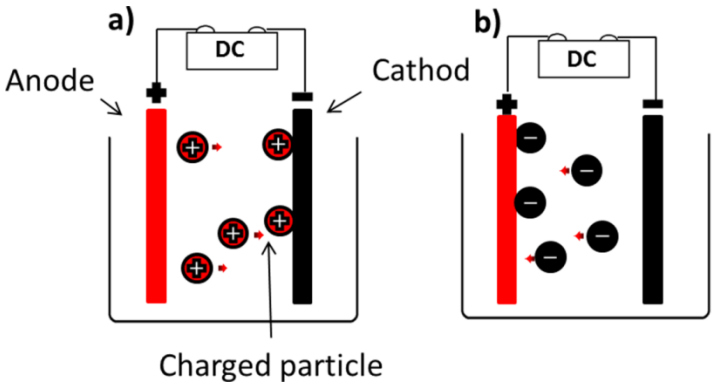

Figure 3.1 Schematic illustration of electrophoretic deposition process. (a) Cathodic EPD and (b) anodic EPD

The electrode on which the deposition takes place can act as a simple support or be an integral part of the final product (reinforcement fabric or fibers, a surface that must be coated, decorated or protected). In the first case the material must be electrically conductive and has the shape of the requested piece. At the end of the deposition the product must be removed with caution, to avoid cracking or leaching of the deposit [6]. If the electrode is to be part of the product, it must be made of the required material, preferably conductor. So far many studies have been carried out on EPD coating of fiber in order to produce metal matrix composites (MMCs) [7], CMCs [8], or just to use the fiber as a template for replicas of different kinds of ceramics [9]. In case of high toughness structural CMCs, the coating mainly aims to (i) control interface debonding and frictional sliding in order to increase the crack-wake bridging phenomena and subsequent toughness [8,10,11], and (ii) protect from degradation at high temperature [12]. This behaviors allows to achieve the best compromise between the matrix-to-fiber stress transfer, and crack deflection and pull-out [13]. Dispersion and co-dispersion of ZrB_2 and/or SiC have been reported in the literature [14–17], as well as EPD of ZrB_2-SiC films starting from aqueous suspensions [16,18]. The main problem of water based suspension is the electrolysis of water which can result in large and irregularly distributed flaws [16,18].

Furthermore electrochemical reactions can occur on the surface of the metal electrode when current are passing off. For these reasons, many researchers prefer the use of organic solvent, even if they are not eco-friendly [19–22].
In this work, carbon fiber (C_f) was used as substrate in EPD process:

- Carbon fibers (Granoc XN80-6K: density 2.17 g/cm^3, fabric thickness 330 mm, mass per unit area 330 g/m^2, fiber diameter 10 mm, sized with epoxy resin about 1 wt%, CTE -1.5 10^{-6}/K, tensile modulus of 780 GPa and tensile strength 3.4 GPa)

3.2.3 Sintering process

Sintering is a fundamental technological step to manufacture almost all ceramics from compacted powder particles. During the sintering process the powder compacts densify with accompanying dimensional changes resulting in mechanical strengthening, possible gastight microstructures and improved thermal conductivity. The density of green samples was measured by geometric method. For the sintered materials, the density was measured by Archimede's principle and image analysis of the SEM picture (see section 3.3.2).
The standard measurement of Archimede's method consists in recording the mass of dry sample, dip and weight the same sample in a liquid and then apply the following equation:

$$\rho_{Archimede} = \frac{m_{dry}}{m_{dry} - m_{sub}} \rho_{liquid}$$

where m_{dry} is the weight of dry sample, m_{sub} is the weight of the dip sample in a liquid and ρ_{liquid} is the density of the liquid.
The relative density (RD) of each samples was calculated from the ratio of experimental density (ρ_{exp}) and theoretical density (ρ_{th}):

$$RD = \frac{\rho_{exp}}{\rho_{th}} \cdot 100$$

All the theoretical densities of the studied compounds are listed in the section 3.3.3

- **Hot pressing (HP)**

High density materials with a very fine microstructure, and therefore with high mechanical resistance, are obtained by hot pressing (HP). Sintering by hot pressing is carried out in low vacuum (about 10 Pa), in a graphite oven heated by induction heating, with a heating rate of 80 °C/min and free cooling, and with a constant uniaxial load applied of 30-40 MPa. For each composition, the maximum sintering temperature is established by analyzing the shrinkage curve of the rams during densification.

From this analysis (see chapter 4) we can observe at which temperature shrinkage start, the shrinkage (densification) rate, and the maximum temperature needed for complete densification.

Fig. 3.2 shows images of the vacuum furnace for HP with induction heating system (Ing.Allaria MP20 / II Alto Vuoto, IT).

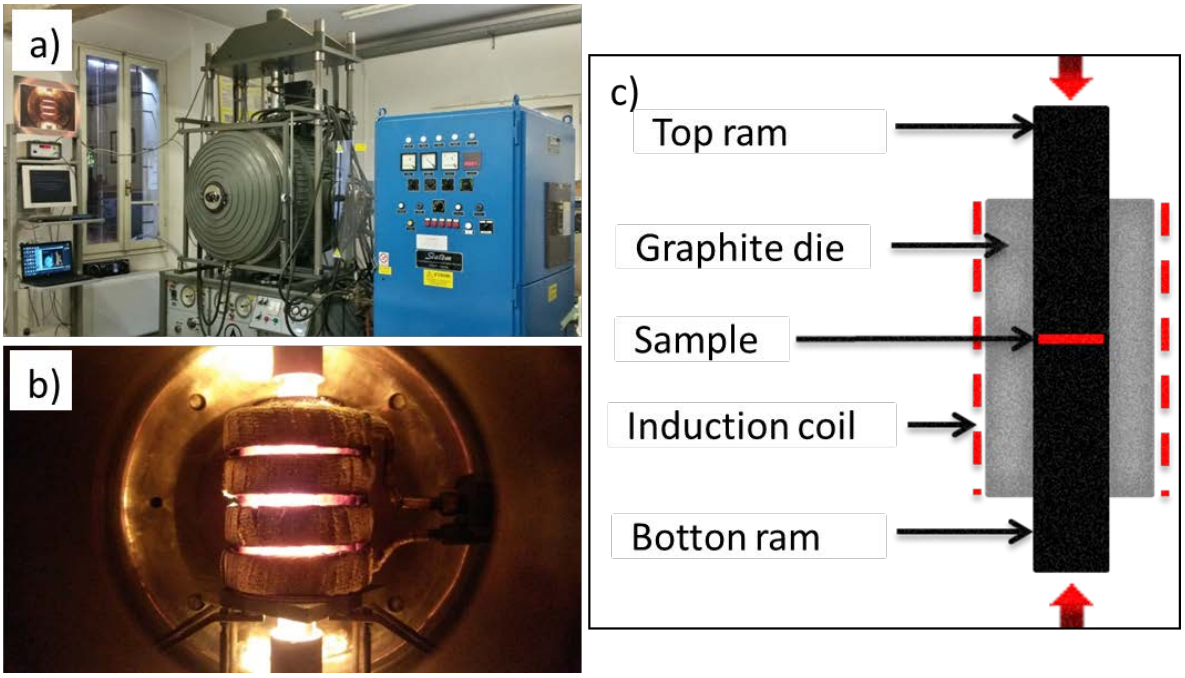

Figure 3.2 a) Vacuum hot pressing (HP) with induction heating system (Ing. Allaria MP20 / II Alto Vuoto, IT); b) induction coil (internal chamber of the oven, working condition 1900 °C); c) simplifying scheme of the hot pressing process

- **Pressureless sintering / Gas pressure sintering (PLS/GPS)**

Ceramic B_4C/TiB_2 based materials (see Chapter 4) were sintered at temperatures up to 2100 °C in vacuum or in an inert atmosphere at atmospheric pressure or in gas pressure up to 50 bar. The gas pressure depends on the final temperature. Maximum pressures

achievable in our furnace at ISTEC are 20 bar at 2400 °C and 100 bar for temperatures up to 1800 °C. Complex shaped samples can be produced. The oven chamber is large enough to accommodate green discs with a starting diameter up to about 180 mm.

The height of the chamber is about 280 mm so it is possible to sinter more discs at the same time. Fig. 3.3 shows images of the LHTG 200-300 / 24-1G Carbolite Gero oven.

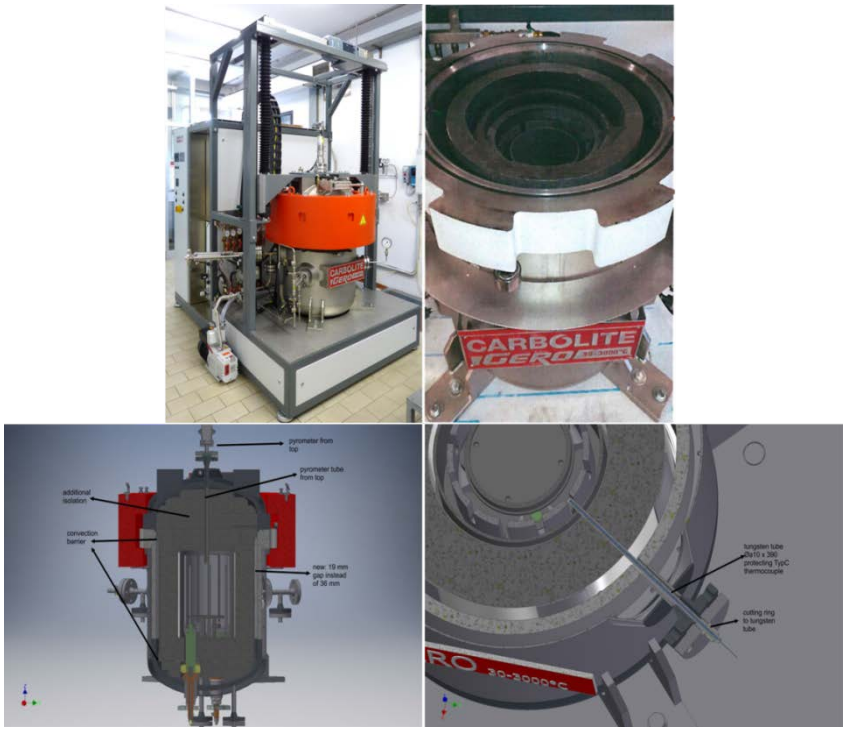

Figure 3.3 LHTG 200-300/24-1G Carbolite Gero high performance oven

- **Spark plasma sintering (SPS)**

Through this process the current passes (with values between 5000 and 20000 A, depending on the size of the sample) through the powder in a graphite mold under uniaxial pressure of 10-100 MPa in contrast to the traditional hot pressing in which heat is provided by external heating elements. Joule effect heating plays a dominant role in densifying powder compacts, significantly reducing the sintering times compared to conventional techniques. For these reasons, it is possible to obtain extremely high heating or cooling rates, order of 600 °C/min or more high and the sintering process is very fast (a few minutes). This technique is particularly suitable for densifying nano structures avoiding the grain growth that is usually present in standard densification techniques.

3.2.4 Arc-melting

It is an electric arc process (250 A) with infusible electrode (tungsten), under protection of inert gas, which can be performed with or without filler metal. The procedure is based on a torch in which the tungsten electrode is inserted through a nozzle of ceramic material and is carried on the melting bath. Fig. 3.4 shows images of the arc-melting equipment

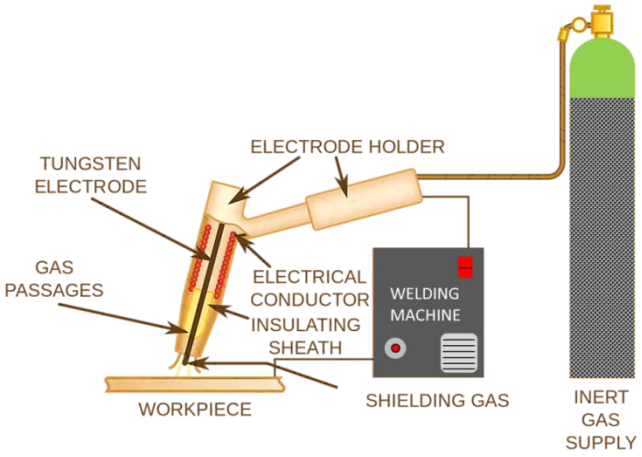

Figure 3.4 Schematic representation of arc-melting equipment

The operator moves the torch along the joint to move the melting bath, positioning the tungsten infusible electrode at maximum distance of a few millimeters and maintaining this distance stable. It is absolutely necessary to prevent electrode from coming into direct contact with the piece to be welded, otherwise the tungsten rod will "stick" to the joint and the welding will stop. This technique is able to reach high heating/cooling rate (~10 s) and very high temperature (> 3500 °C) as demonstrated by Zhang et al [23] that was able to melt TaC and HfC elements with melting point of ~3800 °C .

The equipment to perform a fusion with arc-melting therefore consists of:

- welding machine
- torch made up of: tungsten electrode, gas passage, insulating sheath, electrical conductor, electrode holder
- inert gas supply

3.2.5 Finishing

"Electron discharge machining (EDM) was used in this work to obtain the bars for the mechanical test. EDM exploits discharge phenomena between an electrode (cathode) and the rough material (anode) divided by a thin layer containing a dielectric fluid. This stage of machining is long, complex and expensive (but less than diamond tools)"[1].

3.3 Microstructural characterization

For a good knowledge on the theoretical principles and the functioning of the following analysis techniques and equipment, the documents related to the Ref.[24] have been consulted for this work. The main microstructural characterization techniques used in this work are listed below

3.3.1 X-Ray diffraction analysis

X-ray diffraction is a fundamental technique for the investigation of the fine structure of crystalline compounds. It was initially used mainly for the determination of crystallographic structures. Currently the method is applied in much wider areas such as chemical analysis, the measurement of induced stresses, the study of phase equilibria, the characterization of sub-micrometric particles and reticular defects, etc.

They are produced by bombarding with high energy electrons, emitted by a heated filament, a suitable target metal (anticathode) cooled (Fig. 3.5).

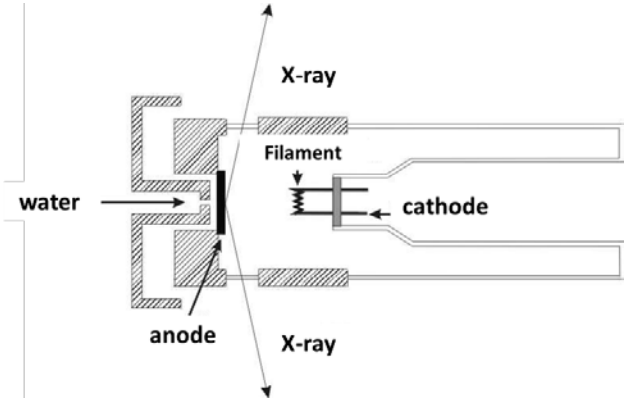

Figure 3.5 Schematic representation of an X-ray tube: filament for the emission of electrons for heating; water circulation to cool the anticathode; window (of Beryllium) for X-ray discharge

The emitted X radiation contains the continuous spectrum and the characteristic peaks of the element used as target. For X-ray diffraction experiments it is important to have

high intensity monochromatic radiation. In our case we used copper as targets which have wavelengths of 1.5418 Å (Cu Kα).

"The distances d between the crystallographic planes of crystalline materials have dimensions comparable with the wavelengths of X-rays and therefore the interaction between electromagnetic radiation X and atoms can give rise to interference phenomena.

The crystallographic plane reflects the incident radiation: it determines the angle θ for which there is constructive interference (Fig. 3.6).

The path difference between the two beams is:

$$AB + BC = 2d\ sin\theta$$

When $AB + BC = n\lambda$, with n integer, the reflected waves are in phase and constructively interfere; it follows that a light reflection is observed when the angle θ satisfies Bragg's law"[1]:

$$n\lambda = 2d\ sin\theta$$

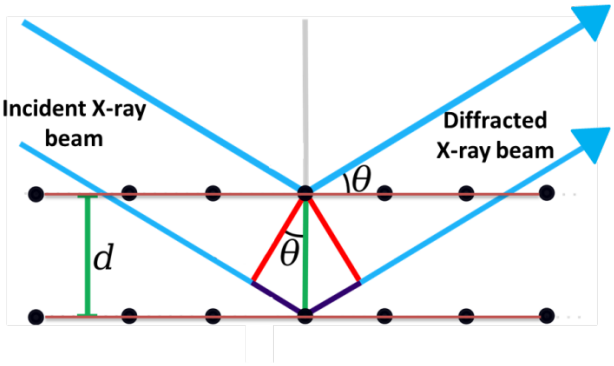

Figure 3.6 Bragg's law. Reflection of X-rays from two planes of atoms in a solid.

The most common application of X-ray diffraction is the powder diffraction method. With this technique a sample in powder form is hit by X-rays and the diffractions emerge simultaneously. A detector on a circle that moves forming an angle of 2θ with the X-ray source collects the signals diffracted by the sample, recording the position and intensity of the peak. The most common application of powder diffraction is the qualitative analysis of crystalline phases.

In this work, X-ray diffraction (XRD, mod. D8 Advance - Bruker, Germany) was used in order to found the crystalline phases of the samples. The condition was: step size of 0.04 and 0.5 seconds counting rate in the 20–100° 2θ range.

3.3.2 Scanning electron microscopy

"Scanning Electron Microscope (SEM) is a tool for seeing otherwise invisible worlds of microspace (1 micron = 10^{-6}m) and nanospace (1 nanometer = 10^{-9}m)."[24].

A schematic illustration of the main SEM components are shown in Fig. 3.7.

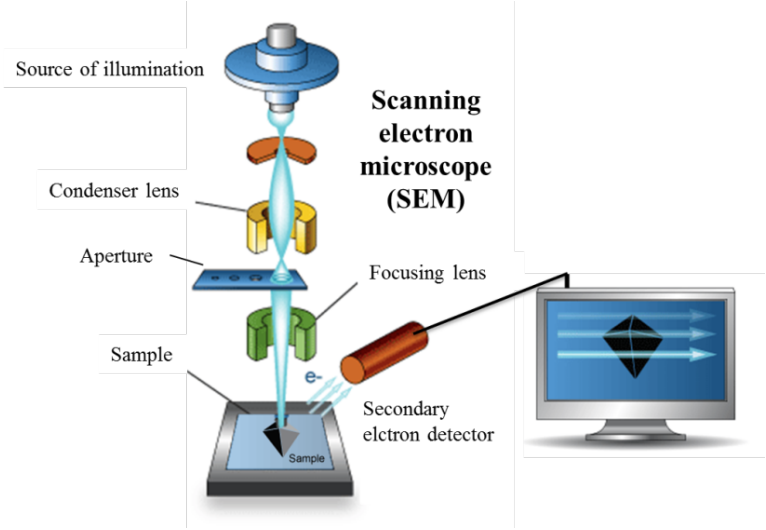

Figure 3.7 Schematic illustration components of Scanning electron microscope (SEM)[24]

"When the electron beam hits a sample it interacts with the atoms in that sample. Some electrons are bounced back out of the sample (backscattered electrons), others knock into atoms and displace electrons that, in turn, come out of the sample (secondary electrons); alternatively X-rays, and light or heat (in the sample) can be the result of these interactions (see Fig 3.8). Electron-matter interactions can be divided into two classes:

1. **Elastic scattering** – the electron trajectory within the specimen changes, but its kinetic energy and velocity remains essentially constant. The result is generation of backscattered electrons (BSE).

2. **Inelastic scattering**– the incident electron trajectory is only slightly perturbed, but energy is lost through the transfer of energy to the specimen. The result is the generation of bremsstrahlung radiation, characteristic x-ray radiation, secondary electrons and auger electrons"[24].

Fig. 3.8 shown the different signals generated by the electron-matter interaction and the portion of sample volume involved. “This shape is called an interaction volume and its depth and diameter depends on the kV as well as the density of the specimen”[24]. The interaction volume will be larger for a larger accelerating voltage, but smaller for samples with a higher mean atomic number.

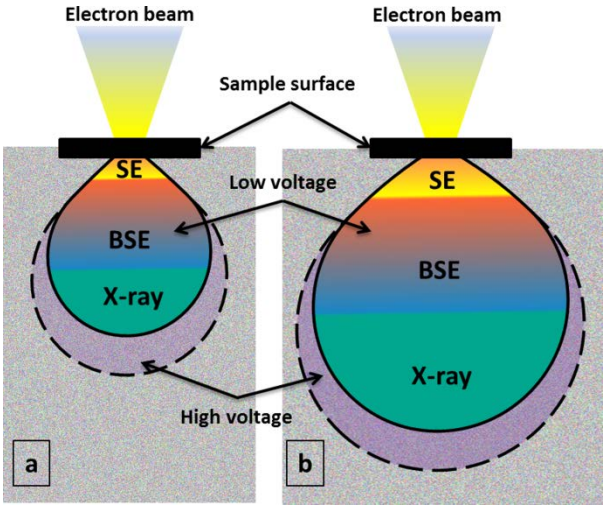

Figure 3.8 The interaction volumes of: Low voltage and high voltage of Secondary electrons (SE), Backscattered electrons (BSE) and X-ray; a) material with high atomic number b) material with low atomic number

The main advantages of SEM compared to light microscope (LM) are:

- “*Resolution at high magnification*. The best resolution possible in a LM is about 200 nm whereas a typical SEM has a resolution of better than 10 nm (typically 5 nm).
- *Depth of field* i.e. the height of a specimen that appears in focus in an image - more than 300 times the depth of field compared to the LM.
- *Microanalysis* i.e. the analysis of sample composition gives information about chemical composition”.[24]

For the microstructural analysis, the preparation of the sintering samples was carried out through an initial sectioning of materials in order to obtain a portion of cross section. The cross sections were grinded and polished until a surface finish was obtained with a 0.25 μm abrasive emulsion and some sections were broken to obtain fracture surfaces.

After polishing, the sections were analyzed with an electronic FE-SEM microscope (FESEM, Carl Zeiss Σigma NTS Gmbh Öberkochen, Germany).

Through image analysis (Image -ProAnalyzer 7.0 software) we have been determined, within their resolution limit and chemical-physical constraints, the phase, the microstructure, the porosity, grain size and phase distribution in order to investigate the influence of technological process on the products, or to characterize the morphology and microstructure of the material.

3.3.3 Energy-dispersive X-ray spectroscopy

Microanalysis is the identification of the chemical elements present either within or on the surface of an object[25].

"Energy Dispersive X-ray Spectroscopy (EDS) is a qualitative and quantitative X-ray microanalytical technique that can provide information on the chemical composition of a sample for elements with atomic number (Z) >3.

The X-rays are detected by an Energy Dispersive detector which displays the signal as a spectrum of intensity versus Energy. The energies of the characteristic X-rays allow the elements making up the sample to be identified, while the intensities of the characteristic X-ray peaks allow the concentrations of the elements to be quantified"[24].

Fig. 3.9 shown a typical spectrum obtained by energy dispersive X-ray micro-analyzer (EDS, mod. INCA Energy 300, Oxford Instruments, UK) of sample "1-all" of the Chapter 6.

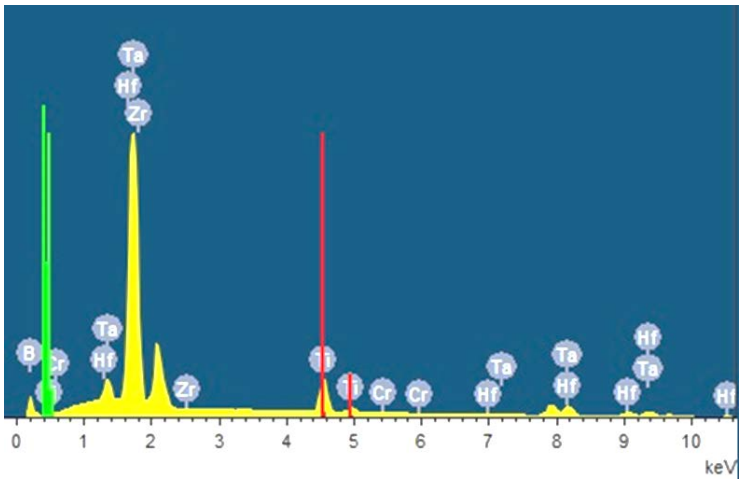

Figure 3.9 Typical spectrum obtained by EDS analysis. In this case is possible to find all element of the sample 1-all ($Hf_{0.20}$, $Zr_{0.20}$, $Ti_{0.20}$, $Ta_{0.20}$, $Cr_{0.20}$)B_2 of the Chapter 6. Red and green lines are the value of K and L shells respectively of the Ti atom.

“The electrons in the electron cloud have a stable set of energy levels, also known as electron shells (K, L, ecc...).

The production of characteristic X-rays is a two-stage process: ionization followed by relaxation. Firstly, an electron is removed from one of the inner shells of the atom by an electron from the primary beam so that the atom is ionized and in an unstable state. Secondly, the atom regains stability when an electron from an outer shell fills the inner shell vacancy and an X-ray photon is emitted. The energy of the emitted X-ray is equal to the difference between the ionization energies of the electrons involved in the transition”[24] (see Fig. 3.10).

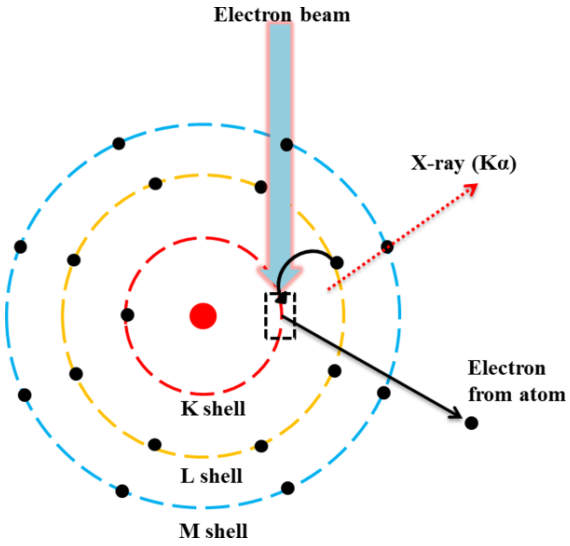

Figure 3.10 An electron from the primary beam eject an electron from the K shell of a generic atom . An electron from the L shell fills the vacancy and K_α X-ray is generated. The energy of the X-ray is equal to the ionization energy of the K shell minus the ionization energy of the L shell.

In our work, for example, for Ti atom (see Fig. 3.9), the ionization energy of the K_α shell was 4.507 keV, K_β = 4.930 KeV, the ionization energy of the L_α shell was ~0.452 keV and the ionization energy of the L_β shell iwas ~0.458 keV. Table 3.1 showed the values of ionization energy of K and L shell of the elements present in this work.

Table 3.1 Ionization energy of K and L shell

	Atomic number Z	K_α	K_β	L_α	L_β
		keV			
B	5	0.183	-	-	-
C	6	0.277	-	-	-
Ti	22	4.507	4.930	0.452	0.458
Cr	24	5.410	5.945	0.573	0.583
Zr	40	15.773	17.703	2.042	2.219
Hf	72	55.801	63.521	7.897	9.019
Ta	73	57.540	65.348	8.143	9.341
W	74	59.305	67.372	8.394	9.669

The spatial resolution of EDS analysis in the SEM depends on the size of the interaction volume, which in turn is controlled by the accelerating voltage and the mean atomic number of the sample, Z. The spatial resolution values are reported in Table 3.2 calculated through the Kanaya-Okayama equation (K-O):

$$R_{K-O} = 0.0276A\frac{E_0^{1.67}}{\rho Z^{0.89}}$$

with A the atomic mass, E_0 accelerating voltage, ρ density and Z mean atomic number of the element.

Since we have used different elements that spanning from light to heavy Z (B<C<Ti<Cr<Zr<Hf<Ta<W) the used accelerate voltage was between 5 and 15 keV. This technique was widely used in Chapter 6 in order to observe the formation of high entropy metal diborides (HEMBs). Instead of punctual analysis, the function, "EDS mapping" was carried out scanning a specific area (~0.9 - 3 mm^2) in order to observe the distribution of different elements in a mixture of solid solutions. Before to perform EDS microanalysis, the detector was calibrate with cobalt standard element. EDS microanalysis was carried out by using a working distance of 8.5 mm and an aperture of 60 μm. Spatial resolution is reported in Table 3.2 for each investigated compound.

Table 3.2 Values of spatial resolution of EDS analysis obtained by Kanaya-Okayama equation for each investigated compound and different value of accelerating voltage E_0. Z is the mean atomic number, A is the mean atomic mass, ρ is the theoretical density

	Z	**A**	**ρ**	**1 keV**	**3 keV**	**5 keV**	**10 keV**	**15 keV**	**20 keV**
		g/mol	**g/cm^3**				**μm**		
B_4C	5.2	11.051	2.52	0.03	0.18	0.41	1.31	2.57	4.15
TiB_2	16.17	23.1607	4.52	0.01	0.07	0.18	0.56	1.09	1.77
CrB_2	17.49	24.5373	5.22	0.01	0.06	0.15	0.48	0.94	1.51
ZrB_2	28.05	37.614	6.085	-	0.06	0.13	0.41	0.81	1.31
HfB_2	49.17	66.704	10.5	-	-	-	0.26	0.50	0.82
TaB_2	49.83	67.5207	12.53	-	-	-	0.22	0.42	0.68
WC	40	97.9255	15.7	-	-	-	0.30	0.59	0.96

It should be noted that calculations at low accelerating voltage values (e.g. 1 keV) are given for purely academic purposes because at low voltage counts would be too low and the signal-to-noise ratio would not be optimal for a reliable analysis.

3.4 Mechanical testing

Ceramic materials generally have a combination of high hardness, high bending strength, high elastic modulus and low fracture toughness. These mechanical properties are among the critical requirements to evaluate the performance of the material in terms of possible applications. A description of the phenomenological models and of the experimental methods of measurement of hardness, toughness, flexural strength and Young's modulus is given here[1]:

- Vickers hardness (Innovatest Falcon 505, Rupac, Netherlands) (CEN ENV 843, 1992)
- Elastic modulus (ENV 843-2) (frequency analyzer mod. 4194A, Hewlett–Packard, Yokogama, Japan)
- 4-point flexural strength at room temperature (Zwick mod. Z050) and high temperature (1200 °C) (Instron mod. 6025, Instron High Wycombe) (ENV 843-1)
- Fracture toughness at room temperature with the Chevron-Notched Beam (CNB) (Zwick mod. Z050)

All of the bars were cut by electro discharge machine (EDM) technique and no damage was not observed.

3.4.1 Hardness

"Hardness is defined as the resistance of a material to the penetration of a hard penetrator of specific geometry and charged in a defined way (CEN ENV 843, 1992).

The factors that determine the hardness are:

- interatomic bond
- type and quantity of dislocation needed for plastic deformation
- microstructural parameters such as average grain size, porosity and composition characteristics."[1]

In addition to plastic deformation, a sample subjected to penetration can give rise to incipient cracks or brittle fractures according to various mechanisms. For this work the hardness was measured by static method.

A penetrator is placed almost statically on the surface with an applied specific force for a certain time. Once the load is removed, the dimensions of the produced impression are measured with an optical microscope: the hardness is calculated from the measured dimensions and the value of the applied load.

The measurement method adopted was Vickers micro-hardness, HV 1.0 (GPa), using a standard micro-hardness tester. A hard tip whose mechanical properties are known (Vickers diamond pyramid, see Fig. 3.11) is pressed with a load of 1.96-9.81 N into a sample whose properties are unknown; the load is held constant for a period (10-15 seconds) and removed. Then, the area of the indentation in the sample was measured, using light microscopy.

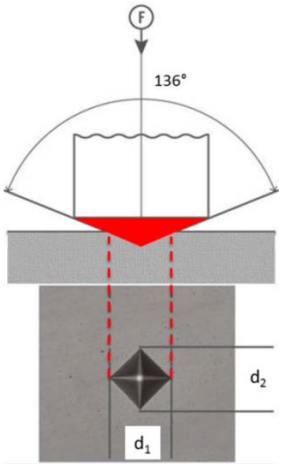

Figure 3.11 Vickers hardness indentation

"The hardness HV1.0 is defined as the maximum load F (kgf) divided by the residual indentation area d^2 (mm) as indicated by the following formula"[1]:

$$HV = \frac{2Fsin\frac{136°}{2}}{d^2} = 1.8544\frac{F}{d^2}$$

In this work the hardness was measured by Vickers indentation method by applying a load of 1.96 N (200 g), 4.90 N (500 g) or 9.8 N (1000 g). The load was held constant for 10-15 seconds and removed. Then, the area of the indentation in the sample was measured, using light microscopy.

3.4.2 Elastic modulus

The elastic modulus or (*Young's modulus)* E (GPa) for an amorphous or polycrystalline solid is defined by Hook's law as the ratio of the stress (force per unit area) to the corresponding strain (deformation) in a material under tension or compression[26,27].

$$\sigma = E\varepsilon$$

where σ is the stress (F/mm^2) and ε the strain.

The elastic modulus is basically the slope of the stress-strain curve within the elastic range, the straight-line portion of the curve (Fig. 3.12), and measures the difficulty in starting to deform the material in elastic behavior.

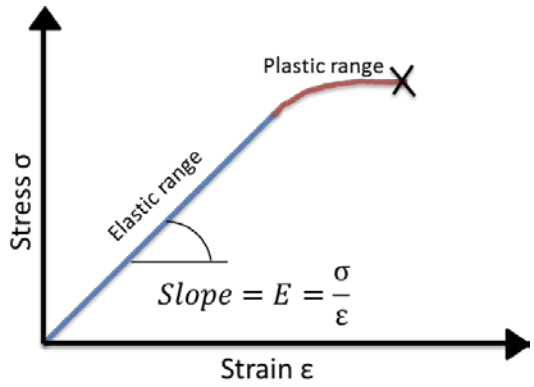

Figure 3.12 Stress-strain diagram

“The methods used to measure the elastic modulus are divided into static and dynamic. With static methods a known load is imposed on the sample by a dynamometer and the induced deformation is measured by strain gauges (small metal coils whose electrical resistance changes as the sample section changes); these methods are not recommended for very rigid materials, such as ceramics, because it is necessary to apply very high loads to arise an appreciable signal. For this reason, dynamic methods are preferred.”[1]

In this work Young’s modulus was measured by the resonance frequency in bending method using a universal frequency analyzer. “E” was calculated by the following relationship:

$$E = 0.946\left(\frac{mf^2}{b}\right)\left(\frac{l}{h}\right)^3\left[1 + 6.585\left(\frac{h}{l}\right)^2\right]\cdot 10^{-9}$$

where m is the mass (g), f_n the natural frequency (Hz), and b, l and h are the width, length and thickness (mm) respectively [28,29] (8.0 x 28.0 x 0.8)

This method, unlike static methods, allows the analysis of elastic and possibly inelastic parameters in a wide range of temperatures, it is not destructive and is more reliable because it provides values averaged over the entire volume of the sample.

3.4.3 Flexural strength

The concept of mechanical resistance can be defined as the stress, imposed on a solid, capable of producing a complete separation along a plane between its elementary particles.

The flexural strength of a sintered sample depends on many factors: size, shape and distribution of pores, agglomerates, and grains, grain boundary features, surface flaws, etc..

Pores reduce the cross-sectional area over which the load is applied, and can act as stress concentrators relates strength an porosity:

$$\sigma_P = \sigma_0 e^{-BP}$$

where σ_P and σ_0 are the strength with and without of porosity (MPa), respectively, B is a constant depending on the distribution of pores, and P is the volume fraction of pores.

“The agglomerates, stuck during a rapid densification, can generate stresses within the surrounding areas inducing the formation of voids and cracks. Large grains can produce mismatch in thermal expansion and elastic modulus and act as flaws in homogeneous matrix.”[1]

Strength is also affected by grain size, typically decreasing with the increase of the grain dimensions, therefore sintering parameters such as temperature and pressure must be controlled in order to avoid excessive grain growth.

From the experimental point of view, the resistance is measured and classified according to different type of test:

- tensile strength
- compressive strength
- flexural strength.

In the present work, four points bending strength tests at room temperature (RT) and high temperature (HT) were carried out on test bars 25 x 2.5 x 2 mm (length by width by thickness, respectively) with long edges chamfered using a semi-articulated test fixture with a lower span of 20 mm and an upper span of 10 mm using a screw-driven testing machine

The flexural strength at high-temperature was tested with heated up to 1200°C with a rate of 10°C/min under a constant flow of argon (3.5 l/min) under flowing argon protective gas. Before the bending test, a soaking time of 18 min was set to reach thermal equilibrium. For rectangular cross sections, the fracture strength in 4-point bending is given by the following equation [27,30]:

$$\sigma = \frac{3F(L - L_0)}{2bd^2}$$

Where F is the force, L and L_0 are the outer and inner support span respectively (for three point bending, $L_0 = 0$), and b and d are the width and thickness respectively.

3.4.4 Fracture toughness

Fracture toughness, K_{Ic} ($MPa \cdot m^{0.5}$), is the measure of the resistance to fracture of a material containing a crack.

Brittle fracture is characteristic of materials with low fracture toughness values.

"An inverse V notched is introduced in rectangular bar by very sharp diamond blades and, when the load is applied, the crack starts to propagate from the tip of the triangular notch.

Munz *et al.*[31] determined the relationships which allow to calculate K_{Ic} from the maximum load (P_{max}) measure in 4-pt bending test of a chevron-notched sample of known geometry. The CNB model and formulas are reported in Fig. 3.13 and in following equations"[1].

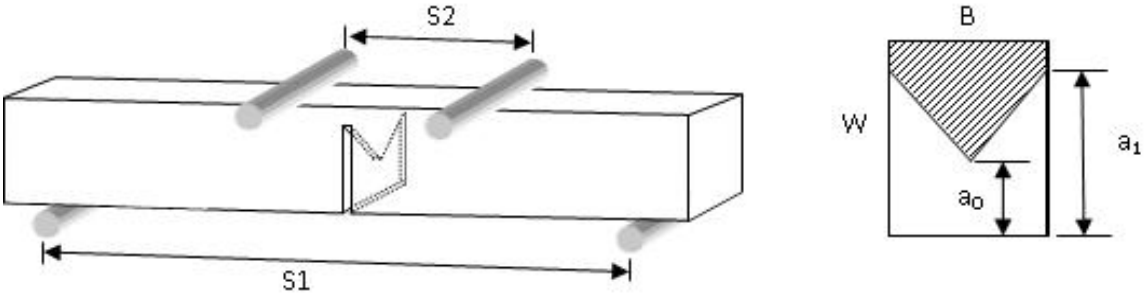

Figure 3.13 Chevron notched beam model

Munz's relationship

$$K_{Ic} = Y^* \frac{P_{max}(S_1 - S_2)}{BW^{3/2}}$$

$$Y^* = (3.08 + 5\alpha_0 + 8.33\alpha_0^2)\frac{(S_1 - S_2)}{W}\left(1 + 0.007\sqrt{\frac{S_1 S_2}{W^2}}\right)\left(\frac{\alpha_1 - \alpha_0}{1 - \alpha_0}\right)$$

K_{Ic} fracture toughness, (MPa·m$^{0.5}$);

P_{max} maximum peak of force, (mN);

S_1 distance between the lower span, (m);

S_2 distance between the upper span, (m);

B specimen width, (m);

W specimen thickness, (m);

a_0 a_0/W;

a_1 a_1/W;

"In this work the fracture toughness (K_{Ic}) was evaluated using the method of chevron notched beam (CNB) in flexure. The test bars, 25 x 2 x 2.5 mm^3 (length by width by thickness, respectively), were notched with a 0.1 mm-thick diamond saw; the chevron-notch tip depth and average side length were about 0.12 and 0.80 of the bar thickness, respectively"[1]. The specimens were fractured in four-point fixture with a lower span of 20 mm and an upper span of 10 mm. The specimens, three for each composite, were loaded with a crosshead speed of 0.05 mm/min. The "slice model" equation of Munz et al.[31] was used to calculate K_{Ic}.

3.5 Method of preparation and characterization of the samples

3.5.1 Production and analysis of B_4C/TiB_2 based materials (high hardness)

Commercial powders of B_4C, TiB_2, n-SiC, β-SiC, Si_3N_4, TiO_2 and WC, were used to produce the composition shown in Chapter 4.

The powders were subjected by soft (SB) and high-energy milling (HEBM) cycles by the following procedures:

- SB using WC milling media (size 10 mm), the homogenization of the powders was carried out in wet condition in a polyethylene bottle and EtOH at low speed for 24 hours, with grinding media.
- HEBM using WC milling media (size 0.6 mm), the powders, after homogenization by SB, were ground using a high-energy planetary mill in a WC jar according to the following protocol:

- suspension of the homogenized powder in ethyl alcohol;
- addition of tungsten carbide grinding media;
- grinding at 400 rpm for 5 minutes, cooling pause of 30 minutes

Repeating the last step six times in order to obtain a total grinding time of 30 minutes. The next step for both procedures consisted in drying the powders by means of a rotary evaporator at 120 rpm in a water bath at 80 °C and -40 mmHg of vacuum to avoid the preferential sedimentation of heavier powder. Once dried, the powders were sieved at 250 μm.

The scope of HEBM step, in addition to reducing the particles, was also to introduce surface defects that made powders more reactive and therefore easier to sinter.

Samples, with the basic mixture (50v% B_4C - 50v% TiB_2) and sintered by HP (Table 3.3), were modified with different sintering aids, such as: α-SiC, β-SiC, Si_3N_4. Pure B_4C and TiB_2 as basic materials were also produced, which served as reference materials (E, F).

B_4C/TiO_2 powders mixture was also prepared to produce TiB_2 in the final microstructure by exploiting the reaction with carbon already presents in the B_4C powder:

$$2TiO_2 + B_4C + 3C \rightarrow 2TiB_2 + 4CO$$

The sintering reaction was exploited to facilitate the densification process.

All HP samples were prepared by uniaxial pressing the dry powder mixtures up to 250 MPa in a circle stainless steel mold of 45 mm of diameter to obtain green samples.

PLS/GPS samples (Table 3.3) were prepared starting from mixture of B_4C-TiB_2 that spanning from B_4C-rich composition to TiB_2-rich composition. The powders were subjected to HEBM cycles in order to reduce the mean grain size from the micrometric range to the sub-micrometric range. The green pellets were prepared by uniaxial pressure up to 25 MPa in stainless steel molds (12-45 mm of diameter) and subsequent were CIPed at 400 MPa. In this way, relative densities of about 60-65% were reached. In fact, PLS and GPS need to start from high dense "green body" since more high is the contact between the particles and better densification will be achieved.

Table 3.3 Compositions chosen to select the best sintering additive and sintering technique

Name	Composition (v%)	Sintering aids	Mixing/milling	Sintering
A	50 B_4C - 40 TiB_2 - 10 SiC(n)	SiC	SB	HP
B	50 B_4C - 40 TiB_2 - 10 SiC(β)	SiC		HP
C	50 B_4C - 45 TiB_2 – 5 Si_3N_4	Si_3N_4		HP
D	50 B_4C - x TiO_2	TiO_2	HEBM	HP
E	100 B_4C	no		HP
F	100 TiB_2	no		HP
G	100 B_4C			PLS/GPS
H	87.5 B_4C - 12.5 TiB_2			PLS/GPS
I	75 B_4C - 25 TiB_2			PLS/GPS
L	25 B_4C - 75 TiB_2			PLS

Other compositions, spanning from B_4C-rich compositions to TiB_2-rich compositions, were studied in order to explore the effect of WC addition (see Table 3.4). WC was directly introduced in the starting powder mixture (B50-2 sample) or exploiting the wearing of the WC milling media (HEBM samples). All the samples were sintered by hot pressing, trying to find the best conditions to obtain the maximum densification and to optimize the microstructural features such as grain size. The amount of incorporated WC was determined by weighting the powders before and after the milling procedure (Table 3.4).

Table 3.4. Compositions chosen to investigate the influence of the WC addition

Name	Composition (v%)	Mixing/milling	Incorporated WC (v%)	Sintering
B50-1	50 B_4C - 50 TiB_2	SB	Traces	HP
B50-2	50 B_4C - 45 TiB_2 - 5 WC		Traces	
B50-3	50 B_4C - 50 TiB_2	HEBM	~1.5	
B25-3	25 B_4C - 75 TiB_2		~1.6	
B75-3	75 B_4C - 25 TiB_2		~2.1	

- *Sintering*

The HP mixtures, sintered in a graphite mold by using an induction heated hot pressing machine, were investigated in order to assess the effect of:

- heat treatment;
- sintering aids;
- powders refinement.

PLS/GPS mixtures was designed in order to evaluate the influence of:

- sintering temperature;
- dwell time;
- isostatic gas pressure.

In particular, for PLS and GPS techniques, the aim was to find the most suitable temperatures and dwell time to obtain an ideal densification of 100% and avoid grain overgrowth. Once the best temperature-time conditions were found, an accurate analysis was carried out in order to assess the effect of the applied gas pressure. The aim of this investigation was to understand if it was possible to decrease the dwell times so that to make the GPS technique more competitive compared to HP and PLS techniques.
The designed heat treatments for HP, PLS and GPS are reported in the following:

- HP: from RT up to 1750-1930 °C (depending on the mixture) at 35 °C / min. Mechanical pressure of 30 MPa was applied from 900 °C and increased up to 40 MPa only for reaction sintering (D material). Dwell time was 10-20 minutes.
- PLS: from RT up to 1800 °C in vacuum at 10 °C/min. Inert gas (Ar) at 1 bar pressure was introduced above 1800 °C up to T_{max}. The dwell times at T_{max} was 60-120 minutes.
- GPS: from RT up to 1800 °C in vacuum at 10 °C/min. Inert gas (Ar) at 50 bar pressure was introduced above 1800 °C up to T_{max} and kept constant for the dwell time of 60 minutes.

Table 3.5 shows the main analysis conducted for the high hardness based materials

Table 3.5 Methods and characterizations of high hardness based materials

S.A.	ρ_{green}	ρ_{bulk}		SEM	EDS	XRD	σ		K_{Ic}	HV			E
	Geom.	Arch.	I.A.				RT	1200 °C	RT	1.96 N	4.9 N	9.8 N	RT
X	**X**	**X**	**X**	**X**	**X**	**X**	**X**	**X**	**X**			**X**	**X**

S.A.= Sedimentation analysis, Geom.= geometric density, Arch.= archimede's density, I.A.= Image analysis relative density

3.5.2 Production and analysis of UHTCMC based materials (high toughness)

Carbon fibers were used as substrate in EPD. Ethanol-based colloidal suspensions at 2 wt% of either ZrB_2 or TiB_2 (commercial powders, see 3.2.1 section) with a polyacrylate (PEI) [32] for EPD process were prepared by ball-milling for 3 h in a polyethylene bottle with SiC balls. Depositions of ZrB_2 or TiB_2 on individual unidirectional (UD) Cf fabrics were performed in plane parallel cell geometry and cathodic modality, keeping the working electrode 10 mm apart from the stainless steel counter electrode and applying constant DC potentials. After EPD process, the fabrication of carbon fibre reinforced composites (UHTCMC) have required several steps before obtaining the final material. The coated fabrics were infiltrated with slurries having compositions ZrB_2 + 5 v% B_4C or TiB_2 + 5 v% B_4C, subsequently stacked in 0/0 configuration and dried using the vacuum bagging technique at 90 °C for 1h. Commercial B_4C (see 3.2.1 section) was added as sintering aid, according to studies [33]. For the sake of comparison, an uncoated sample was also produced with the same composition of ZrB_2+5 v% B_4C, just using the slurry impregnation and sintering [34]. Three different combinations of coating and matrix were produced, see Table 3.6.

Table 3.6 Compositions of UHT-CMC materials

Sample ID	Matrix	coating
ZZ	ZrB_2 / 5v% B_4C	ZrB_2
ZT	ZrB_2 / 5v% B_4C	TiB_2
TZ	TiB_2 / 5v% B_4C	ZrB_2
Z	ZrB_2 / 5v% B_4C	Uncoated

The schematic flow diagram of the green shaping is illustrated in Fig. 3.14.

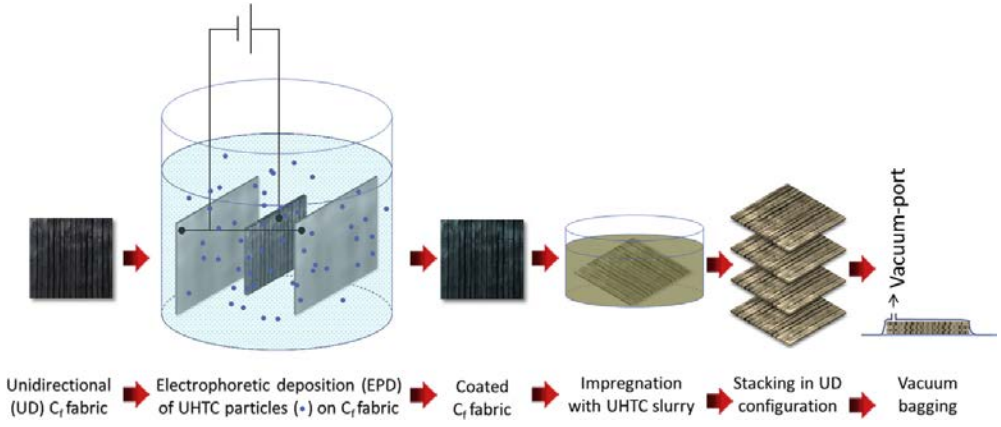

Figure 3.14 Schematic flow diagram of green shaping.

- *Sintering*

Sintering was carried out by hot pressing in low vacuum range using an induction-heated graphite die (square 30 x 30 mm), heating rate 35 °C/min with a uniaxial pressure of 30-40 MPa, at 1800-1900 °C with 10 minutes of dwell time. Fiber volume content (FVC) was calculated by multiplying fiber mass per unit area, times the layers' number and sample area.

Table 3.7 shows the main analysis conducted for the high toughness based materials

Table 3.7 Methods and characterizations of high toughness based materials

S.A.	ρ_{green}	ρ_{bulk}		SEM	EDS	XRD	σ		K_{Ic}	HV			E
	Geom.	Arch.	I.A.				RT	1200 °C	RT	1.96 N	4.9 N	9.8 N	RT
		X	**X**	**X**			**X**		**X**				

S.A.= Sedimentation analysis, Geom.= geometric density, Arch.= archimede's density, I.A.= Image analysis relative density

3.5.3 Production and analysis of high entropy metal diborides (high entropy)

Five commercial powders of transition metal diborides were used to prepare six equimolar mixture showed in Table 3.8. The starting equimolar powders were mixed using mortar and pestle and rotary milled with no milling media.

Table 3.8 High entropy metal diboride samples.

Label	**Starting composition mol%**
1 - all	$(Hf_{0.20}, Zr_{0.20}, Ti_{0.20}, Ta_{0.20}, Cr_{0.20})B_2$
2 - CrB_2	$(Hf_{0.25}, Zr_{0.25}, Ti_{0.25}, Ta_{0.25})B_2$
3 - TaB_2	$(Hf_{0.25}, Zr_{0.25}, Ti_{0.25}, Cr_{0.25})B_2$
4 - TiB_2	$(Hf_{0.25}, Zr_{0.25}, Cr_{0.25}, Ta_{0.25})B_2$
5 - ZrB_2	$(Hf_{0.25}, Cr_{0.25}, Ti_{0.25}, Ta_{0.25})B_2$
6 - HfB_2	$(Cr_{0.25}, Zr_{0.25}, Ti_{0.25}, Ta_{0.25})B_2$

- *Sintering and melting*

All mixtures were pre-sintered in a Spark plasma sintering furnace (Chenhua 10–20 SPS furnace, China), at 1600 °C in low vacuum (5 Pa) under a pressure of 25 MPa, heating rate of 80 °C/min and dwelling time of 10 minutes, in order to clean borides from oxide impurities as much as possible. From each of the 6 pre-sintered pellets, 10

smaller pieces with a volume of about 40 mm^3 were obtained for the arc-melting experiments in order to have similar heating and cooling rates.

All samples were melted on a water-cooled copper crucible using arc melting under argon flow, with purity of 99.999 %, applying a current of 100 A for 10-20 seconds. The argon flow was maintained for 10 seconds after switching off the current in order to protect the samples from the oxidation during the free cooling. The samples were re-melted 5 times in order to homogenize the mixture as much as possible during melt formation.

Table 3.9 shows the main analysis conducted for the high entropy metal diborides based materials

Table 3.9 Methods and characterizations of high entropy metal diborides based materials

S.A.	ρ_{green}	ρ_{bulk}		SEM	EDS	XRD	σ		K_{Ic}	HV			E
	Geom.	Arch.	I.A.				RT	1200 °C	RT	1.96 N	4.9 N	9.8 N	RT
		X		**X**	**X**	**X**				**X**	**X**	**X**	

S.A.= Sedimentation analysis, Geom.= geometric density, Arch.= archimede's density, I.A.= Image analysis relative density

3.6 References

1. Silvestroni, L. Development and characterization of non-oxide ceramic composites for mechanical and tribological applications. (University of Bologna, 2009). doi:10.6092/unibo/amsdottorato/2045
2. Boccaccini, A. R. & Zhitomirsky, I. Application of electrophoretic and electrolytic deposition techniques in ceramics processing - Part 2. *InterCeram Int. Ceram. Rev.* **54**, 242–246 (2005).
3. Zhitomirsky, I. & Gal-Or, L. Formation of hollow fibers by electrophoretic deposition. *Mater. Lett.* **38**, 10–17 (1999).
4. Sarkar, P. & Nicholson, P. S. Electrophoretic Deposition (EPD): Mechanisms, Kinetics and Application to Ceramics. *Journal of American Ceramic Society* **79**, 1987–2002 (1996).
5. Besra, L. & Liu, M. A review on fundamentals and applications of electrophoretic deposition (EPD). *Prog. Mater. Sci.* **52**, 1–61 (2007).
6. Powers, R. W. The Electrophoretic Forming of Beta-Alumina Ceramic. *J. Electrochem. Soc.* **122**, 490 (2006).
7. R.V. Subramanian and Eric A. Nyberg. Zirconia and organotitanate film formation on graphite fiber reinforcement for metal matrix composites. *J. Mater. Res.* **7**, 677–688 (1992).
8. Lee, J.-H., Gil, G.-Y. & Yoon, D.-H. Fabrication of SiCf/SiC Composites using an Electrophoretic Deposition. *J. Korean Ceram. Soc.* **46**, 447–451 (2009).
9. Zhitomirsky, I. Electrophoretic and electrolytic deposition of ceramic coatings on carbon fibers. *J. Eur. Ceram. Soc.* **18**, 849–856 (1998).
10. Davis, J. B., Lofvander, J. P. A., Evans, A. G., Bischoff, E. & Emiliani, M. L.

Fiber Coating Concepts for Brittle-Matrix Composites. *J. Am. Ceram. Soc.* **76**, 1249–1257 (1993).
11. Yoshida, K. *et al.* Interfacial control of uni-directional SiCf/SiC composites based on electrophoretic deposition and their mechanical properties. *Compos. Sci. Technol.* **72**, 1665–1670 (2012).
12. Gonsalves, K. E., Yazici, R. & Han, S. Ceramic coatings for graphite fabrics by metalorganic pyrolysis. *J. Mater. Sci. Lett.* **10**, 834–837 (1991).
13. Galizia, P., Failla, S., Zoli, L. & Sciti, D. Tough salami-inspired Cf/ZrB2 UHTCMCs produced by electrophoretic deposition. *J. Eur. Ceram. Soc.* **38**, 403–409 (2018).
14. Zhang, X., Hou, Y., Hu, P., Han, W. & Luo, J. Dispersion and co-dispersion of ZrB2 and SiC nanopowders in ethanol. *Ceram. Int.* **38**, 2733–2741 (2012).
15. Lee, S. H., Sakka, Y. & Kagawa, Y. Dispersion behavior of ZrB2 powder in aqueous solution. *J. Am. Ceram. Soc.* **90**, 3455–3459 (2007).
16. Zhang, Y. & Lin, X. Aqueous Electrophoretic Deposition of ZrB2-SiC Nano-composites in Pulsed DC Electric Fields. *Adv. Automob. Eng.* **01**, 1–3 (2016).
17. Tang, F., Uchikoshi, T., Ozawa, K. & Sakka, Y. Dispersion of SiC suspensions with cationic dispersant of polyethylenimine. *J. Ceram. Soc. Japan* **587**, 584–587 (2005).
18. Tabellion, J. & Clasen, R. Electrophoretic deposition from aqueous suspensions for near-shape manufacturing of advanced ceramics and glasses - Applications. *J. Mater. Sci.* **39**, 803–811 (2004).
19. Negishi, H. Uniform and ultra low-power electrophoretic deposition of silica powder using a nonflammable organic solvent. *J. Eur. Ceram. Soc.* **36**, 285–290 (2016).
20. Mendoza, C., González, Z., Castro, Y., Gordo, E. & Ferrari, B. Improvement of TiN nanoparticles EPD inducing steric stabilization in non-aqueous suspensions. *J. Eur. Ceram. Soc.* **36**, 307–317 (2016).
21. Galizia, P., Ciuchi, I. V., Gardini, D., Baldisserri, C. & Galassi, C. Bilayer thick structures based on CoFe2O4/TiO2 composite and niobium-doped PZT obtained by electrophoretic deposition. *J. Eur. Ceram. Soc.* **36**, 373–380 (2016).
22. Zehbe, R., Mochales, C., Radzik, D., Müller, W. D. & Fleck, C. Electrophoretic deposition of multilayered (cubic and tetragonal stabilized) zirconia ceramics for adapted crack deflection. *J. Eur. Ceram. Soc.* **36**, 357–364 (2016).
23. Zhang, Z. *et al.* Arc melting: a novel method to prepare homogeneous solid solutions of transition metal carbides (Zr, Ta, Hf). *Ceram. Int.* **45**, 9316–9319 (2019).
24. Australia, M. Microscopy training. Available at: https://myscope.training.
25. Goldstein, J. et al. Scanning Electron Microscopy and X-ray Microanalysis. Scanning Electron Microscopy and Xray Microanalysis. (2003). doi:doi:10.1007/978-1-4615-0215-9
26. Roylance, D. Stress-strain Curves. Test. (2001). doi:doi:10.1361/aac
27. Vable, M. Mechanical Properties of Materials. *Springer* (2012). doi:10.1007/978-94-007-4342-7
28. Quinn, G. D. & Swab, J. J. Elastic Modulus by Resonance of Rectangular Prisms Corrections for Edge Treatments. *J. Am. Ceram. Soc.* (2000). doi:10.1111/j.1151-2916.2000.tb01192.x
29. ASTM. ASTM E1875-08 Standard Test Method for Dynamic Young ' s Modulus , Shear Modulus , and Poisson's Ratio by Sonic Resonance. *ASTM B. Stand.* (2001). doi:10.1520/E1875-08.2

30. Davidge, R. W. & Evans, A. G. The strength of ceramics. *Mater. Sci. Eng.* (1970). doi:10.1016/0025-5416(70)90064-9
31. Munz, D. G., Shanno, J. L. & Bubsey, R. T. Fracture toughness calculation from maximum load in four point bend tests of chevron notch specimens. *Int. J. Fract.* **16**, 137–141 (1980).
32. Medri, V., Capiani, C. & Gardini, D. Slip casting of ZrB2-SiC composite aqueous suspensions. *Adv. Eng. Mater.* **12**, 210–215 (2010).
33. Sciti, D., Silvestroni, L., Medri, V. & Monteverde, F. Sintering and densification mechanisms of ultra-high temperature ceramics. in *Ultra-High Temperature Ceramics: Materials for ExtremeEnvironment Applications* (eds. Fahrenholtz, W. G., Wuchina, E. J., Lee, W. E. & Zhou, Y.) 112–143 (2014). doi:10.1002/9781118700853.ch6
34. Zoli, L., Vinci, A., Galizia, P., Melandri, C. & Sciti, Di. On the thermal shock resistance and mechanical properties of novel unidirectional UHTCMCs for extreme environments. *Sci. Rep.* **8**, 1–9 (2018).

4. High hardness structural

4.1 B_4C/TiB_2 materials (Hot pressing)

The effect of sintering additives (eg. nano-SiC, β-SiC, Si_3N_4, TiO_2 and WC), during hot pressing of B_4C-TiB_2 matrix spanning from B_4C-rich to TiB_2-rich compositions, was investigated. SiC or Si_3N_4 were chosen for their low density. The effect of in-situ formation of TiB_2 from TiO_2 powder on reactive hot pressing of the B_4C was also investigated. Pure B_4C an TiB_2 were produced as basic materials. Their densification was improved by reducing the mean particle size through high energy ball milling (HEBM) of the starting powders.

We also explored the effect of WC addition by designing different processing methods in order to obtain the best densification and grain size distribution.

WC addition took inspiration from pioneering works on the effect of WC doping on ZrB_2 [1] where the formation of a Zr-B-W solid solution led to unprecedented strength of ~1 GPa.

The most effective amount of additive was identified by looking at matrix densification, grain refinement, and microstructure homogeneity in terms of grain and pore size distribution and dispersion. Mechanical properties were evaluated for all those materials characterized by a residual porosity less than 5 v%.

4.1.1 B_4C/TiB_2 with sintering aids

4.1.1.1 Raw materials analysis

B_4C – XRD analysis confirmed that B_4C was pure and stoichiometric: the peaks corresponded to those reported in JCPDF 35-0798 of B_4C and no secondary peaks were detected (Fig. 4.1).

In agreement with the data supplied by the producer, SEM analysis (Fig. 4.2) shows fine particles smaller than 2 μm, and a coarser fraction of about 4 μm.

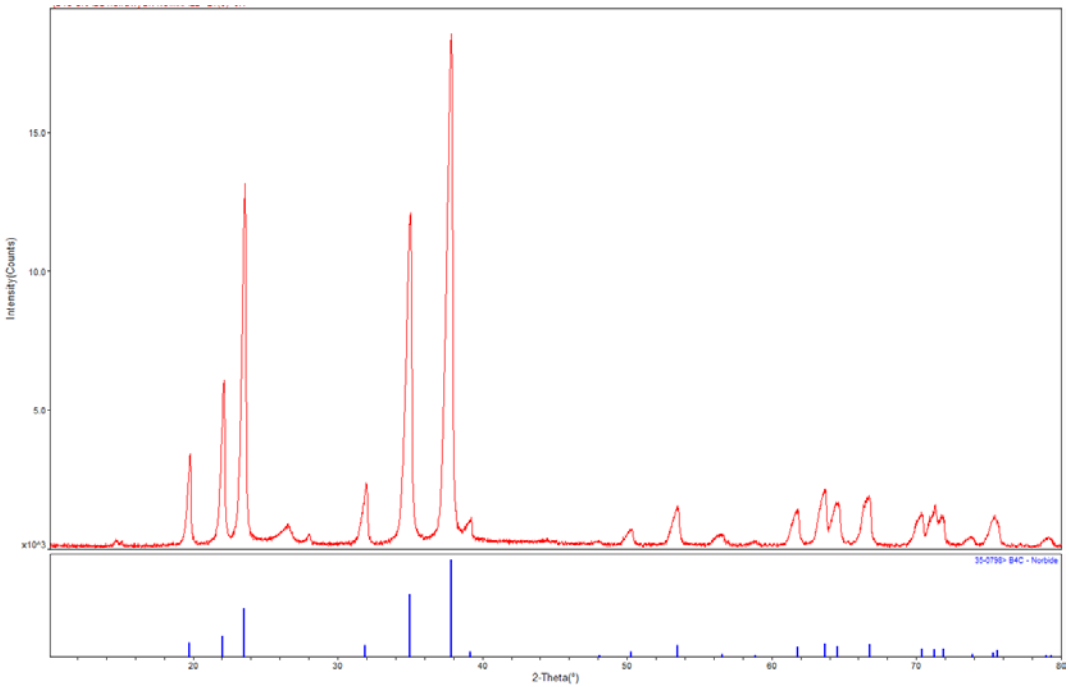

Figure 4.1 Diffraction pattern of commercial powder of B_4C-Starck grade HS

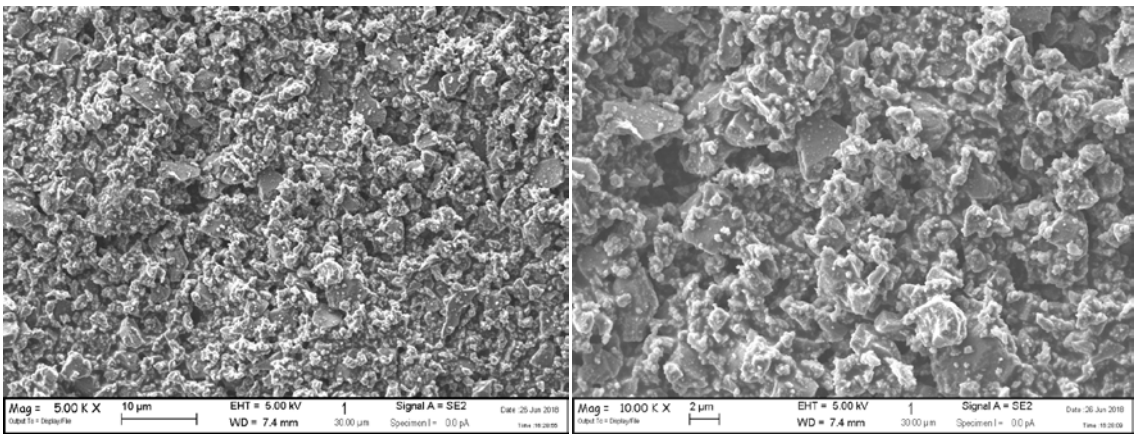

Figure 4.2 SEM images at different magnification of commercial powder of B_4C-Starck grade HS.

TiB_2 – From the cumulative curve (Fig. 4.3a) it was measured that 50% of the particles were smaller than 2.6 µm (D_{50}) and most of the particles had dimensions between 0.91 and 4.34 µm (D_{10} and D_{90} respectively).

From the frequency distribution curve (Fig. 4.3b) it can be seen a smaller peak at about 0.4 µm, which however represented less than 0.5% of the total mass of the particles.

XRD diffraction pattern confirmed that the compound was pure and stoichiometric (Fig. 4.4). The peaks corresponded to those reported in JCPDF 75-0967 of TiB_2 and no secondary peaks were present. SEM analysis (Fig. 4.5), in agreement with the

sedimentometer analysis, showed particles size about 2 µm with a regular shape and a smaller fraction of finer particles. TiB_2 particles are coarser than those of B_4C.

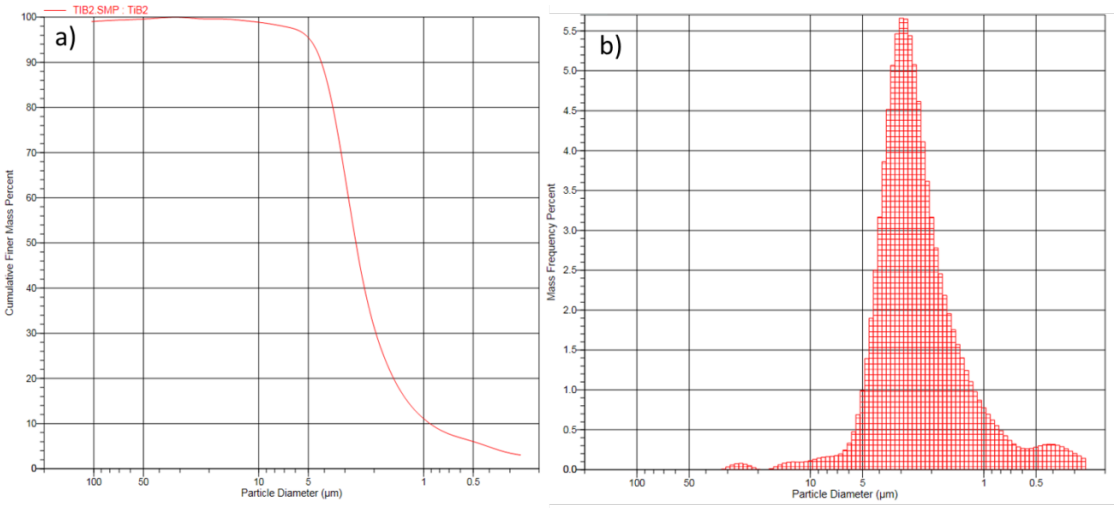

Figure 4.3 a) Cumulative curve of commercial powder of TiB_2-Starck grade F. b) Frequency distribution curve of commercial powder of TiB_2-Starck grade F.

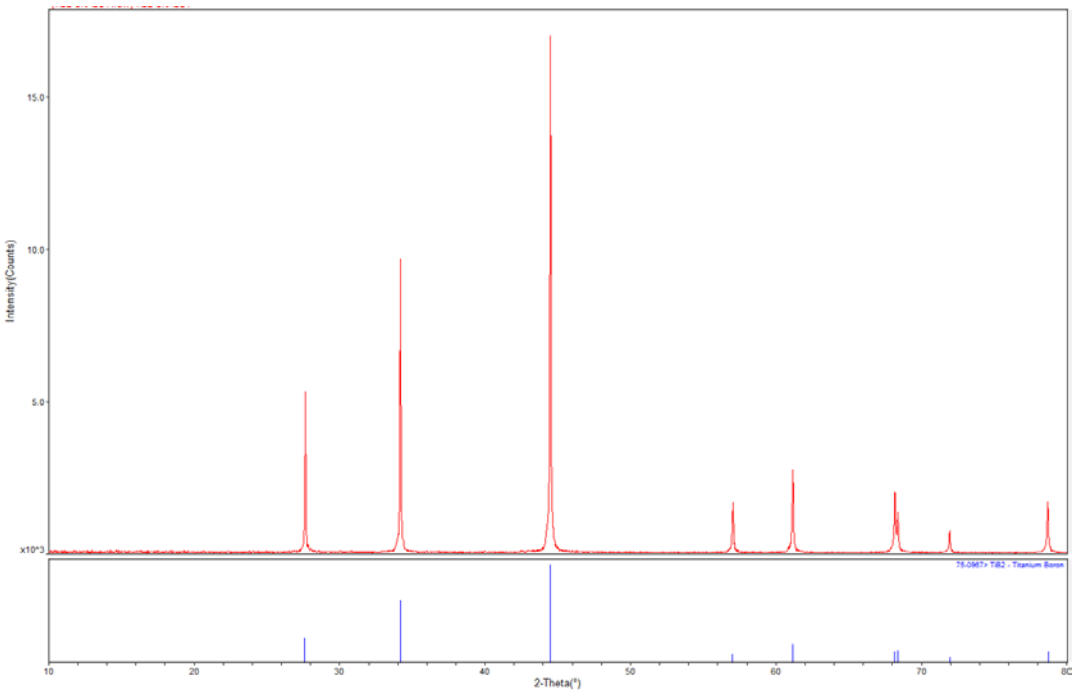

Figure 4.4 Diffraction pattern of commercial powder of TiB_2-Starck grade F.

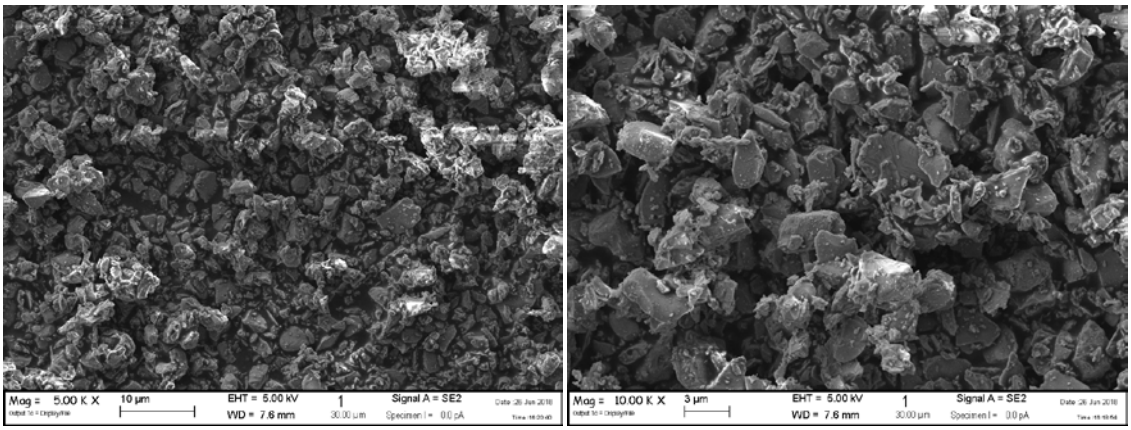

Figure 4.5 SEM images at different magnification of commercial powder of TiB_2-Starck grade F.

4.1.1.2 Sintering behavior

The three mixtures A - B - C (Table 4.1) were sintered in HP with the same cycle up to 1930 °C. In Fig. 4.6, which shows the temperature and shrinkage curves as a function of time, it was possible to observe a reduction of the densification onset (1630 °C) with the addition of n-SiC if compared to β- SiC and Si_3N_4 (1660 °C).

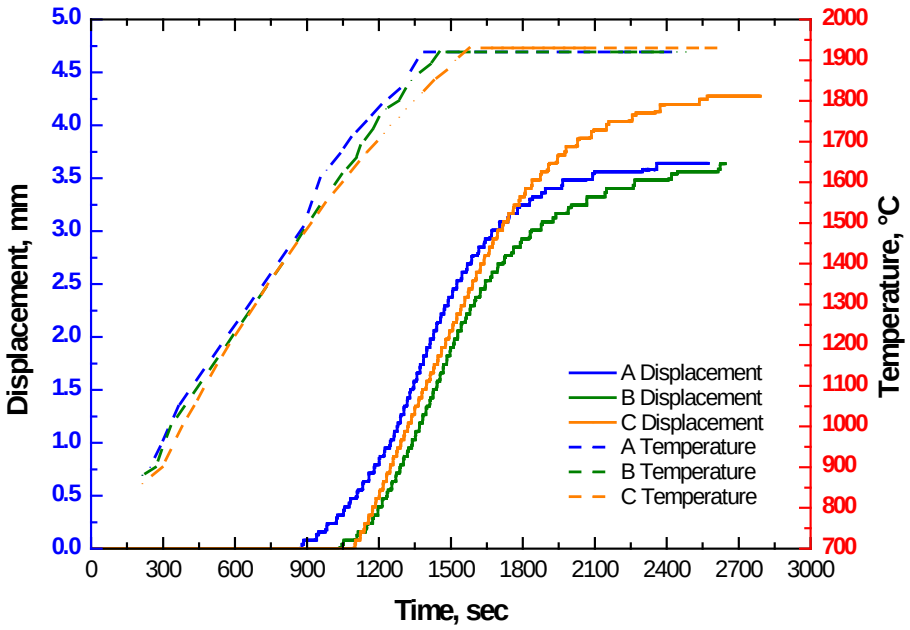

Figure 4.6 Temperature and Shrinkage Vs Time for A, B, and C materials

D material was heated up to 1800 °C with a maximum load of 40 MPa. In this case the pressure was higher than other cycles in order to favor the reaction sintering process. In Fig. 4.7, which shows the temperature and shrinkage curves as function of time, it was possible to observe a start densification temperature of 1410 °C. The decrease of

densification onset can be attributed to the (i) WC coming from the high energy milling, (ii) to the reduction of the particle size, and (iii) to the reaction occurred during sintering.

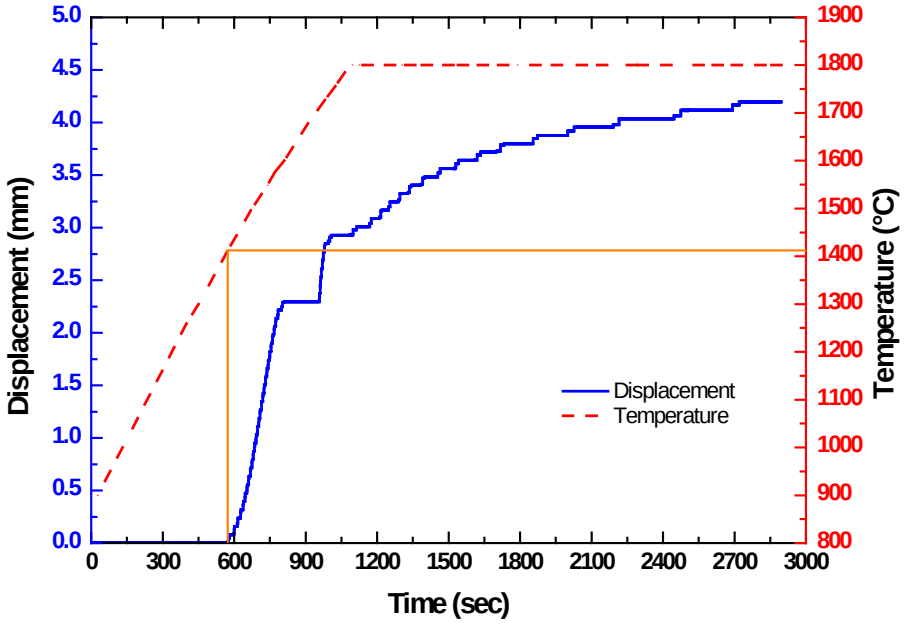

Figure 4.7 Temperature and Shrinkage Vs Time for D material

E material (100% B_4C) required temperature of 1930 °C (the maximum allowed in our machine) with 20 minutes of dwell time and F material (100% TiB_2) was sintered at 1750 °C with 10 minutes of dwell time (Fig. 4.8).

High energy milled B_4C, material was more refractory than the other compositions. The onset of densification was moved to higher temperatures, around 1890 °C. B_4C/TiB_2-based materials, densification started at much lower temperatures: 1160-1660 °C. All data on the start of densification process are shown in Table 4.1.

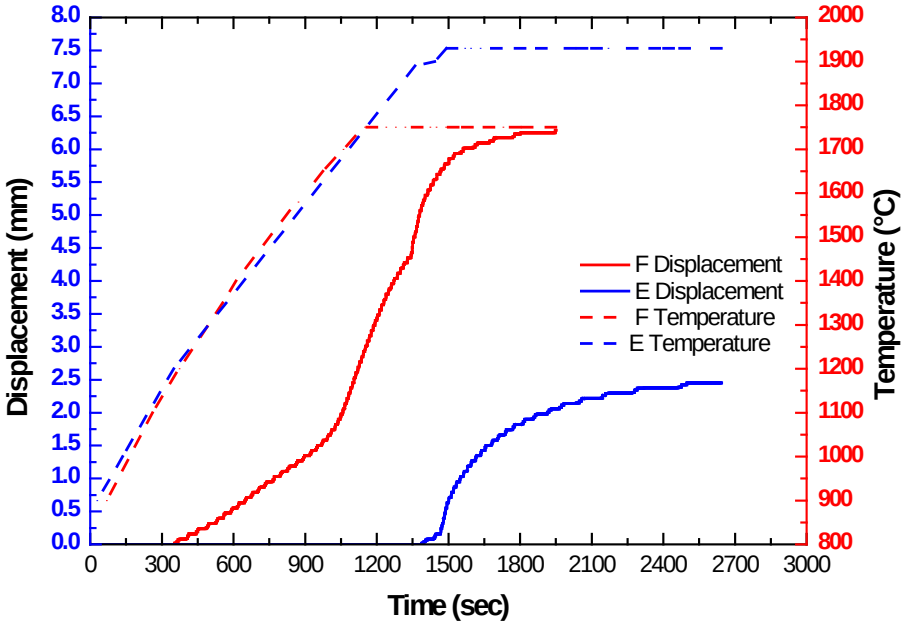

Figure 4.8 Temperature and Shrinkage Vs Time for E and F materials

Table 4.1 For each sample: composition, type of grinding, onset temperature (T_{ON}), theoretical density, final density, relative density

Sample	Composition			Process			Sintered material	
	B_4C/TiB_2 (v%)	Sint. aid (v%)	ρ_{Th} (g/cm^3)	Mixing/ milling	Sintering (°C | min| MPa)	T_{ON} (°C)	ρ_{bulk} (g/cm^3)	$\rho_{\% bulk}$ (%)
A	50/40	10 SiC (n)	3.38	BM	1930|20|30	1630	3.27	96.8
B	50/40	10 SiC(β)	3.38	BM	1930|20|30	1660	3.22	95.3
C	50/45	5 Si_3N_4	3.44	BM	1930|20|30	1660	3.26	94.8
D	55 B_4C	45 TiO_2	3.02	HEBM	1800|30|40	1410	2.37	78
E	100 B_4C	-	2.72	HEBM	1930|20|30	1890	2.38	85
F	100 TiB_2	-	4.71	HEBM	1750|10|30	1160	4.45	94.4

4.1.1.3 Microstructure

A material (n-SiC) – density was 3.27 g/cm^3, which corresponded to a relative density of 96.8%. The BSE image (Fig. 4.9) showed the presence of three phases where SiC (intermediate gray) was easily distinguishable thanks to the channeling contrast that characterizes its microstructural growth. TiB_2 was distinguished as the lightest phase, while the B_4C matrix appeared dark.

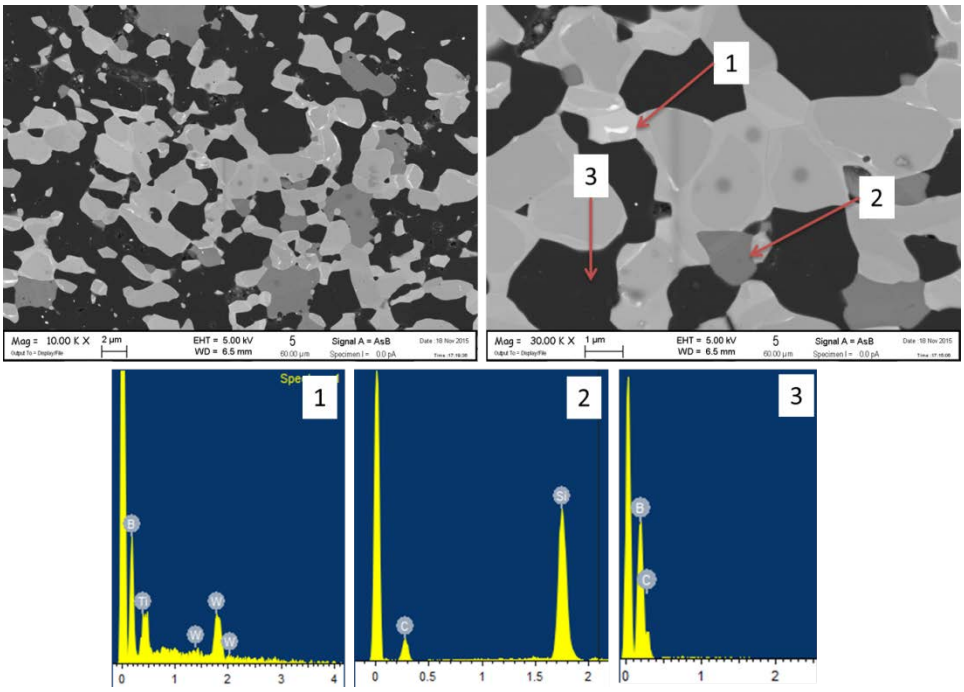

Figure 4.9 FESEM micrographs of A material with related EDS spectra

At low magnifications (Fig. 4.10) the presence of rounded SiC aggregates was found. Probably it is due to the SiC nanometer particles, which were not homogeneously mixed. B_4C had grains around 3-4 µm, TiB_2 around 2-3 µm, while nanometric SiC formed agglomerates sized from 2-5 µm to 30 µm (pointed by red arrows in Fig.4.10).

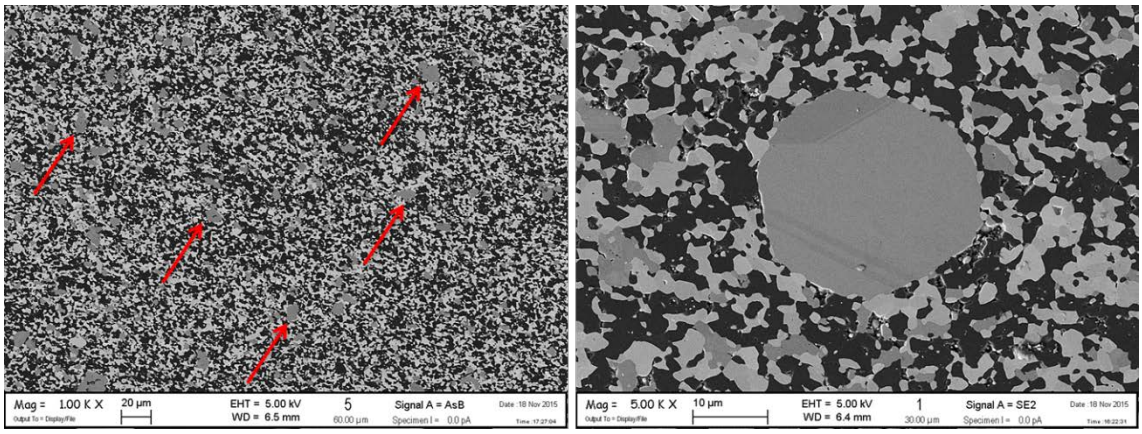

Figure 4.10 FESEM micrographs of A material and detail of a SiC macro defect

B material (β-SiC) - despite B material differs from A material exclusively for the dimensions of the starting SiC, it presented some important differences from a microstructural point of view. The density was 3.22 g/cm^3, equal to 95% of relative density. Despite the residual porosity was slightly higher than A material, this

composite did not show SiC agglomerates (Fig. 4.11). B_4C had a grain size from 2.5 to 10 µm, TiB_2 around 2.55 µm, and SiC around 1.40 µm.

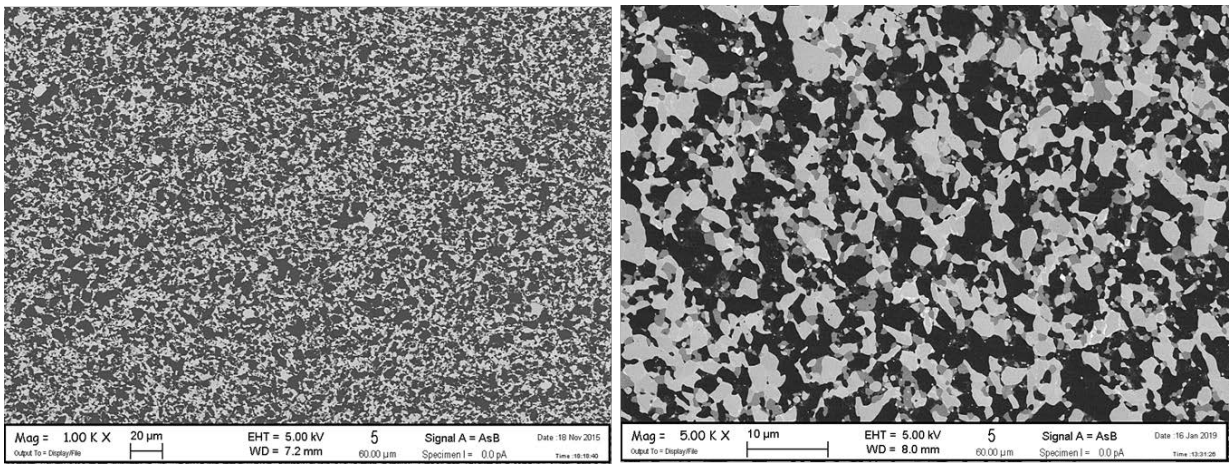

Figure 4.11 FESEM micrographs of B material

C material (Si_3N_4) – the material had density of 3.26 g/cm^3, which corresponded to a relative density of 94.8%. Compared to SiC, this additive was less effective during sintering. Owing to the lower relative density, the polishing had clearly "torn" the grains from the material (left image in Fig. 4.12). However internal porosities were distinguishable by their rounded shape (red arrows in Fig. 4.12). B_4C had grains with an average size of 2.10 µm, and TiB_2 grains had an average size of 2.20 µm.

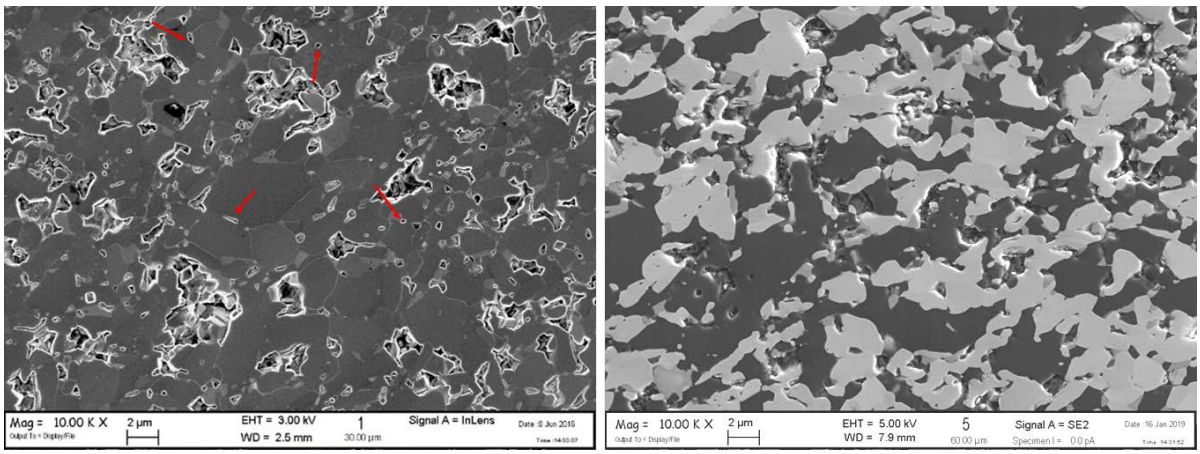

Figure 4.12 FESEM micrographs of C material

The addition of Si_3N_4 had produced a secondary phase in the grain boundaries of TiB_2 and B_4C. EDS spectrum (Fig. 4.13) suggested that Si_3N_4 had partially transformed into SiC by reacting with the free Carbon present in the B_4C.

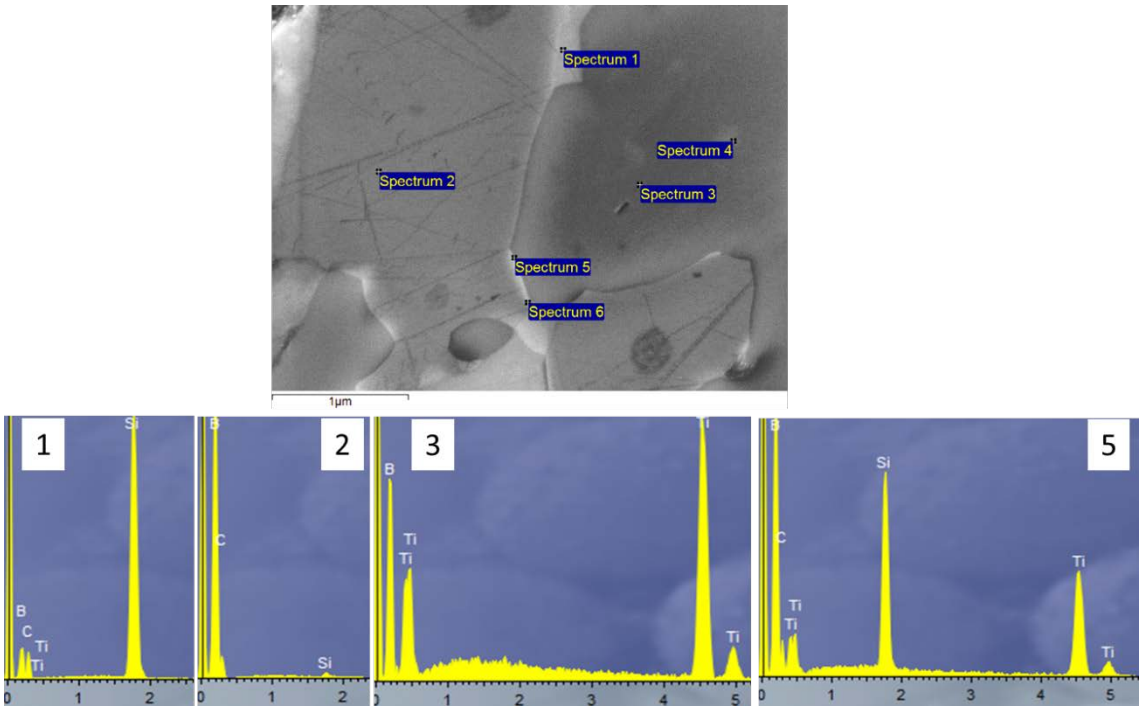

Figure 4.13 FESEM micrographs and EDS spectra of C material showing both the primary phases, B_4C, TiB_2 and the phases formed by the Si_3N_4 reaction.

D material (TiO_2) - The material had density of 2.37 g/cm^3, which corresponded to a relative density of 78%. The high porosity (visible in Fig. 4.14) suggested that more suitable sintering conditions were necessary to obtain a more compact material. B_4C and TiB_2 had grains with an average size of 1.5 µm. The B_4C and TiO_2 mixture appeared to have completely reacted obtaining a solid solution of (Ti_x, W_{1-x}) B (light phase in Fig. 4.14). Tungsten arrived from the contamination of WC grinding bodies. From the EDS analysis (Fig. 4.14) it was noticed the presence of cobalt. Also Co contamination arrived from the WC spheres which contain 6 v%.

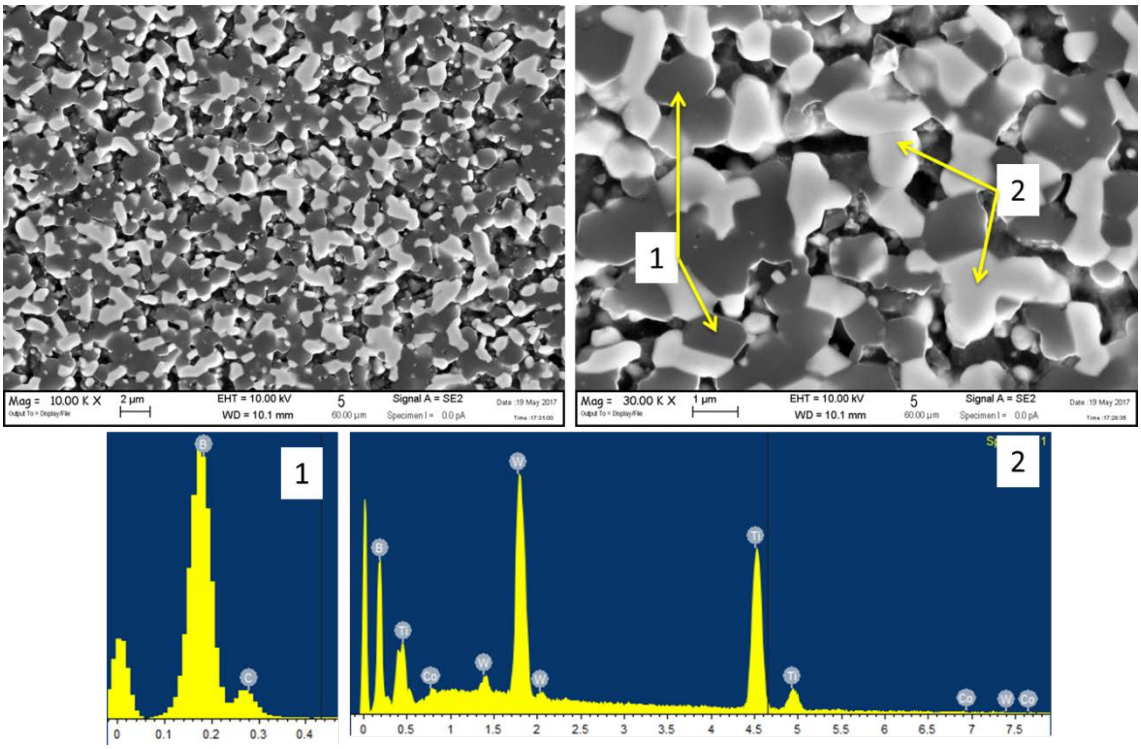

Figure 4.14 FESEM micrographs and EDS spectra of D material

E and F material (B_4C HEBM, TiB_2 HEBM) - Observing the microstructures of the polishing cross sections of the pure E (100% B_4C) and F (100% TiB_2) materials (Fig. 4.15) it was noted that the sintering temperatures had not been sufficiently high to obtain more than 95% of relative density. In this case the reduction of particle size, and the contamination by WC did not help the consolidation of the materials.

E material - The material had a density of 2.38 g/cm^3, which corresponded to a relative density of 85%. 15 v% of porosity remained, although the reduced starting particle size, the contamination of WC, and the temperature limit value of 1930 °C was reached (limit of our facilities). The poor densification should be ascribed to the low diffusion coefficient of B_4C. The average grain size calculated by image analysis on FESEM micrographs was approximately 0.75 µm. This value was comparable with the average size of the starting commercial powders and indicated that HEBM process balances the grain growth due to high temperature sintering. No (Ti,W)B_2 solid solutions were present. X-ray diffraction (Fig. 4.16) confirmed the formation of the new phase, W_2B_5, obtained by reaction between B_4C and WC. Traces of TiB_2 have also been found which probably derive from a small contamination of the sieves.

F material - the material had a density of 4.45 g/cm^3, which corresponded to relative density of 94.4%. The low temperature leaved a residual porosity of 5.6 v% and grain

boundaries not very cohesive in some areas. The mean grain size calculated by image analysis on FESEM micrographs (Fig. 4.15) was approximately 0.97 μm. This value was much lower than the mean particle size of the starting commercial powder (2.58 μm) and suggests that the high energy milling process (HEBM) was particularly effective in reducing the particles powder size. The microstructure was characterized by the presence of high-contrast phases homogeneously distributed. EDS and X-ray analysis in Fig. 4.17 revealed that these phases were WB and W_2C. TiB_2 grains had a peculiar microstructure called rim-core, where the core was pure TiB_2, and the rim was a solid solution $(Ti,W)B_2$. This typical structure was achieved by process of dissolution and precipitation of the grains in the presence of a liquid phase during sintering. Under these conditions the crystal structure of TiB_2 could host W atoms, but the low sintering temperature (1750 °C) did not complete the entire diffusion of the W in the main phase.

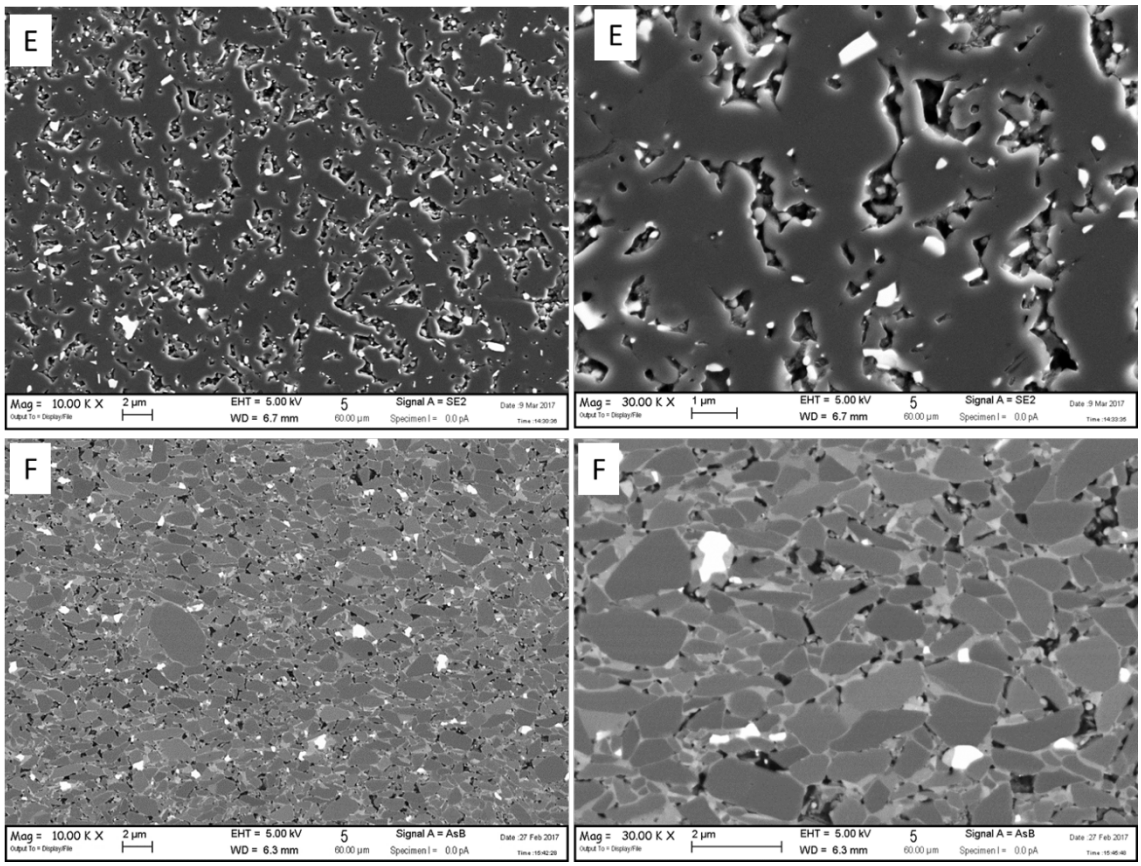

Figure 4.15 FESEM micrographs of E and F materials

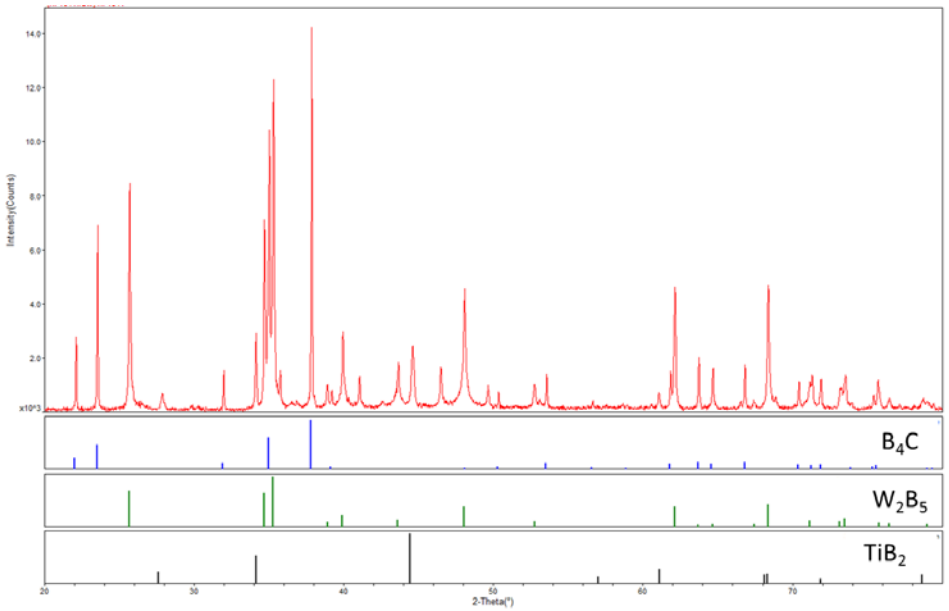

Figure 4.16 X-ray diffraction patterns E material

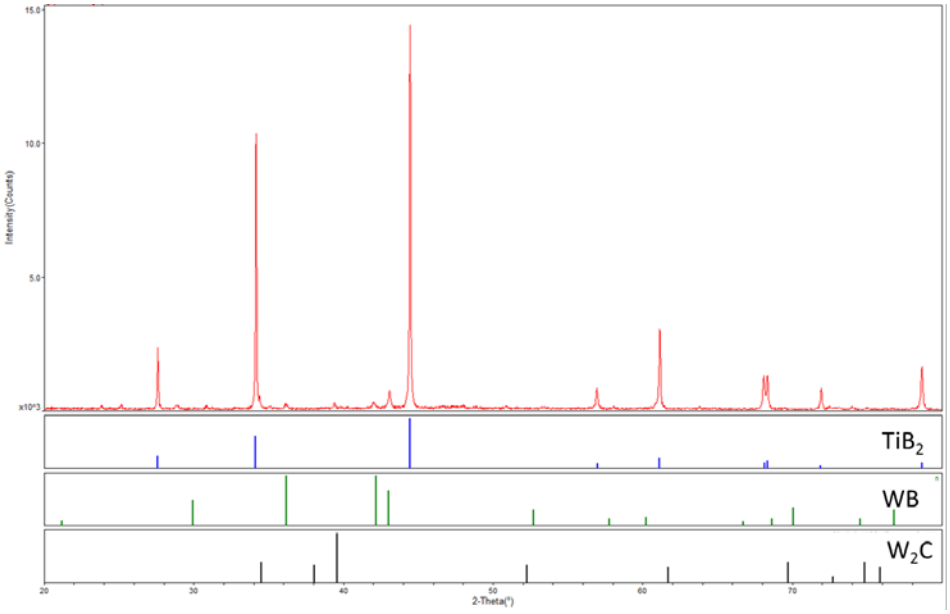

Figure 4.17 X-ray diffraction patterns F material

4.1.1.4 Mechanical properties

Table 4.2 shows the values of the mechanical properties: hardness, flexural strength, fracture toughness and elastic modulus.

In the first instance, the hardness value of all samples was measured to assess the quality of the individual materials. For D material, it was not possible to perform this test since the high degree of porosity did not allow for regular indentations useful to

extract values of Vickers footprint diagonals. The only material that gave values in line with its composition was A material with a hardness value of 28 GPa. B material, despite slightly differed from A material for the absence of abnormal SiC aggregates and a slightly greater porosity, had a much lower hardness value, 18 GPa. Its microstructural homogeneity could not compensate for the greater cohesion of the grains obtained in A material. C material, in which Si_3N_4 was present as a sintering additive, obtained a lower hardness value, 23 GPa, than expected one obtained by rule of mixture, about 28 GPa. The reason for this value mismatch was mainly attributed to the residual porosity. In accordance with the porosity values and the microstructural analysis analyzed in section 4.1.2.3, E and F materials had very low values compared to the theoretical ones, which are respectively 35 GPa[2] and 25 GPa[3]. On the basis of microstructural analyzes and micro-hardness values, only the mechanical properties of A material was further investigated. This material shown values of Young's modulus and fracture toughness close to the expected ones. The high value of strength (592 ± 59 MPa) could be raised by further improving the densification and by avoiding the abnormal agglomerates of SiC.

Table 4.2 Mechanical properties of materials produced by HP: hardness, flexural strength, fracture toughness, Young's modulus, relative density. Some materials were not completely characterized due to their high porosity.

Sample	Sintering aid (v%)	Relative density (%)	Hardness (GPa)	Strength (MPa)	Fracture toughness (MPa· $m^{0.5}$)	Young modulus (GPa)
A	10 SiC (n)	96.8	28 ± 0.3	592 ± 59	4.32 ± 0.14	440
B	10 SiC(β)	95.3	18.7 ± 1.4	-	-	-
C	5 Si_3N_4	94.8	23.4 ± 1.3	-	-	-
D	45 TiO_2	78	-	-	-	-
E	HEBM B_4C	94	12.2 ± 0.6	-	-	-
F	HEBM TiB_2	94.4	18 ± 0.3	-	-	-

4.1.2 Effect of WC content on sintering and microstructure

4.1.2.1 Sintering behavior

All the mixtures were sintered by HP at 1750-1930 °C. Densification behaviour of B50-1, B50-2, B50-3 is reported in Fig. 4.18 as relative density and temperature curves vs time. We can note that densification started at 1660 °C for B50-1 (soft ball milling), 1400 °C for B50-2 (addition of WC particles) and 1320 °C for B50-3 (high energy

milling). Beside this, for all three systems after a short stage of solid state sintering accompanied by little shrinkage, a steep increase of the densification rate occurred, as typical of particle rearrangement in presence of a *liquidus*. From the change in the curve slope it can be approximately inferred that 1800°C was the temperature for liquid phase formation of B50-1, 1500 °C for both B50-2 and B50-3. It can be also visualized that B50-3 had the highest shrinkage rate after an initial slow stage. The baseline composition, B50-1, reached about 93% of relative density upon densification by hot pressing at 1930°C. With the addition of 5% WC (B50-2), the final relative density increased to 96 %. The high energy milling of the powders (B50-3), resulted in a notable improvement of the densification behavior, with the shrinkage completed at 1860°C and the final relative density reaching 98 %. Fig. 4.18b compares B50-3 with B25-3 and B75-3, e.g. systems containing different amounts of B_4C processed with the high energy milling. In this case, increasing the amount of B_4C, B75-3, the system becomes more refractory. The onset of densification is shifted to higher temperature, roughly 1490 °C. In contrast, increasing the TiB_2 content, B25-3, the densification started at much lower temperature, e.g. 1160 °C. All densification data are reported in Table 4.3.

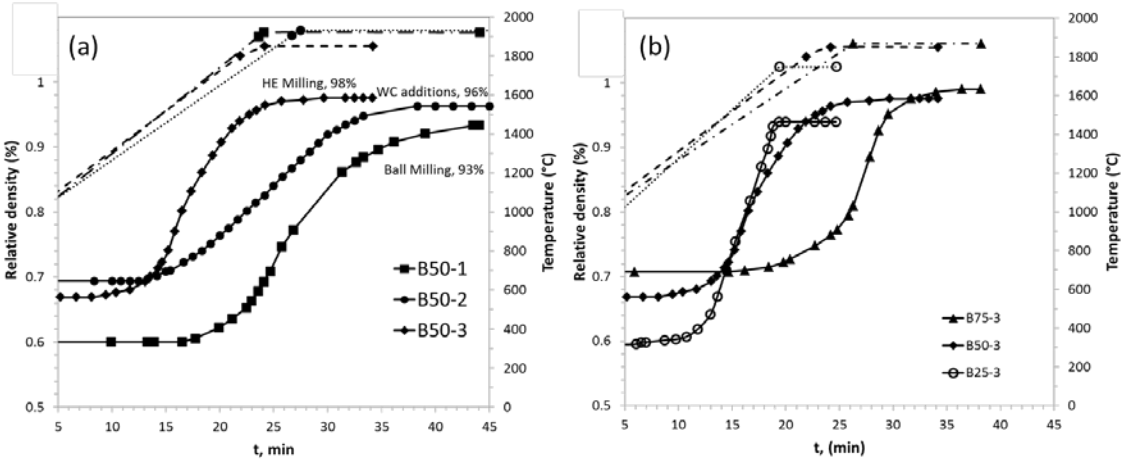

Figure 4.18 a) Comparison of densification curves for 50/50 systems with different process, B50-1, B50-2, B50-3. b) comparison of densification curves for different B_4C content according to process 3, B25-3, B50-3, B75-3.

Table 4.3 Starting compositions (including WC), processes, sintering parameters and densities

Sample	Mixing/ milling	Composition		Sintering				Sintered material	
		Starting powders	Incorporated WC	ρ_{Th}	T_{ON}	Slope change	$T_{Max.}$	ρ_{bulk}	$\rho_{\% bulk}$
		v %	v %	g/cm^3	°C	°C	°C	g/cm^3	%
B50-1	BM	$50B_4C+50TiB_2$	Traces	3.52	1660	1800	1920	3.28	93.0
B50-2	BM	$50B_4C+45TiB_2+5WC$	Traces	4.08	1400	1500	1930	3.91	96.0
B50-3	HEBM	$50B_4C + 50TiB_2$	~1.5	3.70	1320	1500	1860	3.60	98.0
B75-3	HEBM	$75B_4C + 25TiB_2$	~1.6	3.21	1490	1850	1870	3.18	99.0
B25-3	HEBM	$25B_4C + 75TiB_2$	~2.1	4.25	1160	1400	1750	4.02	94.5

4.1.2.2 Microstructural analysis

Fig. 4.19 shows batches B50-1 and B50-3 powder mixtures, ball milled and high energy milled, corresponding EDS spectra and sedimentation analysis. B50-2 was not reported since the direct addition of WC powder masked the effect of contamination due to milling. As expected, only after high energy milling significant incorporation of WC was measured, ~1.5 v% (Table 4.3). Comparing SEM-EDS analysis of B50-1 and B50-3, (Fig. 4.19) decrease of mean particle size and increase of W and Co contamination after high-energy milling compared to the ball milled system was observed. Some W contamination was detected by EDS also in the ball milled powder, not traceable by simple weight difference measures. However, comparing the EDS spectra collected in the same conditions from the two powders, we inferred that the W contamination is one order of magnitude lower than after high energy milling, e.g. ~0.1 v%. Accordingly, the sedimentation analysis showed a significant decrease of the starting particle size, Fig. 4.19c as compared to the ball milled system. It must be mentioned that the analysis was carried out on the TiB_2 – B_4C mixtures, thus it is not possible to discern between the two constituent particle sizes. Nevertheless, it was evident in Fig. 4.19c that the coarse fraction of the mixture was significantly reduced, indeed D90 changed from the nominal 4-7 μm of starting TiB_2 (the coarsest) to 4.3 μm in the planetary milled mixture (B50-3). The same high energy milling procedure applied for B75-3 and B25-3 led to decrease of mean particle size (not shown) and WC contamination. The difference in weight indicates that the amount of incorporated WC was around 1.6 and 2.1 v%, respectively, see Table 4.3.

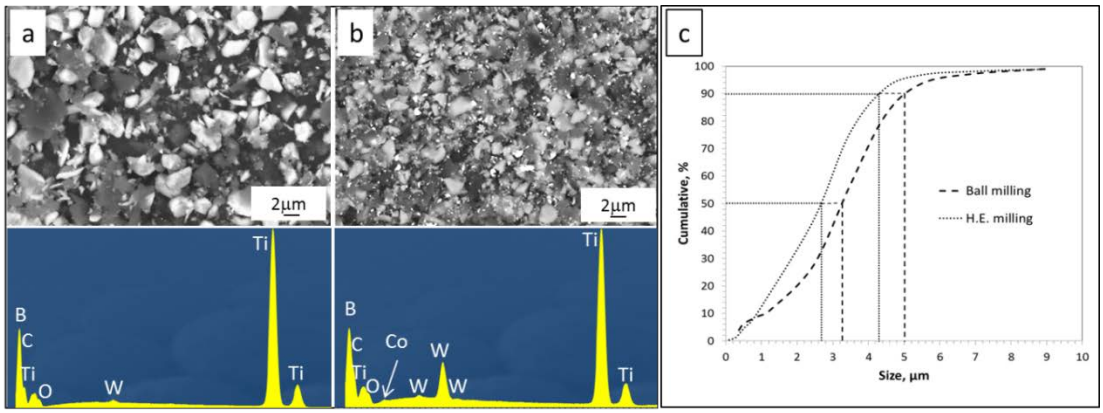

Figure 4.19 a) B50-1 after ball milling and corresponding EDS spectrum b) B50-3 after high energy milling and corresponding EDS spectrum, c) Graph of particle size distribution for composition B50-1, and B50-3

Microstructural features of 50/50 systems (B50 materials): X-ray diffraction patterns, in Fig. 4.20, were collected on dense samples to analyse possible formation of W-based phases. Neither WC-based phases nor other types of W-based phases were detected in the microstructure. TiB_2 and B_4C are mainly stoichiometric (TiB_2: JCPDF card 35-0741, B_4C: JCPDF card 35-0798).

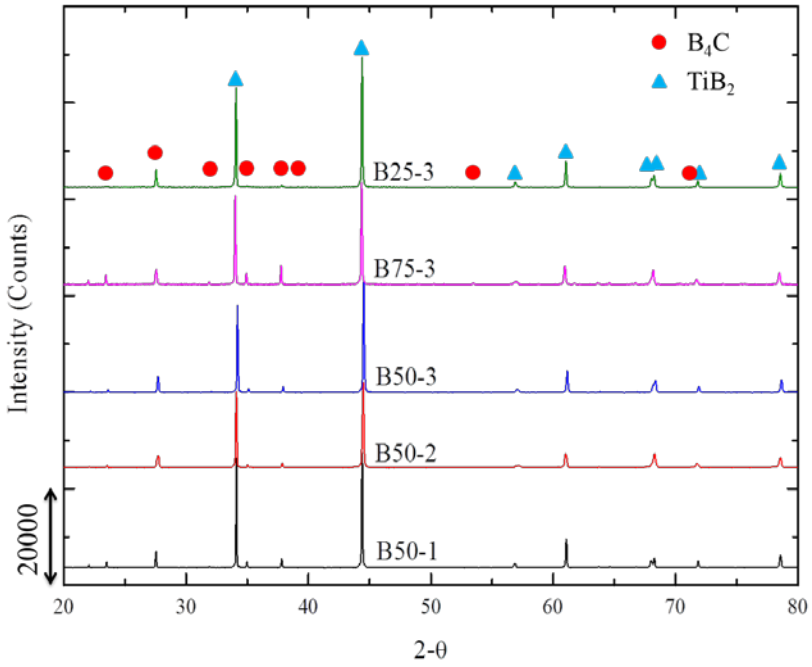

Figure 4.20 Post sintering X-ray diffraction patterns of the 5 systems investigated: only principal phases (B_4C, TiB_2) were detected.

Micrographs of fractures (in lens imaging) and polished sections (BSE imaging) are shown in Fig. 4.21 a–f.

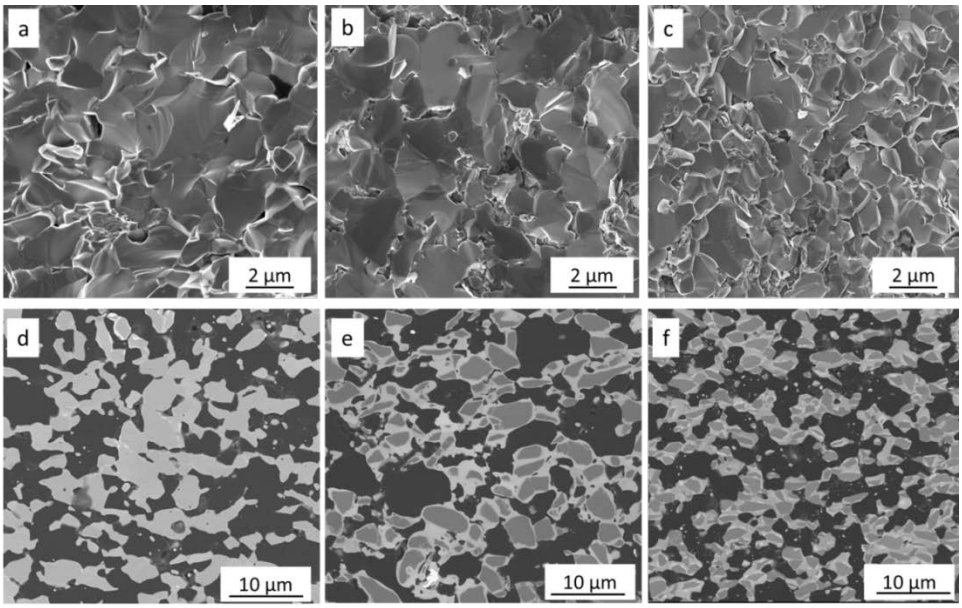

Figure 4.21 SEM images of the fracture and polished surfaces of B_4C-TiB_2-based composites obtained by different processes. a-d) soft ball milling with WC media, B50-1 b-e) addition of 5 v% WC, B50-2 and c-f) high energy milling, B50-3.

Notably, a very low level of porosity is observed in all the samples, although grain pull-out is frequently found. Pull-out is caused by CTE mismatch between B_4C and TiB_2, as reported in literature [4]. The polished sections revealed interesting features: B_4C exhibited rounded grains with dark contrast in BSE imaging, while TiB_2 was characterized by bright contrast. Carbon pockets, recognizable as dark contrasting phases, were often found at the boundary between B_4C and TiB_2 grains, or B_4C/B_4C interfaces. Other thin dark contrasting phases can be observed at B_4C/B_4C or C/B_4C interfaces and their composition has to be determined by future TEM studies. As previously mentioned, milling with WC even at mild conditions causes contamination of the starting powders, see Fig. 4.19a. This is however, particularly evident for high energy milling process (Fig. 4.19b). Incorporation of WC as secondary phase or though milling causes the formation of core shell structures in TiB_2 grains, where the core is the original TiB_2 cores, and the shell is constituted by a $(Ti_x,W_{1-x})B_2$ solid solution. Notably, no alteration of the x-ray diffraction pattern (peak shift or splitting) was observed, probably due to similar atomic radius displayed by Ti and W [5]. Another interesting feature is the particles size reduction occurring upon high energy milling.

Indeed, it can be seen that in B50-3 sample, the mean grain size of TiB_2 and B_4C is almost halved compared to B50-1 and B50-2 (Fig. 4.21). At higher magnification we can observe other interesting features in these materials: for sample B50-3, a double solid solution was indeed observed, Fig. 4.22a, with higher W content in the inner shell, compared to the outer one, see Fig. 4.22b and c.

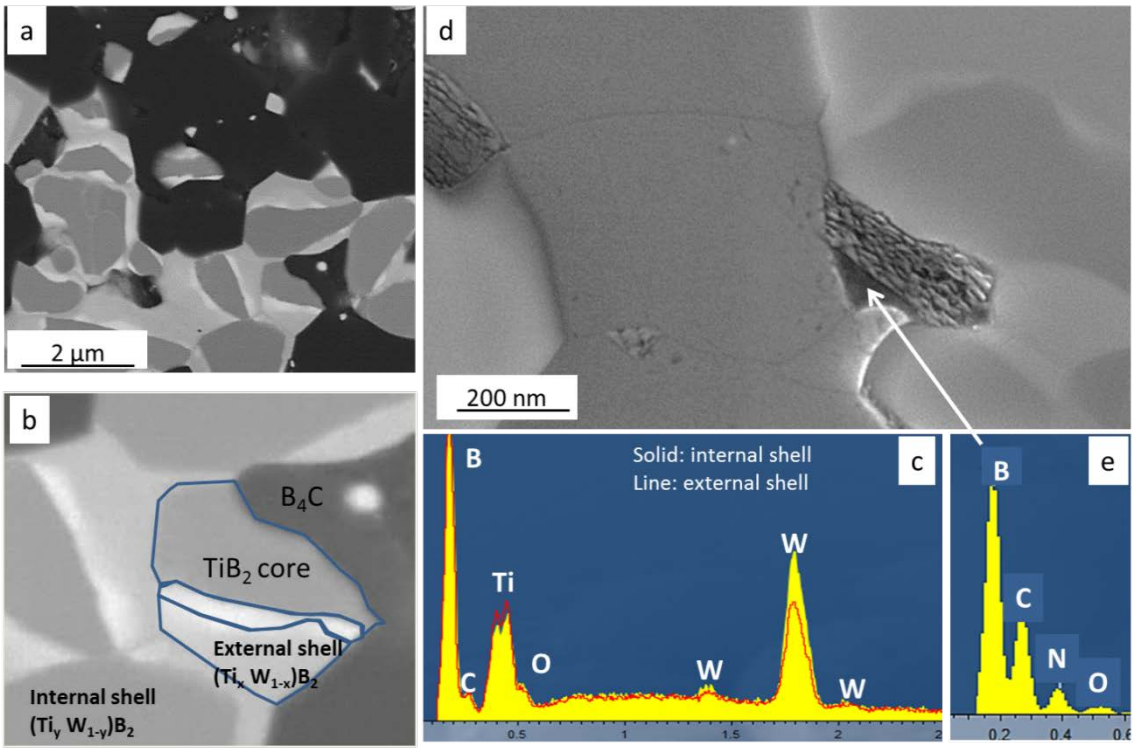

Figure 4.22 Microstructural details of B50-3 sample. a) overview in BSE imaging, b) magnified BSE image with a sketch of the double $(Ti_x,W_{1-x})B_2$ solid solution, c) related EDS spectra showing different amount of W in the internal and external shell, d) In-lens image of the microstructure displaying BN pockets and low density phases, e) EDS spectrum of a residual B-C-N-O phase, in the vicinity of BN lamellae.

Fig. 4.22d shows residual BN based pockets usually located at the B_4C/B_4C and B_4C/TiB_2 boundaries, with low density phases in the vicinity, containing B, N, O, C, Fig. 4.22d. BN formation in the present materials is probably due to the reaction of nitrogen dissolved in the starting powders according to [6]. Another possible source of N is nitrogen present in the vacuum atmosphere during hot pressing, as suggested in [7].

Microstructural features of planetary milled systems with 25 and 75 vol % of B_4C:

The microstructures of polished surfaces of B25-3 and B75- 3 samples are shown in Fig. 4.23 a, b. According to X-ray diffraction (see Fig. 4.20) only the primary

constituent phases were detected, in analogy with the previous presented materials. It can be noted that B25-3 has a finer microstructure compared to B75-3 mainly due to the lower sintering temperature (1750 vs 1870 °C). Details of mean grain size are reported in Table 4.4. As for the previous analyzed systems we observed residual BN or C pockets, core shell structures in TiB_2 grains and double solid solutions in both systems.

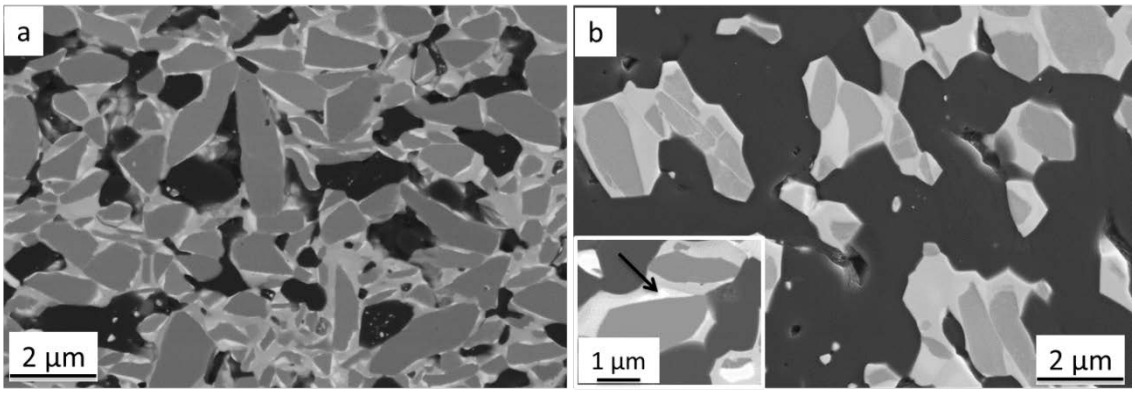

Figure 4.23 Overview of B25-3 samples (a), with a TiB_2 content of 75% and B75-3(b) with a B_4C content of 75%. Note the reduction in mean grain size for the former and the double core-shell structure in both cases (inset in Fig. 4.23b: arrow points to a W-rich shell onto a TiB_2 core).

Densification mechanism

Low self-diffusion coefficients of both constituent phases and surface oxides present on the particle surface are considered responsible for the poor sinterability of the system. Although there is plenty of literature on this system, there is still debate on the densification mechanism occurring for B_4C-TiB_2 systems and the similar B_4C-ZrB_2 or B_4C-HfB_2 systems. The role of B_2O_3 is still controversial, most of the works recognize that B_2O_3 contributes mainly to coarsening rather than densification of B_4C-based materials. A few publications state that the presence of liquid B_2O_3 could instead help the densification of these composites [8]. In our systems, clues that can help in understanding the basic sintering mechanisms are the following:

- WC is reported to be a sintering aid for borides [9];
- Metallic impurities (such as Co introduced with WC milling) are known to favour B_4C densification [10];
- B_2O_3 is liquid above 1200 °C and it is difficult to remove it by vaporization during hot pressing because the powder is constrained between the rams;

- A rapid increase of the shrinkage rate occurs at temperatures well below those reported in the literature;
- TiB_2 grains undergo a notable transformation incorporating W and C and forming core shell structures;
- B-N-C-O based phases and other low density phases are found at the B_4C/B_4C interfaces.

All these clues suggest that densification could be aided by a liquid phase sintering mechanism. We suggest a possible pathway in the sketch of Fig. 4.24. According to this pathway, liquid B_2O_3 could be the base for liquid phase formation. A B-O -liquid medium containing W and metallic impurities could help the initial stage of rearrangement which explains the rapid increase of the densification rate [11] occurring at temperature between 1400 and 1800 °C for all systems.

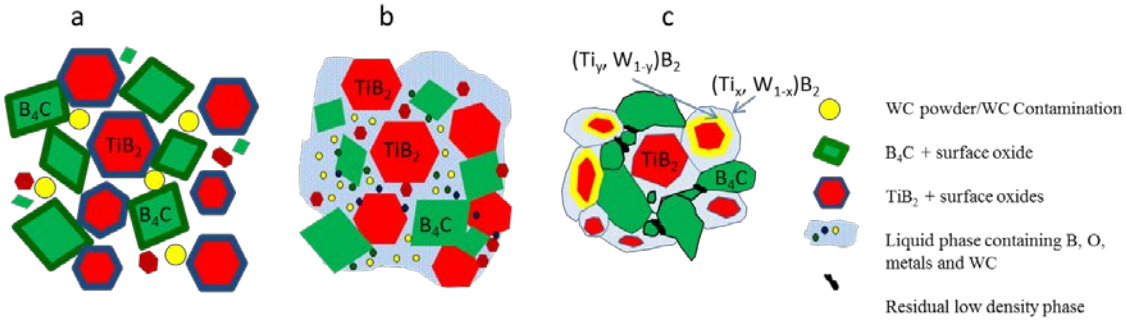

Figure 4.24 a)–c) Sketch of the possible mechanisms occurring during densification, a) starting stage, with all the powders and their respective oxides, b) formation of liquid phase, c) dissolution of TiB_2 grains and precipitation of multiple $(Ti,W)B_2$ shells.

At higher temperatures, almost close to the beginning of the isothermal stage, smaller TiB_2 grains dissolve in the liquid phase and reprecipitate onto larger TiB_2 grains, collecting W and C. This causes the formation of core-shell structures. B_4C grains are not substantially involved in dissolution reprecipitation, however, the liquid phase has the ability to clean the surface from residual oxides, permitting a solid state densification. During cooling from the sintering temperature locally unbalanced amounts of B-C-N-O species can give rise to newly formed B_4C, residual C, BN, BCN or glassy phases. We also expect to observe thin amorphous intergranular phases by TEM in future studies. The occurrence of double solid solutions, with a W-richer inner

layer compared to the outer rim is still under investigation. This phenomenon was observed mainly in B50-3, B75-3 and B25-3. In B50-1 and 2 instead, the shells seem to have a homogeneous color, e.g. composition. This finding suggests that the formation of double solid solutions is somewhat related to the high energy milling procedure and/or to the lower sintering temperature. The formation of double rims is well known in Ti (C,N) cermets prepared by ball milling with WC-Co media [12] and was attributed to dissolution and precipitation process during liquid phase sintering. According to the authors, the inner rim, that is richer in W compared to the outer rim, was formed during the heating stage from the onset temperature for liquid formation, whilst the outer rim was formed at the sintering temperature. This could also be the case for the present materials: early precipitation of W-rich (Ti, W)B_2 layers at temperatures between the onset of liquid phase formation and 1800 °C and then re-precipitation of outer rims with a lower W concentration during the completion of sintering. For thermal treatments at T > 1900 °C (B50-1 and B50-2) the higher temperature could have favored the homogenization of the shell composition. Similar findings were observed in HfB_2-based materials produced by spark plasma sintering, where the mild sintering temperatures (in the range 1300–1700 °C) and fast densification impeded homogenization of double solid solutions [13].

4.1.2.3 Mechanical properties

Mechanical properties are reported in Table 4.4. Values of Vickers hardness span from 18 for B25-3 to 32 GPa for B75-3. In first approximation, the hardness of a composite can be estimated by the rule of mixtures [14]. Using 25 GPa and 35 GPa, as reference values for TiB_2 [3] and B_4C [2] respectively and neglecting the contribution of WC, we obtain the following predicted values: 30 GPa for 50/50, 32.3 GPa for 75 B_4C/ 25 TiB_2, 27.5 GPa for 25 B_4C/ 75 TiB_2. Hardness values of B50-1 and B50-2 samples are lower than predicted values due to residual porosity as well as residual phases, such as C pockets or BN pockets. In contrast, B50-3 (28.5 ± 1.38 GPa) and B75-3 (32 GPa) HV values are in good agreement with the value predicted by the rule of mixture, showing an increase of hardness with increasing the B_4C content. The TiB_2-rich composite, B25-3 has a remarkably low hardness due to residual porosity.

Table 4.4 Mechanical properties of dense samples, Legend: m.g.s.: mean grain size, HV1.0: Vickers Hardness, RH: relative hardness, σ: 4-pt flexural strength, E: Young's modulus, K_{IC}: fracture toughness.

Sample	Microstructure		HV1.0		σ			E	K_{Ic}
	m.g.s.	$\rho_{\%}$	exp	RH	RT	1200°C	$\sigma_{1200}/\sigma_{RT}$	RT	RT
	μm	%	GPa	%	MPa	MPa	-	GPa	MPa·m$^{0.5}$
B50-1	B_4C~1.69 TiB_2~2.33	93	24.0 ± 0.6	80	630±75	646±27	>1	460	4.20±0.03
B50-2	B_4C~1.70 TiB_2~1.65	96	24.5 ± 0.3	82	520±90	470±35	0.90	406	4.5±0.1
B50-3	B_4C~0.89 TiB_2~1.00	98	28.5 ± 1.4	95	860±40	524±44	0.61	407	4.5±0.1
B75-3	B_4C~1.14 TiB_2~0.9	99	32.2± 1.8	100	815±74	451±37	0.55	451	3.4±0.1
B25-3	B_4C~0.53 TiB_2~1.00	95	18.0 ± 0.5	65	745±81	487±69	0.65	398	5.1±0.1

The Young's modulus is affected by both composition and residual porosity of the samples. Within the 50/50 compositions (B50-1,2, and 3) the addition of WC either as a powder or through the milling procedure seems to strongly penalize this property. The highest value is indeed found for the ball milled system where the WC contamination is lower. Looking at the B25, 50, 75-3 composites, one expects an increase of stiffness with increasing the TiB_2 content, due to the higher stiffness of the boride. On the contrary, B25-3 has the lowest E value (residual porosity < 2%) and B75-3 the highest one (residual porosity>5%). These unexpectedly low values suggest that beside residual porosity, spurious C, BN pockets and B-O phases could be also detrimental for E and indicate that the milling procedure must be carefully tailored, in order to avoid an excessive C and O contamination. The fracture toughness was nearly constant amongst samples with 50/50 composition. This value is generally higher than what reported for monolithic B_4C (~2 MPa·m$^{0.5}$), due to the addition of TiB_2. TiB_2 is known to improve the fracture toughness mainly through the residual stress toughening mechanism [15], and crack deflection, as previously indicated. As a matter of fact, the crack propagates mainly transgranularly for B_4C, and intergranularly for TiB_2. Decreasing the amount of TiB_2, as in B75-3, we indeed observed a decrease of the toughness, due to lower degree of crack deflection and lower residual stresses. On the contrary, increasing the amount of TiB_2 leads to an increase of toughness to 5 MPa·m$^{0.5}$. Actually, considering B75, 50, 25-3 there is a nearly linear increase of toughness with increasing the TiB_2 content. The flexural strength was influenced by the mean grain size of the samples. The finer microstructures obtained with high energy milling for B50-3 and B75-3 improved this

property up to 860 MPa and 815 MPa, with peak values of 900 MPa for the former. As for the strength at 1200 °C, the tests were conducted in Ar, in order to limit oxidation effects. Despite a slight darkening of the samples indicating some surficial oxidation, the values found give indication of the high temperature stability of bulk (main and secondary) phases. The system with the lowest addition of WC, e.g. B50-1, was the most refractory, indeed the strength at 1200 °C is the same as the RT one. In B50-2, the addition of WC as a powder, led to a decrease of strength of about 10%. For systems that underwent high energy milling, the 1200 °C strength is sensibly lower than the RT value. Softening of oxygen bearing residual phases deriving from the liquid formed during sintering, as those identified in Fig. 4.22d, seem to be the most probable cause of this sudden decrease. It can be also noticed that increasing the amount of TiB_2 we obtain a higher stability of the systems, as expected. Indeed, the 1200 °C strength retains 55, 60, 65% of the RT value, for 25, 50, 75 volumetric content of TiB_2, respectively.

4.1.3 Conclusions

Particle size, X-ray diffraction and scanning electron microscope observations of commercial B_4C and TiB_2 powders were performed.

The X-ray diffraction on powders allowed us to conclude that commercial B_4C and TiB_2 are stoichiometric and there are no secondary phases in the starting powders.

The mixtures containing 50v% B_4C, with 40-45 v% TiB_2 and various sintering additives (10 v% SiC, 5 v% Si_3N_4) were prepared.

The powders were pressed linearly to obtain billets and the sintering tests were carried out by hot pressing (HP). In the presence of the sintering additive, the material which had the most satisfactory results in terms of relative density was the one with SiC. A sintering reaction test was carried out with TiO_2, to facilitate the densification process, in order to obtain a final composition 75v% B_4C - 25v% TiB_2. In this way the start densification temperature was decreased due to the reduced particles size and the development of the sintering reaction. However, the thermal cycle must be optimized to obtain a satisfactory degree of densification.

100% B_4C and 100% TiB_2 were sintered as base materials obtained by high-energy milling with WC-based grinding media. Despite that, it was evident that the pure B_4C

material requires temperatures > 1950 °C to obtain a full densification. In contrast, for TiB_2 material, densification starts at much lower temperatures.

The microstructural characterization of the materials produced allowed us to identify the main characteristics and problems of the sintering of these materials. Commercial SiC has proven to be a valid additive, generating a homogeneous microstructure without macro-defects. However, the process must be revised to achieve an increase density up to 99%. A good solution is to use a high energy grinding stage to obtain a reduction in grain size.

Nano-SiC has limited the growth of B_4C, but has formed numerous aggregates dispersed in the matrix and difficult to eliminate. Si_3N_4 tends to react on the grain boundary forming SiC, but even in this case the level of densification does not appear sufficient for the application. The identification of the residual porosity of the material is difficult to quantify through image analysis due to the grain pull out due to polishing.

The reaction of B_4C with TiO_2, in D sample, did not produce TiB_2 grains but rather a solid solution with W and Co coming from WC grinding media. The material has not very cohesive grains with each other and high porosity. Further analysis on the thermal cycle may lead to an improvement in the densification of the material, for example by increasing the sintering temperature from 1800 °C to 1900 °C. For E sample (100% B_4C) the sintering temperature (1930 °C in HP) is not high enough to achieve satisfactory densification, despite the reduction in grain size. Therefore it is necessary to apply temperatures higher than 1950 °C. For the TiB_2, sintered in HP, there is still a margin of improvement since the sintering temperature has been limited to 1750 °C.

B_4C-TiB_2 composites were deliberately contaminated with WC in order to improve the densification and properties using different procedures. High energy milling was very effective in reducing the size of the starting powders (from 1.7 to 1 μm) with consequent improvement in densification but stimulated the formation of low density spurious phases (such as BN, C, and B-O based phases). In the materials with sintering additives, nano-SiC was considered the most suitable having hardness values in agreement with the theoretical values of its composition (28 GPa). Strength and hardness benefited from a reduction in mean grain size, while the Young's modulus and the high temperature strength were penalized by the presence of soft phases. The fracture toughness was insensitive to the milling procedure but increased with increasing the TiB_2 content. The best compromise in terms of properties, for the system B_4C-TiB_2 without additives, was achieved with the high energy milled composition

containing 75 vol. % B_4C and 25 vol. % TiB_2, with a hardness of 32 GPa, strength of 815 MPa and modulus of 450 GPa. The results obtained show that the final properties of B_4C-TiB_2 composites can be tailored by carefully designing the starting composition and the process.

4.2 B_4C/TiB_2 (Pressureless sintering, Gas pressure sintering)

Mixtures of B_4C-TiB_2 made without sintering additives were consolidated by the pressureless sintering (PLS) and gas pressure sintering (GPS) techniques. The investigated compositions spanned from B_4C rich composition to TiB_2 rich composition. PLS and GPS offer several advantages, because of their ability to prepare near-net-shape components. Over all, when PLS/GPS is applied, subsequent diamond machining of the sintered parts can be limited, reducing the production costs [16–20].

Hence, the aim of this second series of high hardness structural ceramics was to increase the hardness of the final product by lowering the production costs with sintering techniques that did not impose restrictions on the final shape of the product and that did not require the use of mechanical pressure.

For all mixtures, HEBM technique was used according to the protocol explained in chapter 3.5.1.

4.2.1 Sintering behavior

Four mixtures (G, H, I, and L, see Table 4.5) were sintered trough PLS and GPS techniques. B_4C-rich samples (G, H, and I) were sintered at 2000 °C, 2050 °C and 2100 °C. L sample, which contains less B_4C, the temperatures analyzed were 1900 °C, 2000 °C, 2100 °C. Fig. 4.25 shows the thermal cycle profiles adopted for PLS and GPS technique. The adopted sintering conditions for each composition are reported in Table 4.5 Further process details are reported in Chapter 3.5.1.

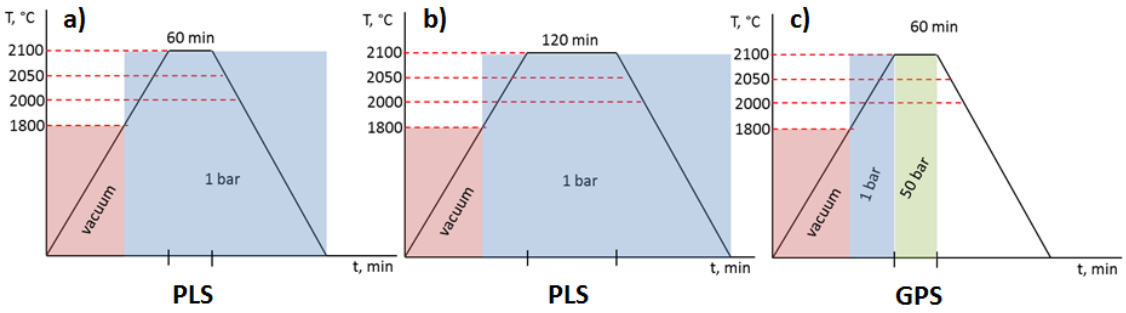

Figure 4.25 Example of sintering cycles of pressureless sintering (PLS) and gas pressure sintering (GPS) with heating ramp of 10 °C/min: a) Tmax, 1 bar, dwell time 1 hour; b) Tmax, 1 bar, dwell time 2 hours; c) Tmax, 50 bar, dwell time 1 hour

G material (100% B_4C) - The relative density of the green body was 65-67 %. Looking at relative density of the materials after PLS process (Table 4.5) and making a comparison between the sintering temperatures and dwell time, it is possible to note, that the relative density values close to 100% were obtained with dwell time of 120 minutes instead of 60 minutes. Nevertheless, for both sintering cycles, the materials reached densities greater than 95%. Comparing PLS with GPS at temperatures of 2050 °C and 2100 °C it was noted that, the gas pressure allowed to achieve the same final density with a shorter dwell time. At 2000 °C the gas pressure contribution was negligible. Even with long dwell time the material had density values equal to or less than 95%. Probably this temperature was not high enough despite the presence of WC contamination, coming from the grinding media. Fig. 5.26 shows the relative density values of G material as function of sintering temperature.

H material (B_4C 87.5/ TiB_2 12.5) - The relative density of the green body was 65-67 %. Observing Table 4.5 it is possible to notice that samples obtained by PLS technique achieved values of relative density ≥ 98% for all temperatures with 120 minutes of dwell time. At 2000 °C, the material struggles to densify for less than 120 minutes of dwell time. Even with the GPS technique, 60 minutes at the maximum temperature were not enough to reach the full densification. Although 12.5 v% TiB_2 is present in a B_4C matrix, this composition still remained highly refractory and required more than 2000 °C to obtain a full densification. At temperatures of 2050 °C and 2100 °C, full densification (relative density of 99%) was obtained with the shortest dwell time of 60 minutes, independently of the used sintering technique. Fig. 4.26 shows the relative density values of H material as function of sintering temperature.

I material (B_4C 75/ TiB_2 25) - The relative density of the green body was 65-67 %. This sample showed a relative density ≥ 97% for 60-120 minutes of dwell time regardless of the sintering process. The highest values were obtained for the samples produced through GPS process for all the investigated temperatures (see Table 4.5). In Fig. 4.26 the relative density values as function of sintering temperature are shown.

L material (B_4C 25/ TiB_2 75) - The relative density of the green body was 60 %. Full densification was obtained at the lowest sintering temperature of 1900 °C. It was found out a density decrease with the increasing of sintering temperature. The most plausible reason could be the formation of gaseous phases which leaved internal porosity. It was something expected since the extended oxide layer existing on the surface of the starting TiB_2 [21–23]

Furthermore, the cycle with the maximum temperature of 2100 °C led to a considerable grains growth, making the material very friable and not very cohesive with a large porosity in the central area. In Fig. 4.26 the relative density values as function of sintering temperature are shown.

Table 4.5 Sintering parameters, densities and hardness of PLS/GPS samples, Legend: m.g.s.: mean grain size, ρ_{bulk}: bulk density, RD: relative density, HV1.0: Vickers Hardness, RH: relative hardness.

Samples	T_{MAX}, (°C)	Sintering	Dwell time, (min)	m. g. s., (μm)	ρ_{bulk}, (g/cm^3)	RD, (%)	HV1.0, (GPa)	RH, (%)
G ρ= 2.72 g/cm^3 B_4C= 100 v%	2000	PLS	120	2.07 ± 0.8	2.60	95.5	16.88 ± 0.82	48
		GPS	60	1.59 ± 0.5	2.58	94.5	15.06 ± 0.55	43
	2050	PLS	120	2.29 ± 0.7	2.69	98.6	24.3 ± 0.78	69
		PLS	60	2.03 ± 0.7	2.63	96.5	22.4 ± 0.67	64
		GPS	60	2.05 ± 0.6	2.72	99.8	24 ± 1.17	68
	2100	PLS	120	204.9 ± 105	3.19	100	26.72 ± 0.87	76
		PLS	60	223.1 ± 65	2.66	97.3	26.3 ± 1.27	75
		GPS	60	139.5 ± 71	2.74	100	26.38 ± 1.46	75
H ρ= 2.99 g/cm^3 B_4C= 87.5 v% TiB_2= 12.5 v%	2000	PLS	120	-	2.94	98.3	21.83 ± 1.3	64
		GPS	60	-	2.84	95.0	16.94 ± 0.91	50
	2050	PLS	120	B_4C~2.31 ± 0.7 TiB_2~2.82 ± 0.8	3.01	100	24.86 ± 0.85	73
		PLS	60	B_4C~1.19 ± 0.5 TiB_2~2.5 ± 0.7	3.00	100	24.73 ± 1.12	73
		GPS	60	B_4C~1.96 ± 0.5 TiB_2~2.5 ± 0.7	2.94	98.7	27.43 ± 0.87	81
	2100	PLS	60	B_4C~33.61 ± 8.8 TiB_2~13.28 ± 4.5	2.96	99.1	26.47 ± 1.63	78
		GPS	60	B_4C~30.66 ± 9.6 TiB_2~15.54 ± 0.4	3.07	100	28.38 ± 0.54	84
I ρ= 3.21 g/cm^3 B_4C= 75 v% TiB_2= 25 v%	2000	PLS	120	B_4C~2.11 ± 0.7 TiB_2~2.29 ± 0.7	3.13	97.5	23.25 ± 0.74	72
		GPS	60	B_4C~2.36 ± 0.7 TiB_2~2.33 ± 0.8	3.22	100	24.51 ± 1.57	75
	2050	PLS	120	B_4C~2.71 ± 0.8 TiB_2~4.32 ± 1.1	3.23	100	22.97 ± 2.05	71
		PLS	60	B_4C~2.35 ± 0.5 TiB_2~2.74 ± 0.7	3.21	99	24.61 ± 0.84	76
		GPS	60	B_4C~2.13 ± 0.7 TiB_2~2.4 ± 0.6	3.33	100	28.17 ± 0.57	87
	2100	PLS	120	B_4C~29.09 ± 9 TiB_2~19.19 ± 8	3.16	98.4	23.59 ± 5.03	72
		PLS	60	B_4C~31.89 ± 11 TiB_2~8.82 ± 2.4	3.2	98.9	25.79 ± 2.03	80
		GPS	60	B_4C~27.9 ± 7.5 TiB_2~8.11 ± 2.9	3.29	100	26.79 ± 1.59	83
L ρ= 4.26 g/cm^3 B_4C= 25 v% TiB_2= 75 v%	1900	PLS	120	B_4C~1.67 ± 0.5 TiB_2~4.10 ± 1.4	4.27	100	23.87 ± 0.94	87
	2000		120	B_4C~2.79 ± 1.1 TiB_2~6.05 ± 2.3	3.78	92.7	21.65 ± 2.85	78
	2100		120	B_4C~14 ± 4.9 TiB_2~29.6 ± 13.9	4.14	97.3	19.11 ± 1.50	69

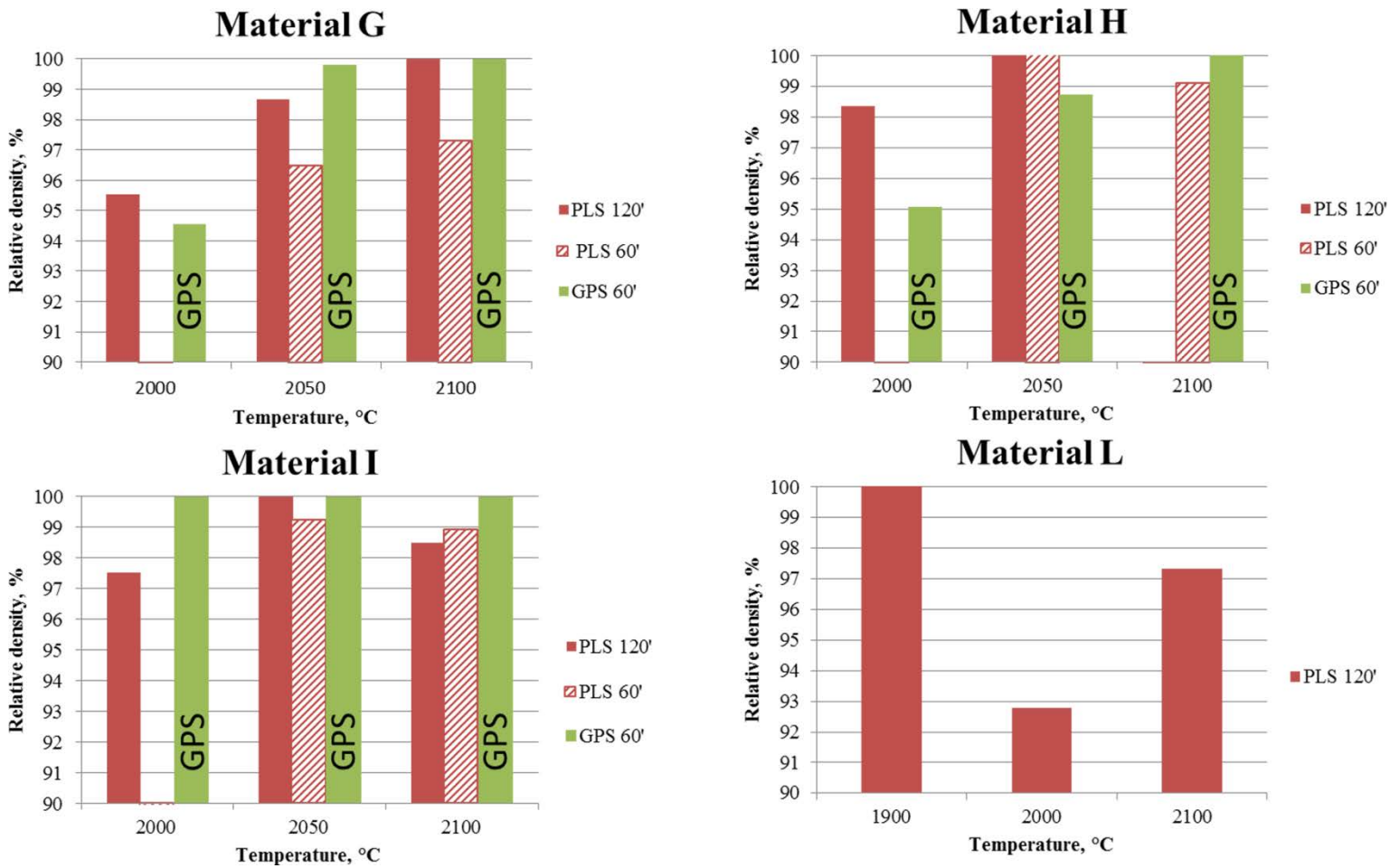

Figure 4.26 Relative density of sintered G, H, I, and L samples obtained with pressureless and gas pressure sintering technique

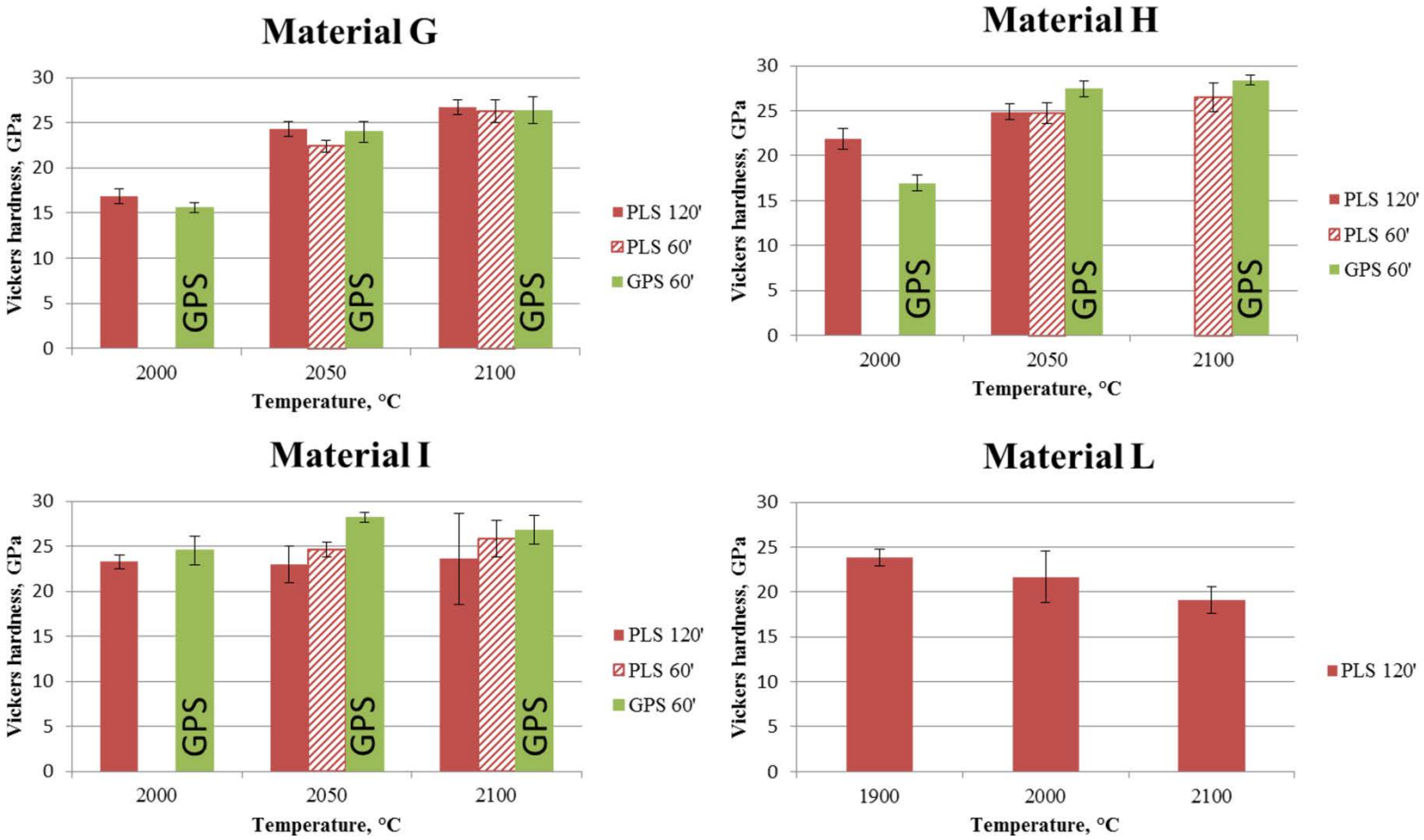

Figure 4.27 Vickers hardness of G, H, I, and L materials obtained with pressureless and gas pressure sintering technique

4.2.2 Microstructural analysis

For all B_4C-TiB_2 compositions of this series of materials, TiB_2 grains had the rim-core microstructure observed in F material (100 v% TiB_2) (*see 4.1.1.3*), where the core is pure TiB_2 and the rim is a solid solution of $(Ti,W)B_2$. W contamination was caused by the wear of WC-6 v% Co grinding media during high-energy milling step.

G material (100% B_4C) – This material had microstructural features that depended on the different thermal cycles discussed in section 5.2.2. The microstructural analysis were performed for materials sintered at 2050 °C and 2100 °C, since they were considered the most promising in terms of relative density. Fig. 4.28 and 4.29 clearly show the different grain size between the two temperatures analyzed. At 2050 °C for all three sintering conditions, the grain size was approximately 2.3 µm. At 2100 °C, grain overgrowth (140- 230 µm) took place. Hence, treatment at 2100 °C was excluded because such large grain size would compromise the mechanical properties of the material.

Microstructural analysis has led to the conclusion that at 2050 °C the density of the sintered material improves by using GPS technique and keeping a dwell time of 60 minutes. Under these conditions, the density of the material (99.8%) exceeded that obtained by using PLS with a dwell time of 120 minutes (98.6%).

W_xB_y phases were detected by EDS qualitative analysis in all sintering conditions (Fig. 4.28 and 4.29). For all the samples sintered at 2100 °C, W_xB_y phases tended to segregate to the grain boundary clearly delimiting the perimeter of the grains as shown in Fig. 4.29. Similar microstructural features was shown by E material (100% B_4C) sintered by HP (see 4.2.4).

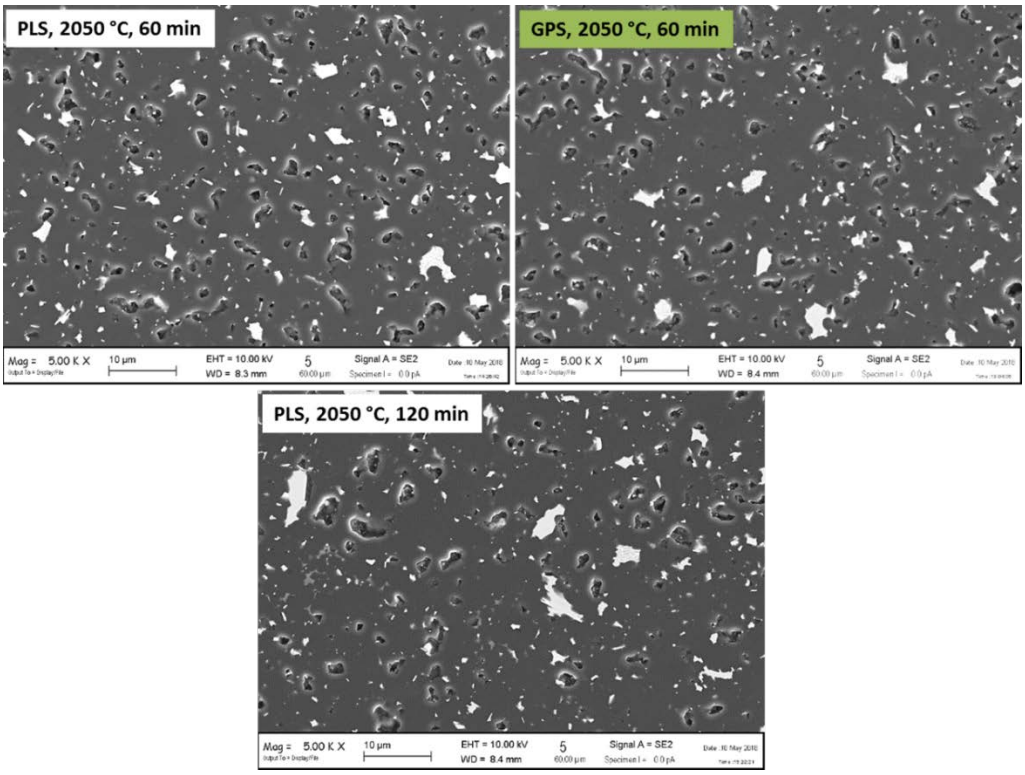

Figure 4.28 FESEM micrographs of G material sintered with PLS and GPS technique at 2050 °C

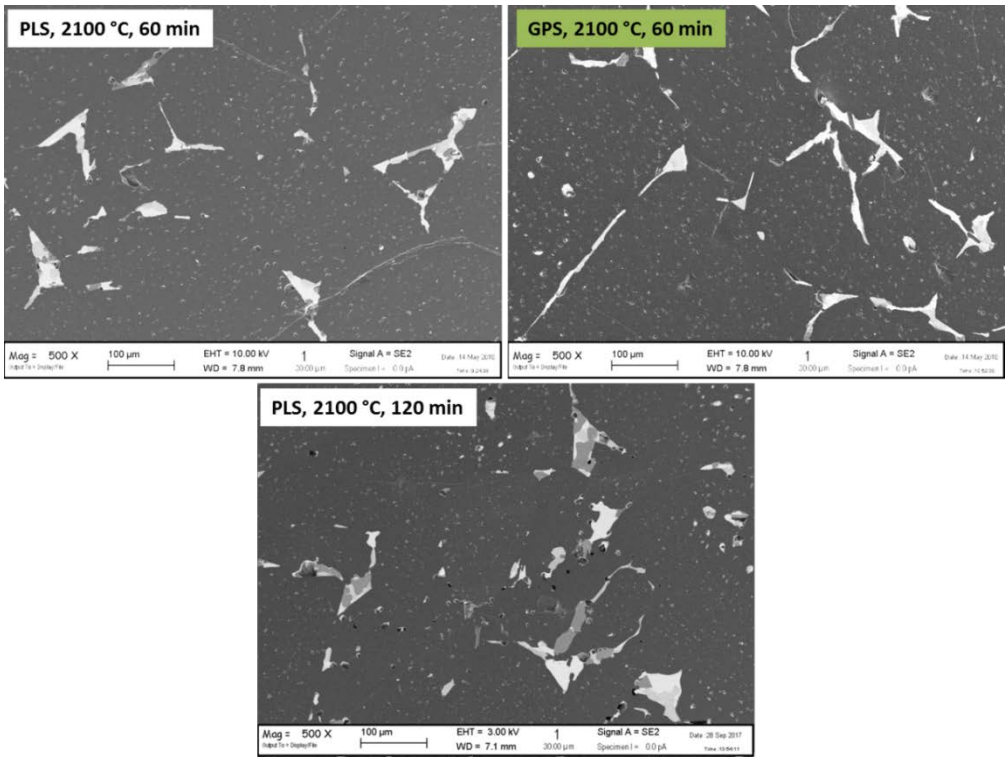

Figure 4.29 FESEM micrographs of G material sintered with PLS and GPS technique at 2100 °C

H material (B_4C 87.5/ TiB_2 12.5) - Also in this case, the microstructural analysis was focused on materials sintered at 2050 °C and 2100 °C, since they were considered the most promising in terms of relative density. The synergistic effect of powder refining with WC aid has led to a microstructure having a smaller grain size with the presence of a solid solution, Fig. 4.30. TiB_2 grains showed the rim-core microstructure also observed in F material (100% TiB_2) produced by HP (*see 4.1.1.3*). Due to the high temperatures and the long dwell times, the W, coming from the grinding bodies, and the TiB_2, spread one into the other almost completely making the TiB_2 *core* disappear. From Fig. 4.30 and 4.32, it has been possible to note a large area made mainly of the solid solution (Ti,W)B_2 (*rim*) without *core*. The presence of this solid solution could slightly distort the theoretical density data calculated from the starting powder mixture. Cobalt was present from the tungsten grinding media which containing 6%.

2050 °C - Density of materials was > 98%. The grain size of TiB_2, considering the solid solution, was about 2.6 µm while for B_4C was 2.1 µm. From the comparison of sintered materials at different times it was possible to see that at 120 minutes of dwell time there was the presence of undesired overgrown grains (red arrows in Fig. 4.31 c)). Instead with 60 minutes of dwell time, the material had a good density with a homogeneous particle size distribution. From Fig. 4.30 it was possible to observe a slight difference in terms of porosity between the material prepared by PLS and GPS technique.

2100 °C - at this temperature, the materials were almost completely dense. The average grain size of B_4C and TiB_2 was between 30 µm and 15 µm, respectively (Fig. 4.32).

TiB_2 grains had an inhomogeneous size distribution, from a minimum of 5 µm to a maximum of 26 µm. Also for this composition, the temperature of 2100 °C seemed to be a threshold over that grain overgrowth took place independently of the dwell time.

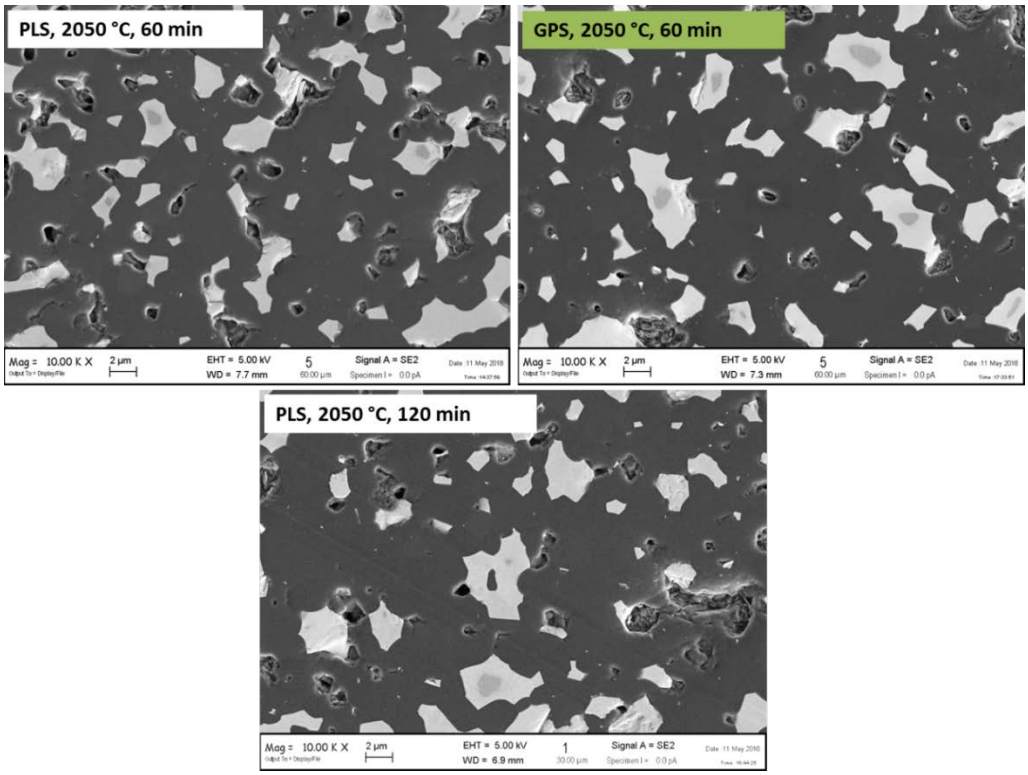

Figure 4.30 FESEM micrographs of H material sintered with PLS and GPS technique at 2050 °C

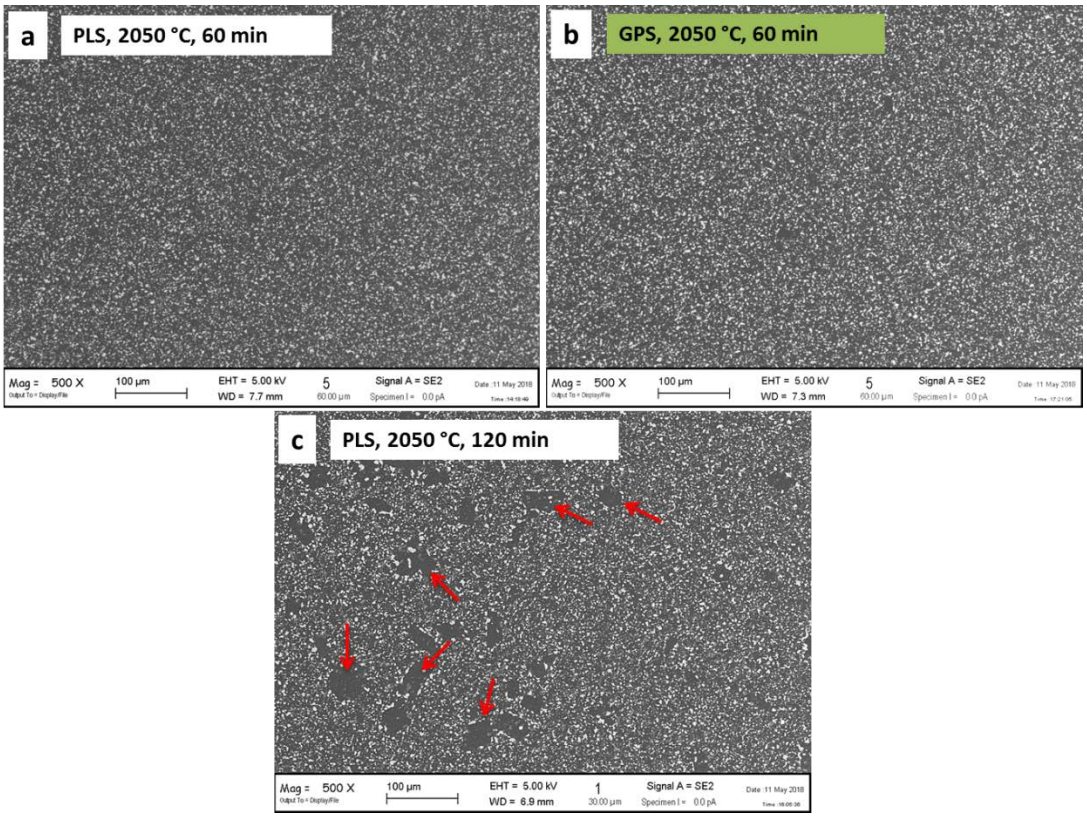

Figure 4.31 Low magnification FESEM micrographs (500X) of the cross section of H material sintered at 2050 °C in PLS and GPS condition with different dwell times

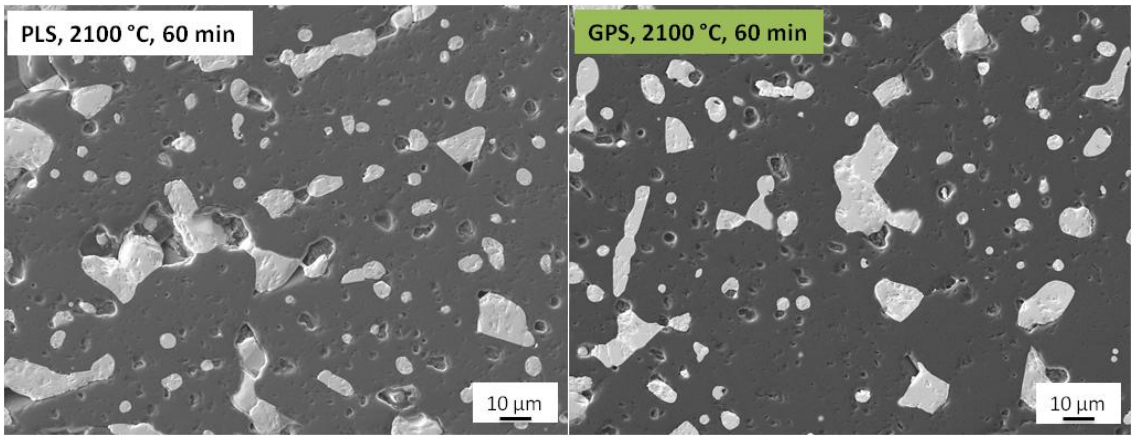

Figure 4.32 FESEM micrographs of H material sintered with PLS and GPS technique at 2100 °C

I material (B_4C 75/ TiB_2 25) - this material had relative density values > 98% for all the heat treatments. TiB_2 grains present the rim-core microstructure up to 2050 °C. Beyond this temperature, TiB_2 phase was completely transformed into a solid solution of $(Ti,W)B_2$. Also in this case Co at the grain boundaries was detected.

2000 °C - the average grain size was about 2.20 and 2.30 µm for B_4C and TiB_2, respectively. This sintering temperature seemed to be sufficient to obtain a proper densification (> 98%) of the mixture with 75 v% of B_4C. However, temperatures above 2000 °C, in both sintering processes: PLS 120 minutes and GPS 60 minutes, were necessary to obtain a full dense microstructure (Fig. 4.33).

2050 °C - in all three sintering conditions (PLS 120 and 60 minutes, and GPS 60 minutes) the samples maintained a satisfactory mean grain size of about 2.4 and 3.15 µm for B_4C and TiB_2, respectively. Material prepared by GPS had an almost no porosity (Fig. 4.34) compared to those sintered by PLS. Hence, gas pressure played a positive role in terms of time, density and grain size.

2100 °C - this temperature led to a grain overgrowth in all conditions of sintering (Fig. 4.35). Mean grain size, obtained by PLS and 120 minutes of permanence, was of 29.10 and 19.2 µm for B_4C and TiB_2, respectively. PLS and GPS, with 60 minute of dwell time, led to 29.90 and 8.45 µm for B_4C and TiB_2, respectively. TiB_2 had an broad particle size distribution for all three conditions examined.

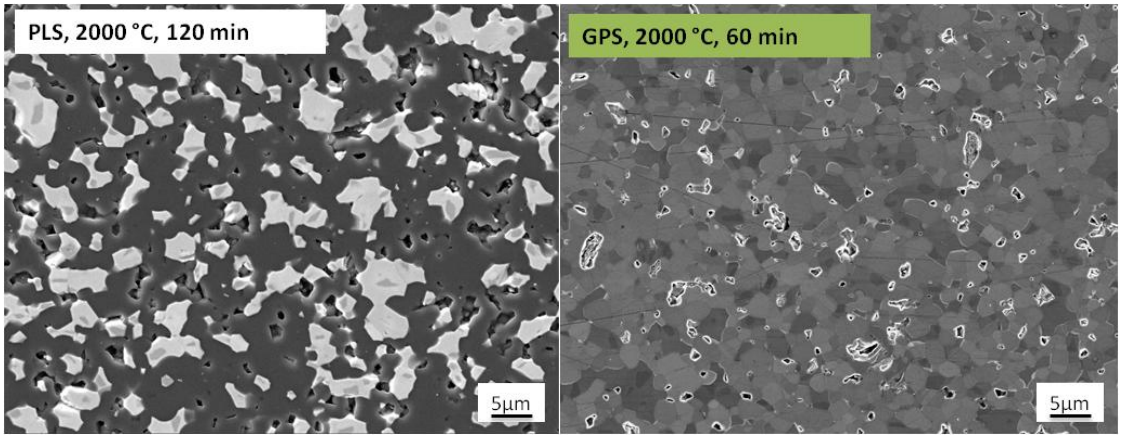

Figure 4.33 FESEM micrographs of I material sintered with the PLS and GPS technique at 2000 °C

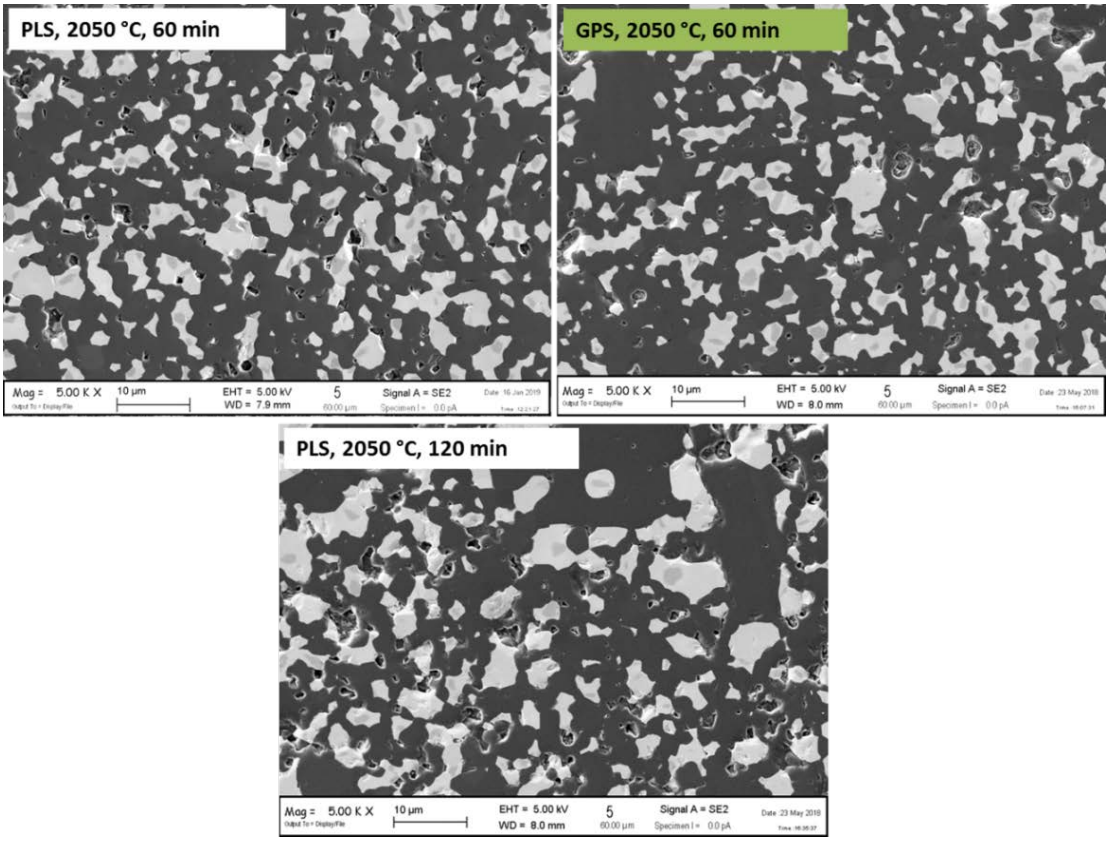

Figure 4.34 FESEM micrographs of I material sintered with the PLS and GPS technique at 2050 °C

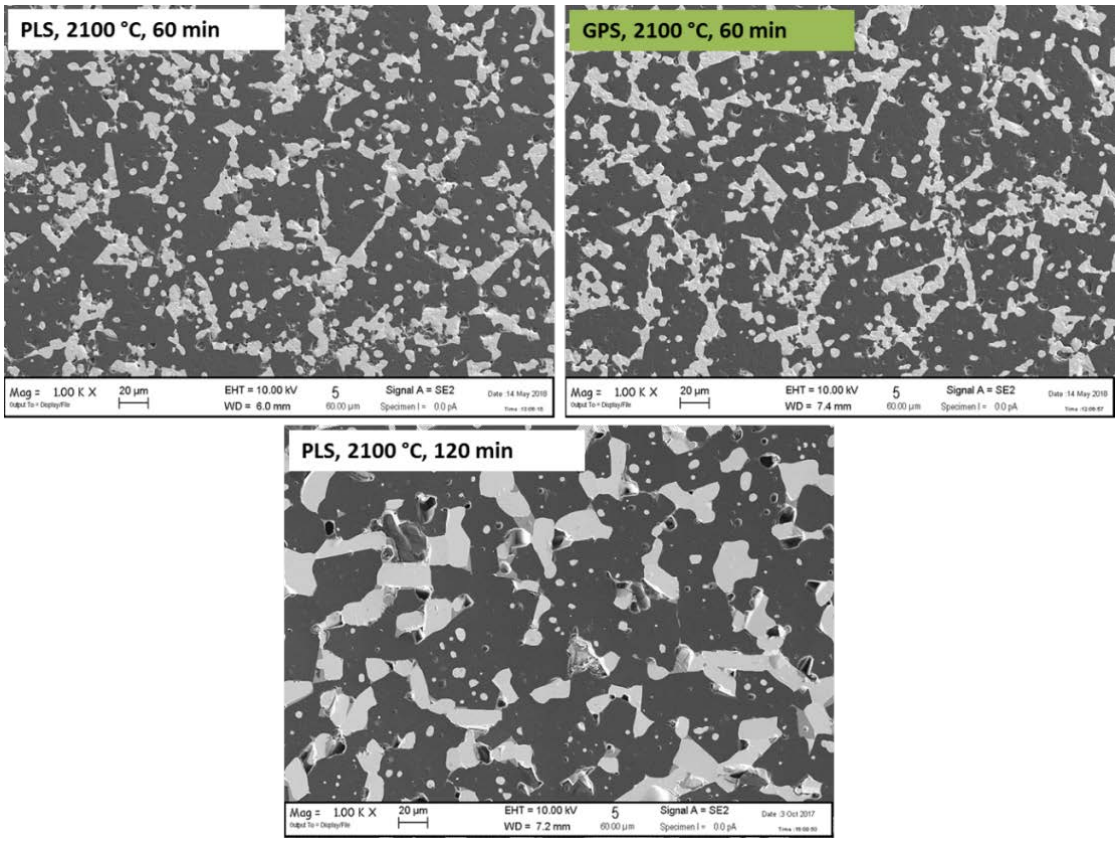

Figure 4.35 FESEM micrographs of I material sintered with the PLS and GPS technique at 2100 °C

L material (B_4C 25/ TiB_2 75) - this material had relative density values of 100% at 1900 °C for 120 minutes. This result was confirmed by the absence of porosity noted by SEM analysis (Fig. 4.36).

1900 °C - mean grain size was 1.67 and 4.10 µm for B_4C and TiB_2, respectively. TiB_2 grains showed the rim-core microstructure typical of the Ti-W-B system (Fig. 4.36). Through EDS (Fig. 4.36) it was possible to observe a double solid solution of B, Ti and W. In fact, higher W content was detected in lighter rim.

2000 °C - mean grain size was 2.79 and 6.50 µm for B_4C and TiB_2, respectively. The low relative density value of 92.78% was confirmed by SEM analysis. From Fig. 4.37 it was possible to note the residual porosity and the rim-core structure. Furthermore, the sample was slightly deformed in the upper part of the surface. Hence, we concluded that the outer zone of the material (hotter during the heating ramp) began to densify faster than the inner zone. At the final temperature of 2000 °C, when the temperature gradient disappeared, gaseous phases (due to the oxides already present in

the starting powders) were trapped in the inner part of the material and led to the deformation of the material.

2100 °C - mean grain size was 14.01 and 29.67 µm for B_4C and TiB_2, respectively. As observed for G, H, and I materials at 2100 °C, there was a large increase in grain growth, especially in the outermost part of the material (Fig. 4.38). This observation was a further confirmation that external area started to densify earlier. In fact, the greater contact between the particles favored the grain growth. Furthermore, the sintered material showed a more pronounced deformation than that observed at 2000 °C. The microstructural analysis showed the formation of very large cracks in the internal area. In the inner part, the smaller grain size could be also favored by the voids leaved by the gaseous phases.

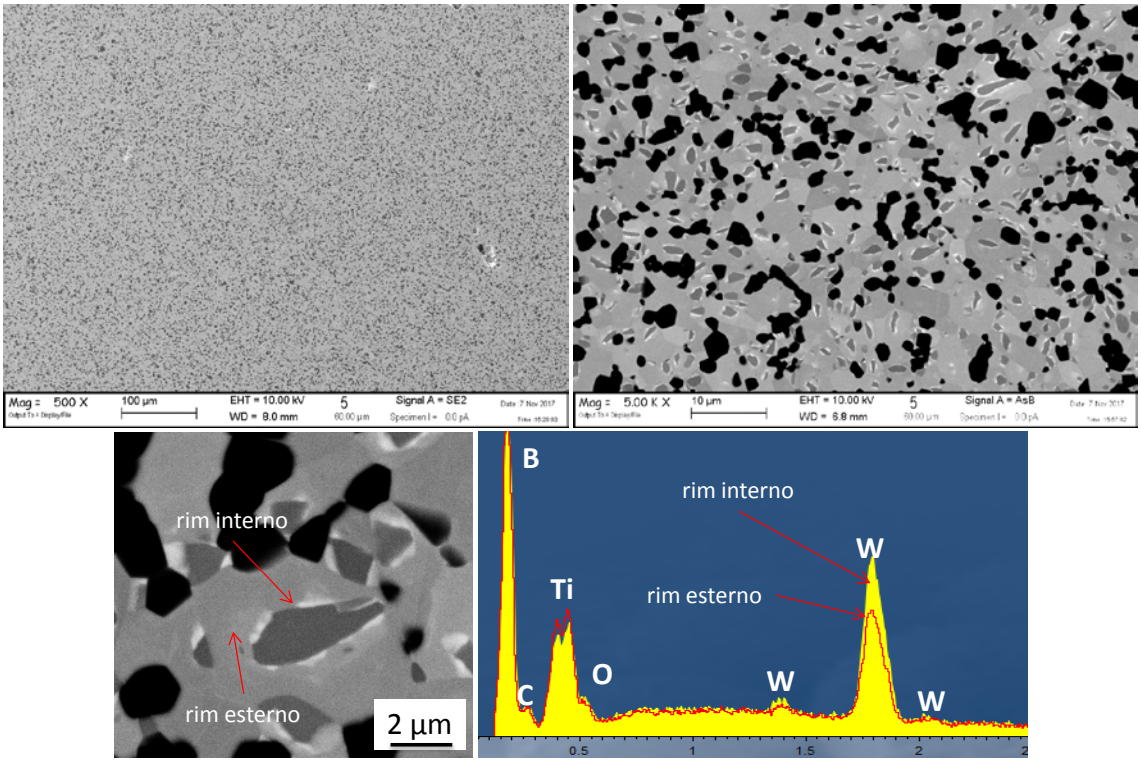

Figure 4.36 FESEM micrographs of L material sintered with PLS technique at 1900 °C for 120 minutes of dwell time with EDS analysis of the double solid solution $(Ti,W)B_2$

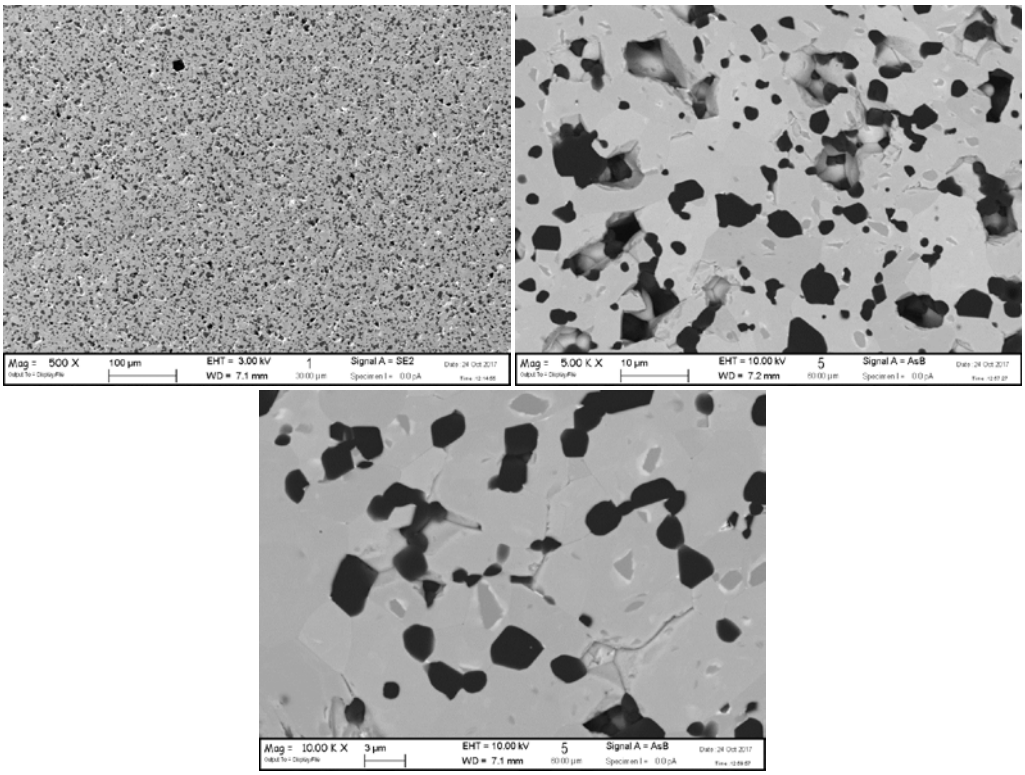

Figure 4.37 FESEM micrographs of P material sintered with PLS technique at 2000 °C for 120 minutes of dwell time

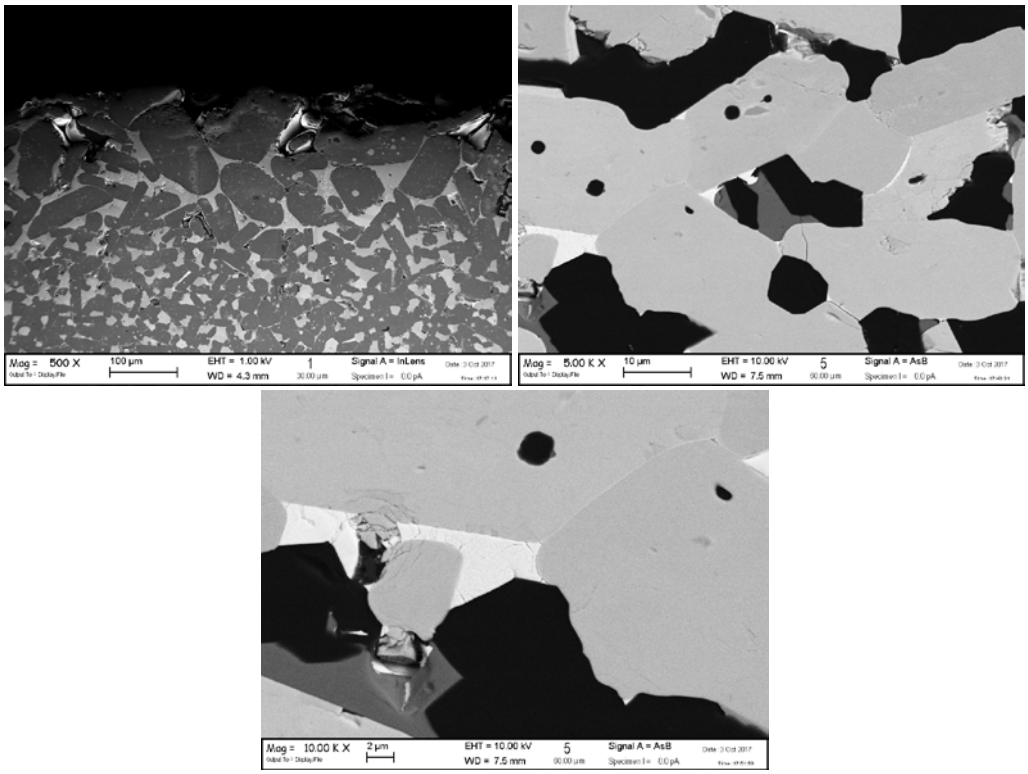

Figure 4.38 FESEM micrographs of L material sintered with PLS technique at 2100 ° C for 120 minutes

4.2.3 Mechanical properties

The carried out microstructural analysis allowed to make a selection of the materials to be mechanically tested. Analyzed mechanical properties were:

- Vickers hardness 1 Kg
- Young modulus
- 4-point flexural strength at room temperature
- Fracture toughness at room temperature

Since the Vickers hardness test required only the polishing of small material surface and is a fairly rapid test, it was decided to subject all the sintered materials to this test.
Table 4.5 and Fig. 4.27 show the values of the hardness. The low hardness obtained at 2000 °C for G, H and I materials for PLS and GPS technique was probably due to the high porosity present in the sintered materials. G materials sintered at 2050 °C showed the same hardness values after GPS, with dwell time of 60 minutes, and PLS with a dwell time of 120 minutes. Also H and I materials showed the same behavior. These results suggested that GPS at 2050 °C, compared to the PLS technique, can further improve the microstructure (see Table 4.5). However in case G, H and I compositions, hardness was slightly lower with respect to the theoretical one of 35 GPa, 33.7 GPa and 32.3 GPa, respectively. G material sintered at 2100 °C had higher hardness than the similar E material obtained with HP technique, and did not dependent of the sintering conditions: PLS/GPS and dwell time. However, since the Vickers indentations of about 26 μm of diagonal fell within a single grain (m.g.s. of 140-230 μm), the hardness did not identify the whole material. For this reason the obtained hardness was lower than the theoretically hardness of for B_4C (33-35 GPa). Hardness of L material followed the same trend of the obtained densities, which increased with decreasing the sintering temperature. In fact, the highest value (23.9 GPa) was find with the sample sintered at the lowest temperature (1900 °C). Hardness values of the other samples (sintered at 2000 and 2100 °C) resulted highly dispersed because the large microstructural inhomogeneity (section 4.2.2).
Further results of mechanical characterization are reported in Table 4.6. This characterization was performed only for those materials showing a hardness higher than 28 GPa (full dense I material produced by PLS was characterized for sake of comparison). Young's modulus and fracture toughness were not strongly affected from

the sintering process and presented values comparable with the theoretical ones. Furthermore, fracture toughness of I material was higher than that of similar composition produced by hot pressing (B75-3 sample, see paragraph 4.1.3.3). Hence, as for I material, the results suggest that GPS positively influenced the microstructure. The low flexural strength of H material should be attributed to the large grain size that hindered the advantages related to the full densification.

Table 4.6 Mechanical properties of H and I materials: hardness, flexural strength, fracture toughness, Young's modulus, relative density

Sample	Sintering (°C/min/technique)	Hardness, (GPa)	Flexural strength, (MPa)	Fracture toughness, ($MPa \cdot m^{0.5}$)	Young's modulus (GPa)	Relative density, (%)
H B_4C= 87.5 v% TiB_2= 12.5 v%	2100/60/GPS	28.38 ± 0.54	371 ± 8	4.48 ± 0.65	452	100
I B_4C= 75 v% TiB_2= 25 v%	2050/120/PLS	22.97 ± 2.05	530 ± 46	5.42 ± 0.29	444	100
	2050/60/GPS	28.17 ± 0.57	825 ± 128	4.71 ± 0.50	473	100

4.2.4 Conclusions

B_4C/TiB_2 mixtures were prepared by using pressureless sintering (PLS) and gas pressure sintering (GPS). The investigated compositions span from 100v% B_4C to 75v% TiB_2. GPS proved to be very useful to produce B_4C, although did not allow to decrease below 2000 °C the need sintering temperature to obtain a density greater than 95%. Conversely, the sample with low amount of B_4C (25 v%) reached full densification at 1900 °C, while higher temperatures caused an evident grain growth and increased the residual porosity.

Finally, it was found that GPS with respect to PLS allowed to reduce the dwell time while improving the mechanical performances. In comparison to hot pressing (HP), GPS led to a comparable bending strength value (σ = 825 ± 128 MPa instead of 815 ± 74 MPa), and higher fracture toughness (σ = 4.7 ± 0.5 $MPa \cdot m^{0.5}$ instead of 3.4 ± 0.1 $MPa \cdot m^{0.5}$)

4.3 References

1. Chamberlain, A. L., Fahrenholtz, W. G. & Hilmas, G. E. High-Strength Zirconium Diboride-Based Ceramics. **1172**, 1170–1172 (2004).
2. Sairam, K. *et al.* Development of B_4C–HfB_2 composites by reaction hot pressing. *Int. J. Refract. Met. Hard Mater.* **35**, 32–40 (2012).
3. Golla, B. R., Bhandari, T., Mukhopadhyay, A. & Basu, B. Titanium Diboride. in

Ultra-High Temperature Ceramics: Materials for ExtremeEnvironment Applications (eds. Fahrenholtz, W. G., Wuchina, E. J., Lee, W. E. & Zhou, Y.) 316–360 (2014). doi:10.1002/9781118700853.ch13

4. Skorokhod, V. & Krstic, V. D. Processing, Microstructure, and Mechanical Properties of B_4C-TiB_2 Particulate Sintered Composites. II. Fracture and mechanical properties. *Powder m* **39**, 504–513 (2000).
5. ZDANIEWSKI, W. A. Solid Solubility Effect on Properties of Titanium Diboride. *J. Am. Ceram. Soc.* **70**, 793–797 (1987).
6. Neuman, E. W., Hilmas, G. E. & Fahrenholtz, W. G. Processing , microstructure , and mechanical properties of zirconium diboride-boron carbide ceramics. *Ceram. Int.* **43**, 6942–6948 (2017).
7. Sarbu, C., Vleugels, J. & Biest, O. Van Der. Phase instability in ZrO_2 – TiB_2 composites. *J. Eur. Ceram. Soc.* **27**, 2203–2208 (2007).
8. Xu, C. *et al.* Spark plasma sintering of B4C ceramics : The effects of milling medium and TiB_2 addition. *Int . J. Refract. Met. Hard Mater.* **30**, 139–144 (2012).
9. Zhang, S. C., Hilmas, G. E. & Fahrenholtz, W. G. Pressureless Densification of Zirconium Diboride with Boron Carbide Additions. *J. Am. Ceram. Soc.* **89**, 1544–1550 (2006).
10. Kim, D. K. & Kim, Chong, H. Pressureless sintering and microstructural development of B_4C-TiB_2 composites. *Adv. Ceram. Mater.* **3**, 52–55 (1988).
11. German, R. M. Liquid phase sintering. in *Sintering Theory and Practice* 225–307 (Jhon Wiley & Sons, Inc, 1996).
12. Ahn, S. & Kang, S. Formation of Core/Rim Structures in Ti(C, N)-WC-Ni Cermets via a Dissolution and Precipitation Process. *J. Am. Ceram. Soc.* **83**, 1489–1494 (2000).
13. Silvestroni, L., Nygren, M. & Sciti, D. Study of the interactions between HfB_2 and Hi-Nicalon^{TM} fiber. *J. Eur. Ceram. Soc.* **33**, 2879–2888 (2013).
14. Kim, H. S. On the rule of mixtures for the hardness of particle reinforced composites. *Mater. Sci. Eng. A* **289**, 30–33 (2000).
15. Taya, M., Hayashi, S., Kobayashi, A. S. & Yoon, H. S. Toughening of a Particulate-Reinforced Ceramic-Matrix Composite by Thermal Residual Stress. *J. Am. Ceram. Soc.* **73**, 1382–1391 (1990).
16. Suri, A. K., Subramanian, C., Sonber, J. K. & Murthy, T. S. R. C. *Synthesis and consolidation of boron carbide: a review*. *International Materials Reviews* **55**, (2010).
17. Skorokhod, V. & Krstic, V. D. High strength-high toughness B_4C-TiB_2 composites. **9**, 237–239 (2000).
18. Kim, H.-W., Koh, Y.-H. & Kim, H.-E. Densification and Mechanical Properties of B_4C with Al_2O_3 as a Sintering Aid. *J. Am. Ceram. Soc.* **83**, 2863–2865 (2000).
19. Wen, Q., Tan, Y., Zhong, Z., Zhang, H. & Zhou, X. High toughness and electrical discharge machinable B_4C-TiB_2-SiC composites fabricated at low sintering temperature. *Mater. Sci. Eng. A* **701**, 338–343 (2017).
20. Zhang, Z. *et al.* Microstructures and mechanical properties of B_4C-SiC intergranular/intragranular nanocomposite ceramics fabricated from B_4C, Si, and graphite powders. *J. Eur. Ceram. Soc.* **34**, 2153–2161 (2014).
21. Torizuka, S., Sato, K., Nishio, H. & Kishi, T. Effect of SiC on Interfacial Reaction and Sintering Mechanism of TiB_2. *J. Am. Ceram. Soc.* **10**, 1606–1610 (1995).
22. Einarsrud, M.-A., Hagen, E., Pettersen, G. & Grande, T. Pressureless Sintering

of Titanium Diboride with Nickel, Nickel Boride, and Iron Additives. *J. Am. Ceram. Soc.* **80**, 3013–3020 (2005).

23. BAIK, S. & BECHER, P. F. Effect of Oxygen Contamination on Densification of TiB_2. *J. Am. Ceram. Soc.* **70**, 527–530 (1987).

5. High toughness UHTCMCs produced by electrophoretic deposition

In this chapter, we exploited EPD to produce salami-inspired architectures (called also non-periodic structures in the following) ZrB_2 and TiB_2 coatings on carbon fabrics. Three different combinations of coating and matrix were produced (Table 5.1). The mechanical properties of the final components were investigated and compared to a similar UHTCMC in terms of fiber volume content and porosity, but characterized by uniformly distributed carbon fibers (below called periodic structure). In particular, fracture energy analysis, based on load-displacement curves obtained from four point bending tests of chevron notched beams, was used to determine if mechanical properties were just affected by the fiber volume content (FVC), or by both FVC and fiber distribution degree. By integrating the area below the load/displacement curve it was possible to obtain the values of work of fracture (WoF) pre- and post-peak, WT and WW respectively, which can be correlated to the toughening mechanism acting on the crack tip and on the wake of the crack.

Table 5.1 Compositions of UHT-CMC materials

Sample ID	Matrix	coating
ZZ	ZrB_2 / 5v% B_4C	ZrB_2
ZT	ZrB_2 / 5v% B_4C	TiB_2
TZ	TiB_2 / 5v% B_4C	ZrB_2
Z	ZrB_2 / 5v% B_4C	Uncoated

5.1 Electrodeposition (EPD)

Figs. 5.1 and 5.2 show C_f bundles coated with ZrB_2 or TiB_2, respectively, by applying electric fields and deposition time between 6 and 11 V/cm, and 5 and 10 min, respectively. It can be seen that the deposited coating increases gradually with the applied electric field and deposition time for both the suspensions.

The thickest and most compact coatings were obtained by applying the electric field of 11 V/cm. In order to ensure a compact coating and minimize crack formation, 11 V/cm and 100 s were selected as electric field and deposition time, respectively.

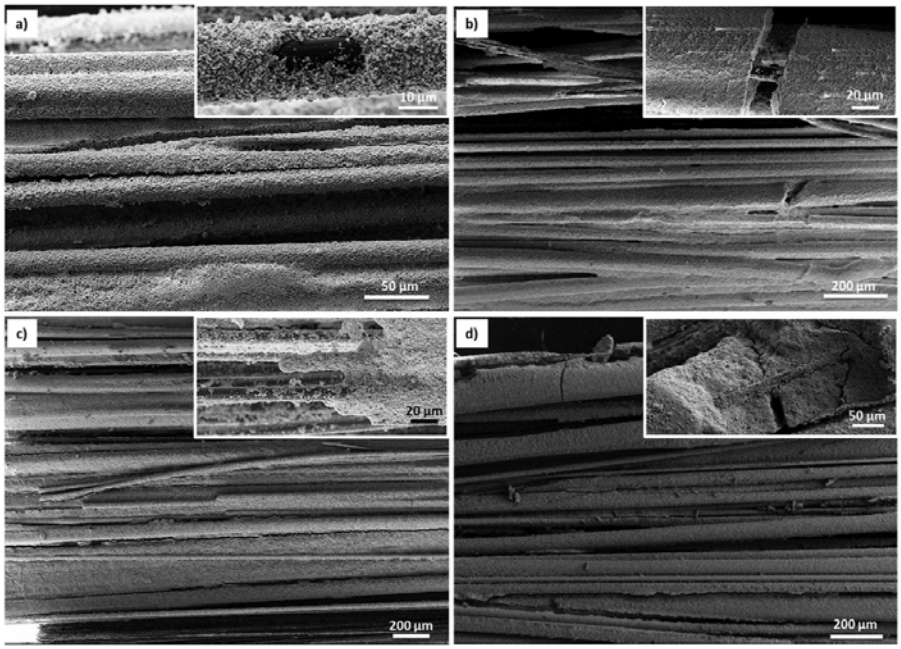

Figure 5.1 Carbon fibers covered with ZrB_2 by EPD at different applied electric field and time: (a) 6 V/cm, 5 min, (b) 11 V/cm, 5 min, (c) 6 V/cm, 10 min, (d) 11 V/cm, 10 min.

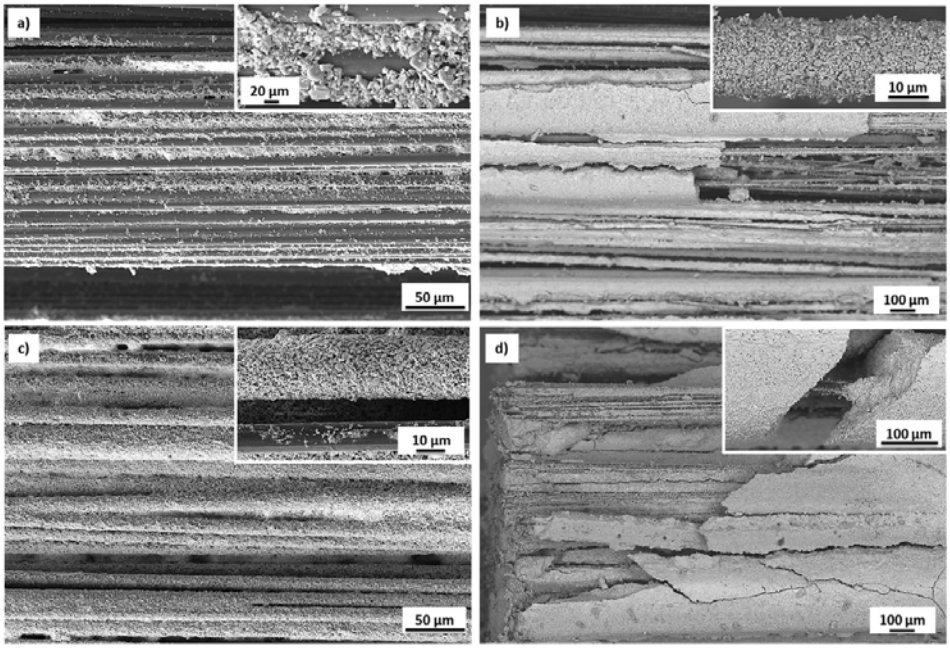

Figure 5.2 Carbon fibers covered with TiB_2 by EPD at different applied electric field and time; (a) 6 V/cm, 5 min, (b) 11 V/cm, 5 min, (c) 6 V/cm, 10 min, (d) 11 V/cm, 10 min.

Fig. 5.3 shows the cross section of C_f bundle after EPD of ZrB_2 obtained under the latter process parameters. EPD produced an external ZrB_2 layer of 15-20 µm thick where the particles were well packed to each other and well stuck to the C_f surface. The cracks on the film and the fibers spreading should be ascribed to the sample preparation. The

coating was formed by particles smaller than 4 μm (the larger particles sediment) and penetrated inside the bundle up to about 100 μm. After that, the inner fibers present a discontinuous coating, being coated by few ZrB_2 particles. Hence if the span between two close fibers is smaller than 6 μm it will be closed during the EPD process by the particles that arrive from the bulk of the suspension. When all the spans (ideally) perpendicular to applied electric field were filled, and the adjacent joined fibers form a continuous wall, the particles from the bulk of suspension cannot penetrate further into the fabric and further increase the external coating which grows up to 15–20 μm.

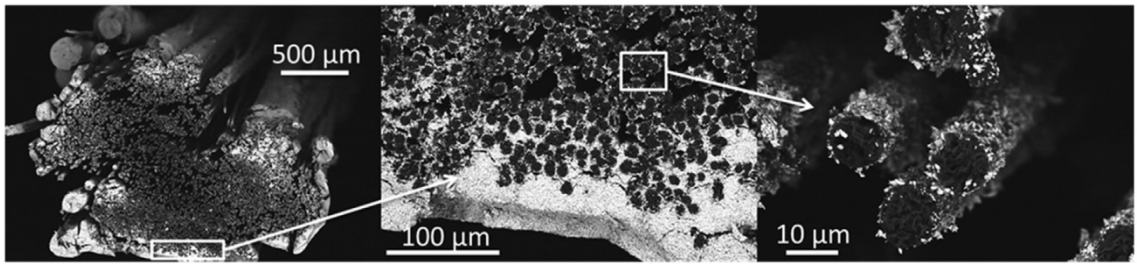

Figure 5.3 Cross section of a single bundle of C_f covered with ZrB_2 by applying an electric field of 11 V/cm for 100 s.

This external layer should give rise to a good adhesion between the C_f bundles and the ZrB_2 matrix as the covalently bonded grafted PB-g-SAN salami-like particles [1]. Another important feature of the coated bundles is the resulted density gradient of parallel C_f between the external and the core of the fabric. It is worth to notice that fiber density is higher at the outer periphery.

5.2 Microstructural analysis

- **ZZ** (ZrB_2-based matrix and ZrB_2 coating) is characterized by a fully dense microstructure with a relative density of 4.1 g/cm^3 and a residual porosity of just 2.1 vol%. The material has 40 vol% of fiber and shows a non-periodic structure (so called "salami" structure [2]) due to the discrete distribution of the bundles inside the matrix, favored by EPD (Fig. 5.4 (a)). Bundles are 200-600 μm thick and about 2 mm wide, as in the original fabrics. EPD covers only the outer shell of each strand (less than 5 layers of C_f [2]), resulting in a well stuck external thick layer of 15-20 μm, while the slurry mostly fills the spaces between the covered bundles, which preserves their pristine configuration also after sintering. Dark spots within the ZrB_2 matrix (the gray area in Fig. 5.4 (b)) were B_4C grains, characterized by a lower density, 2.5 g/cm^3, compared to

the ZrB_2 (6.1 g/cm^3). Observing Fig. 5.4 (b), it is possible to recognize a B_4C-free area at the fiber/matrix interface, 15 μm thick, that can be ascribed to the EPD ZrB_2 coating. The fiber/coating interfaces were characterized by jagged profiles.

- **ZT** (ZrB_2-based matrix and TiB_2 coating) is well densified and presents characteristics in common with both the first two samples (Fig. 5.4 (d)): relative density of 3.8 g/cm^3, 37 vol% of fiber, jagged TiB_2-coating/matrix interface (due to the sintering stresses [2]), and discrete distribution (non-periodic) of fiber bundles in the matrix. On the other hand, ZT presents a thicker coating, approximately 30 and 50 mm.

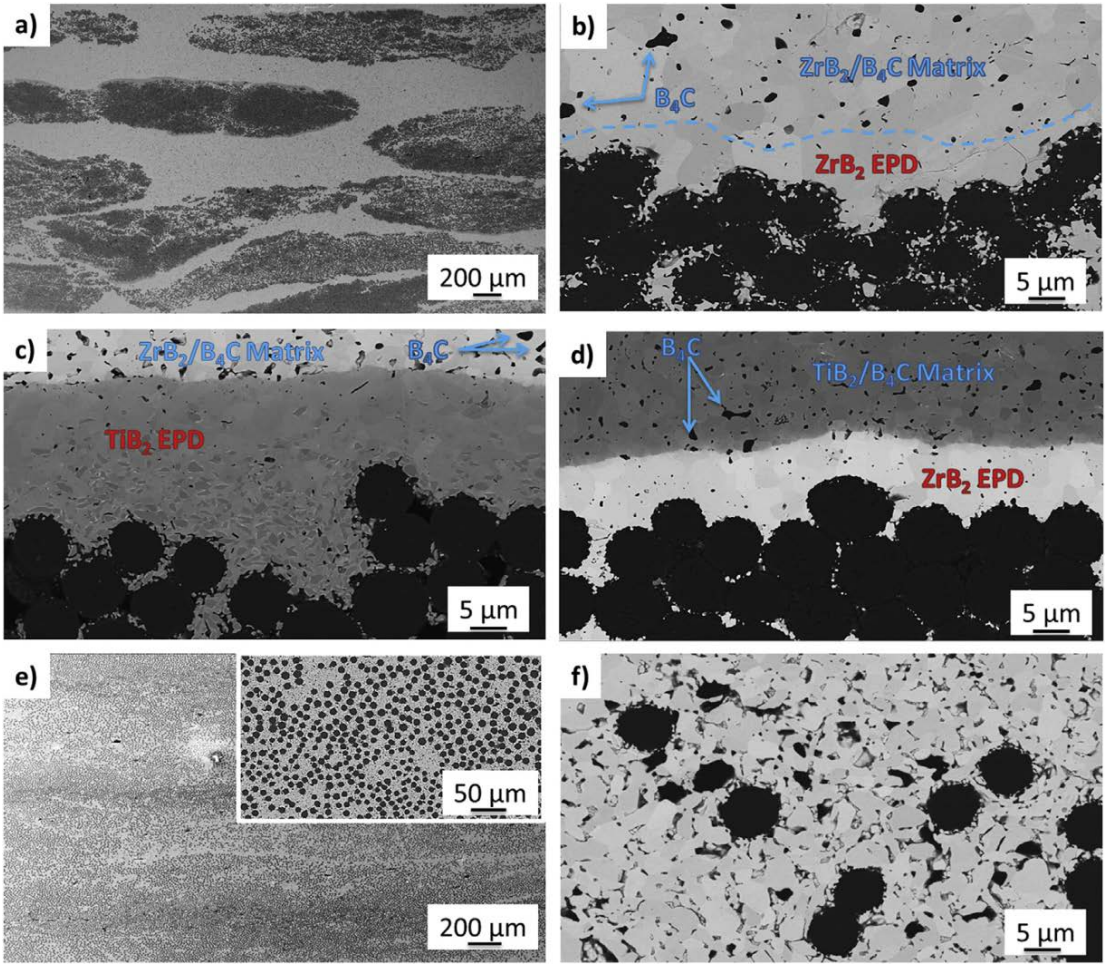

Figure 5.4 SEM micrograph of polished cross section of (a,b) ZZ sample, (c) ZT sample, (d) TZ sample, and (e,f) Z sample.

- **TZ** (TiB_2-based matrix and ZrB_2 coating) shows 3.9 g/cm^3 of density and 33 vol% of fiber. ZrB_2 coating of about 7-20 μm is well recognizable from the matrix due to different contrast displayed in SE/BSE imaging (Fig. 5.4 (c)). Also in this case the

ZrB_2-coated carbon fiber bundles keep memory of the structure of the pristine bundles of the fabrics, displaying a "salami" or non-periodic structure.

- **Z** (ZrB_2-based matrix, no coating): a polished section of this sample, Fig. 5.4 (e and f) reveals the completely different texture of this sample, displaying a homogeneous distribution of C_f inside the matrix. This homogeneous C_f distribution can be described as a periodic configuration, to distinguish it from the non-periodic one of EPD treated samples. Single bundles in periodic case were hardly recognizable. Dark pockets were B_4C particles. The density is 3.97 g/ cm^3, the amount of fiber is 39 vol%. Residual porosity by image analysis is 7.3%.

5.3 Mechanical properties

Values of strength and fracture toughness for the produced samples are reported in Table 5.2.

Table 5.2. Microstructural and mechanical properties. ρ: density; p: porosity; FVC: fiber volume content; K_{Ic}: fracture toughness; W_T: work of fracture at the crack tip; W_W: work of fracture on the crack wake.

Sample	ρ (g/cm^3)	p (%)	FVC (vol%)	σ (MPa)	K_{Ic} ($MPa \cdot m^{0.5}$)	W_T (J/m^2)	W_W (J/m^2)
ZZ	4.1	2.1	40	284 ± 39	11.0 ± 2.4	413 ± 158	954 ± 233
ZT	3.8	8.8	37	278 ± 26	10.7 ± 2.0	333 ± 50	850 ± 391
TZ	3.9	9.2	33	169 ± 23	10.8 ± 0.5	281 ± 56	668 ± 190
Z	4	7.3	39	326 ± 16	7.9 ± 0.7	392 ± 22	500 ± 130

The typical load-displacement curves of ZZ material, characterized by a salami-inspired architecture, are shown in Fig. 5.5 together with the Work of Fracture (WoF) values (the area underlying the load displacement curve divided by the doubled of the projected real surface). The average flexural strength of 284 ± 40 MPa can be ascribed to the jagged matrix/fabrics interfaces, and to higher Cf density at the outer bundles periphery. The former allows a good mechanical coupling between the matrix and the bundles, the latter allows a good stress distribution since the C_f are more concentrated where the stress is larger.

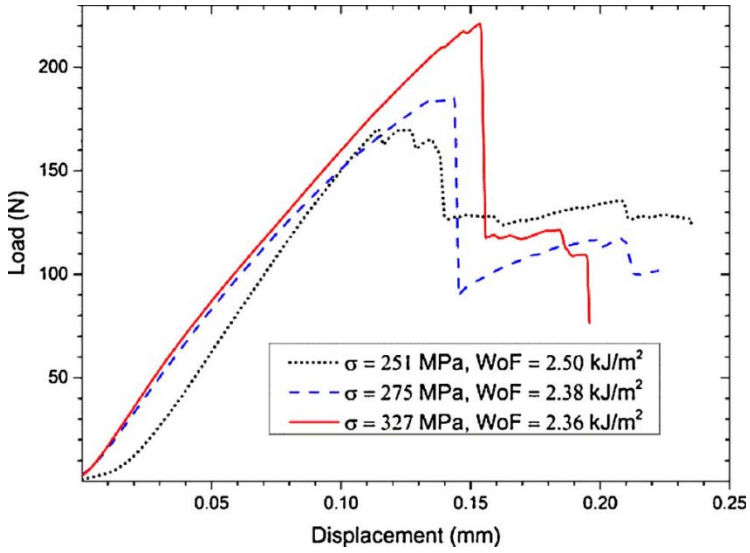

Figure 5.5 Load-displacement curves of 4 pt. for three different bars. The flexural strength (σ) and adsorbed energy (WoF) for each bar is reported.

These phenomena can be considered similar to what occurs in the bamboo plants where the not uniform distribution of the loadbearing fibers enables a more effective and homogeneous stress distribution [3]. It is worth to notice that the maximum flexural strength is still lower than the theoretical value of the side phases. This issue is common for the UHTCMCs and may be due to different reasons such as: tensile residual stress in the matrix due to CTE mismatch with the C_f [4,5], and no perfect alignment of the fibers. The small load drops on the load–displacement curves before the maximum flexural stress can be addressed to delaminations [6,7]. Thus, the shear or local effects which lead to delamination may be the onset cause that will leads to failure. It is likely that delamination starts inside the carbon fabric where the C_f/ZrB_2 and C_f/C_f interfaces were characterized by lower interlaminar shear strength. In order to gain insight into the damage mechanisms occurring during flexural loading, SEM micrographs were taken after failure (Fig. 5.6).

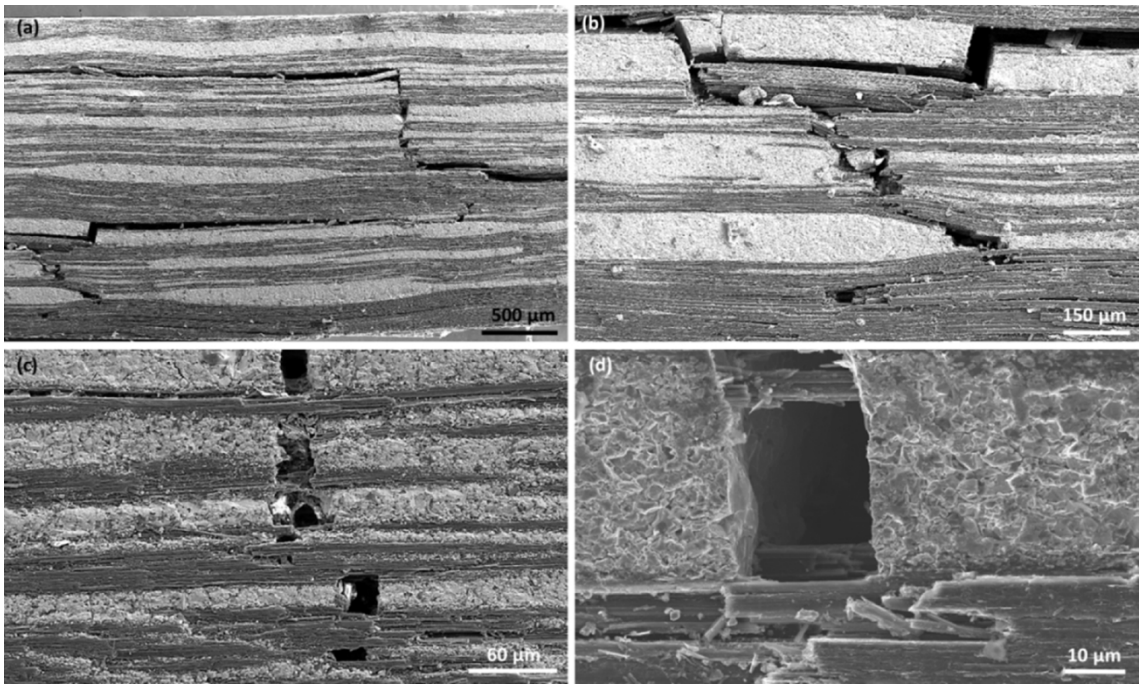

Figure 5.6 SEM images of failed composites under flexural loading.

Interfacial damage and matrix cohesive damage phenomena can be both observed. The cracks deflect inside the bundles and close to the strong matrix/C_f interface. The highly cohesive strength between fibers and matrix prevents the cracks from propagating linearly along their initial directions. The cracks turn to the adjacent layer boundary into the bundles and continue to develop. The resulting crack path is highly tortuous and formed by multiple cracks spread between the layers. This fracture development produces only partial delamination for each layer. This damage mode can sustain further loading, since the C_f inside the bundle stumps remain constrained, and should absorb more energy with consequent improvement in strength and toughness. In a similar way, the grafted PB domains cause an increase of the required fracture energy by facilitating crazing and shearing at the crack tip, and forming fibrils that act on the crack wake [1]. Hence, we think that this salami-inspired architecture on one hand allows a good stress distribution due to the C_f density gradient from inner to outer periphery of bundles. On the other side, the combination of strong (jagged) outer and (weak) inner interfaces prevents both the brittle failure of composites due to strong phases bonding and the easy interfacial debonding under low loading, in case of too weak interfaces. The fracture energy of 2.41 ± 0.08 kJ/m^2 is higher than that shown by similar materials (about 0.1 kJ/m^2 [8]). The WoF decreases down to 1.4 kJ/m^2 if it is calculated from the load-displacement curves of CNB (Fig. 5.7), due to the stress concentration at the notch.

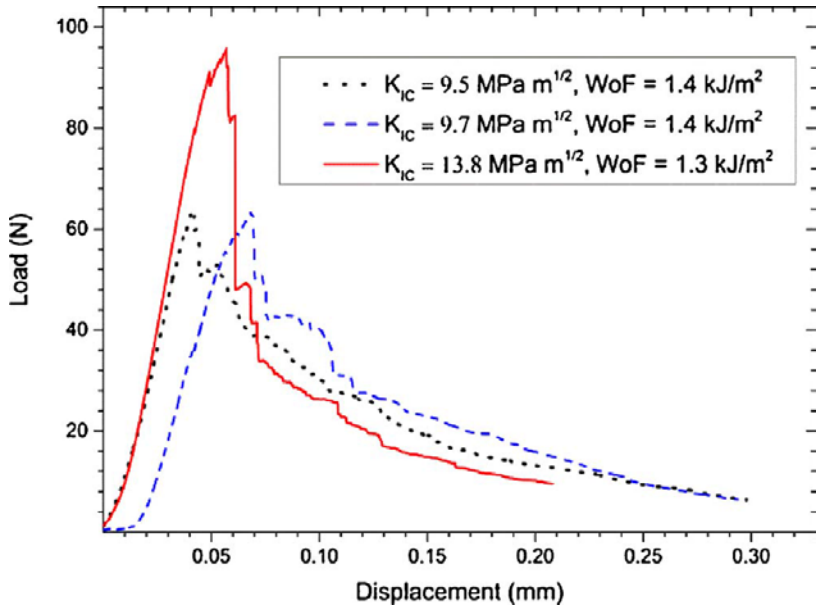

Figure 5.7 Load-displacement curves of 4 pt. fracture for three different chevron notched beams (CNB). The fracture toughness (K_{IC}) and adsorbed energy (WoF) for each CNB is reported.

Nevertheless, this value is still one order of magnitude larger than those shown by similar materials. The increase in fracture energy matches the increase of toughness to about 11 ± 2.5 MPa·$m^{0.5}$ (Fig. 5.8). In fact, as a general rule, cracks do not easily propagate in a material characterized by a high WoF. As seen above, the strong jagged interface between matrix and C_f acts as hindrance for the crack propagation. The crack may be stopped at that interface and activates further toughening mechanisms such as microcracking inside the bundles − where the C_f/C_f and C_f/ZrB_2 were characterized by a lower interfacial strength − and the consecutive crack deflection and propagation along the perpendicular direction. Crack deflection at the weaker interfaces is similar to what occurs in the bioinspired nacre-like composites where a weakness point is needed to fully activate the toughening mechanisms and induces the crack propagation parallel to long axis of platelet (C_f in our case) [9]. In our opinion, such an intricate microstructure gives rise to further toughening mechanisms during fracture including friction and interlocking of entire bundles of C_f, and the pull-out of single C_f from the same bundles. From the fracture surface of CNB specimens that exhibit the lowest and highest fracture toughness (9.5 MPa·$m^{0.5}$ (Fig. 5.9(a)–(c)), and 13.8 MPa·$m^{0.5}$ (Fig. 5.8(d)–(f)), respectively), it is possible to make some qualitative considerations about the different toughening mechanisms. In both samples the matrix between the fabrics shows a brittle behavior and the cleavage fracture is quite flat. The crack likely propagates through the

matrix with a transgranular mode. In contrast, the volumetric shuffling of the material inside the fabrics is the consequence of the crack deflections.

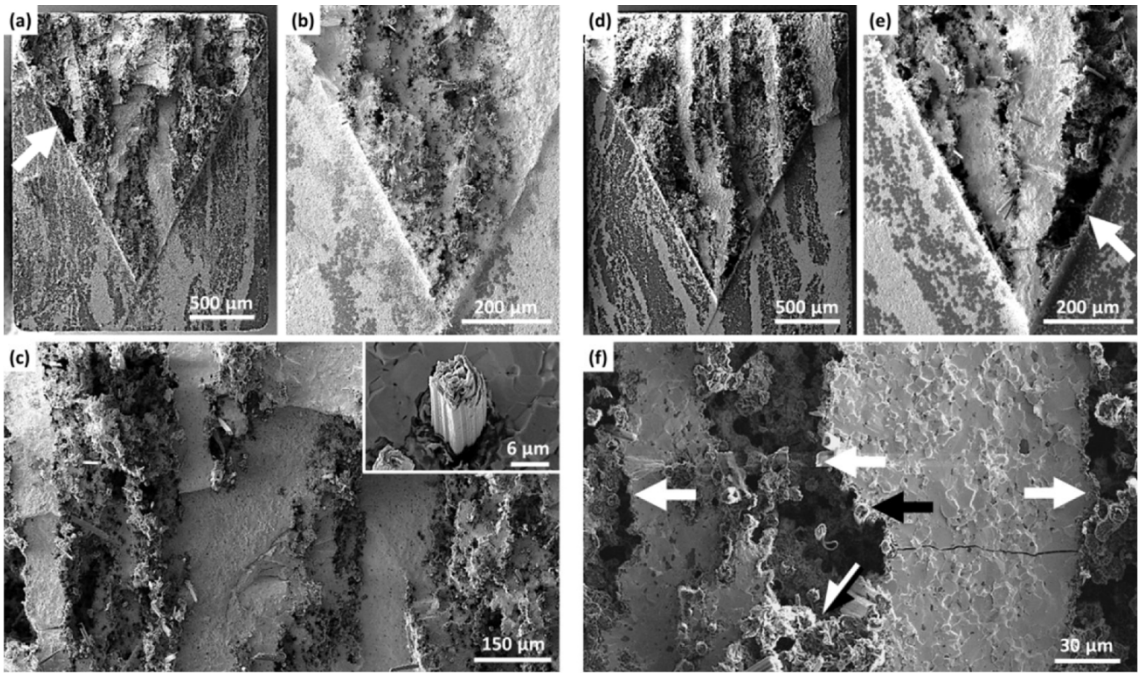

Figure 5.8 Transversal SEM images of failed CNB under flexural loading. (a)-(c) and (d)-(f) correspond to dotted line (K_{IC} = 9.5 MPa·$m^{0.5}$) and solid line (K_{IC} =13.8 MPa·$m^{0.5}$) in Fig. 5.8, respectively. The white arrows point some of the footprints left by the pull-out of the so called salami. The black arrow and the black and white one point a strong jagged matrix/fabric interface and a weak C_f/C_f interface, respectively.

It is worth to remember that crack deflection is triggered inside the fabrics by the process zone at the crack tip. Thus the weak interfacial resistance between C_f/C_f and C_f/ZrB_2 (that characterized by a low ZrB_2/C_f ratio) inside the fabrics is necessary to take full advantage of the toughening mechanisms. The extensive delamination parallel to the C_f and the propagation of the crack mainly through the matrix leave uncracked-bundles bridges. These bridges should act as intact regions spanning the crack wake to inhibit its progress by further microcracking inside the bundles, and crack deflection along the transverse orientation to the main fracture surface. At the end of the fracture processes, the salami-inspired UHTCMCs should fail under bundle pull-out mode. Some of the footprints leaved by the pull-out of the so called salami are pointed by the white arrows in Fig. 5.8. In Fig. 5.8(f) it is clearer how their cross section appears like a slice of salami. In particular, in Fig. 5.8(f), it can be seen that the strong jagged interface of the fabrics is broken at the same level of the matrix, proving the good stress

transmission across these strong interfaces. Moreover, it suggests that the inelastic energy dissipation through the friction interactions during the pull-out of the salami occurs at the weaker interface inside the fabrics. Based on the above discussion, it is reasonable to address the higher K_{IC} value as due to the higher amount of the footprints left from the pull-out of the salami bundles. The deep holes left by the salami pull-out can be justified by adapting the Kelly-Tyson model [10]:

$$l_c = \frac{\sigma \cdot r}{\tau} \quad (1)$$

where l_c is the critical length and corresponds to the lengths/depth of the fragments/hole formed after the pull-out. σ is the flexural stress of the salami (the EPD Cf fabrics), r is the equivalent radius of the projected area of the salami (the footprints leaved by its pull-out), and τ is shear stress at the weaker C_f/C_f or C_f/ZrB_2 interphases. From the Eq. (1) it is clear that the pull-out of a bundle of C_f, due to the weak interphases strength (small τ) and large area (r), brings to large value of l_c, and thus dissipates a large amount of inelastic energy. On the other hand, the pull-out of the single C_f embedded in the matrix is characterized by a small l_c, about 10 μm (Fig. 5.8 (c)). In any case, the interface debonding did not occur at the strong (jagged) interface, but inside the fiber between weakly bonded inner layers. As it can be seen in Fig. 5.8 (e), l_c of the single pulled-out carbon fibers inside the fabrics were one order of magnitude larger than those embedded in the matrix. In fact, as said above, the interlocking thickness (i.e. the value of τ) between ZrB_2 grains and C_f is larger along the external matrix/fabric interface rather than ZrB_2/C_f interfaces inside the fabrics. In Fig. 5.9 sketch of the toughening mechanisms produced by the (a) salami-inspired C_f/ZrB_2 UHTCMCs and (b) salami-like particles is drawn. The red line represents the crack pathway. It can be seen how, for both the ceramic (Fig. 5.9(a)) and polymeric (Fig. 5.9(b)) composites, the crack tortuosity can be enhanced by microcracking and crack deflection ahead of the crack tip.

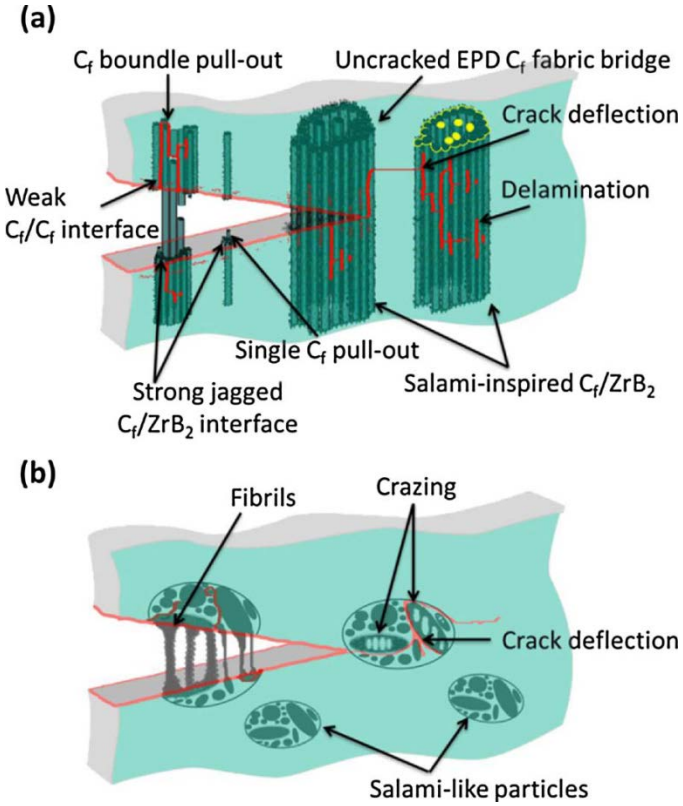

Figure 5.9 Sketch of the toughening mechanisms produced by the (a) salami-inspired C_f/ZrB_2 UHTCMCs and (b) salami-like particles. The red line and the yellow one represent the crack pathway and the cross section of a salami-inspired reinforcement, respectively.

For this goal, first of all, a strong mechanical coupling between the matrix and the reinforcement phase is required, as the jagged interfaces and the grafting for C_f/ZrB_2 UHTCMCs and PB-g-SAN, respectively. Then, the good stress distribution should allow the activation of toughening mechanisms inside the reinforcement phase, such as delamination and crazing. These crack pathways leave entire parts of the reinforcement components like the uncracked-bundle bridges for the salami-inspired composites (the cross section appears like a slice of salami), and rubber fibrils for the salami-like particles dispersed in the polystyrene matrix. These latter components give the larger extrinsic contribution that act behind the crack tip and inhibit its propagation. The resulting damage tolerance, c, according with the Irwin equation:

$$c = \frac{K_{IC}^2}{\pi\sigma^2} \qquad (2)$$

is 473 ± 89 μm. This value is significantly higher that of the conventional ceramics of about 0.1–1 μm [11] and ZrB_2-based ceramics of about 6 μm considering typical values of

strength (~800 MPa and toughness 3.5 MPa·m$^{0.5}$ [12]), and approaches the lower bound of the engineering metals (Fig. 5.10).

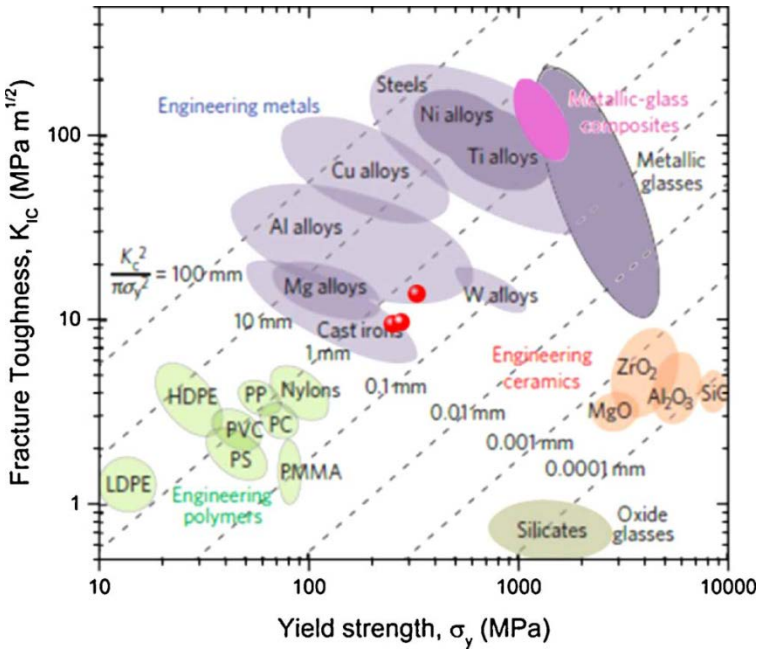

Figure 5.10 Data of fracture toughness (Fig. 5.8) vs. flexural strength (Fig. 5.5) plotted as red spheres on Ashby map redrawn from Ref. [11]. The different levels of damage tolerance are marked with the dotted lines.

These results suggest that salami-inspired UHTCMCs can be exploited in order to overcome the mutual exclusive properties of strength and toughness and allow to develop strong fiber reinforced ceramic composites with a high resistance catastrophic failure. Finally, although comparison with results available in the literature could be unreliable due to different preforms/matrix composition/ process/measurement techniques, it is worthy to notice that our values of strength and toughness were well in agreement with those obtained for other UHTCMCs mostly obtained through enrichment of C/SiC matrix with the UHTC phase [13–15].

The uncoated material, Z, has the highest strength (~330 MPa) due to homogeneous microstructure, which ensures the good mechanical stresses transfer between matrix and fibers. ZZ and ZT, with ZrB_2 matrix and ZrB_2 or TiB_2 coating respectively, both display a strength of ~280 MPa, independent of the different nature of the coating and the different fraction of residual porosity. Sample TZ, with TiB_2 matrix and ZrB_2 coating has the lowest strength, ~170 MPa, probably due to the lowest fiber volume content (FVC) (Fig. 5.5 (a)). In Fig. 5.11 (a,b), experimental data of σ, K_{Ic}, W_T, and W_W for

non-periodic and periodic microstructures were plotted as function of FVC in order to assess whether or not there is some dependence. In case of s a linear dependence on FVC is expected.

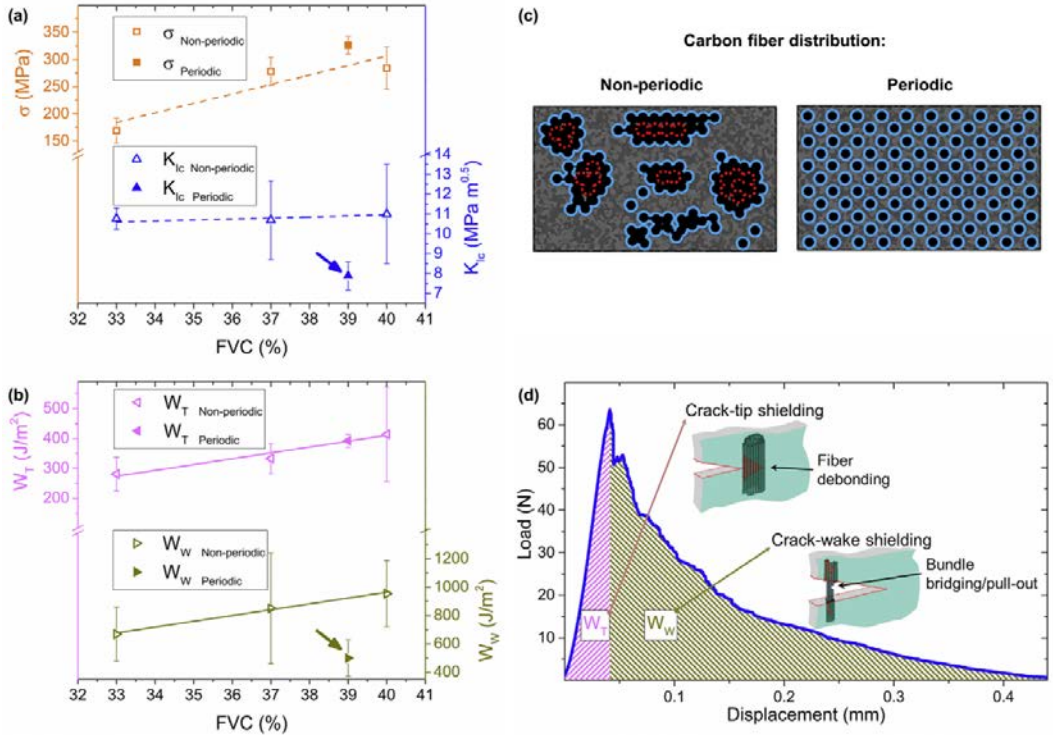

Figure 5.11 (a) Flexural strength, s, and fracture toughness, K_{Ic}, as function of the fiber volume content (FVC). (b) Work of fracture at the crack tip, W_T, and work of fracture at the crack wake, W_W, vs. FVC. Left hand ordinates refer to the distribution-independent properties: σ and W_T. Right hand ordinates refer to the distribution-dependent properties: K_{Ic} and W_W. Arrows point the outlier points. (c) Sketch of non-periodic (salami-inspired architecture) and periodic carbon fiber distribution, where strong and weak interfaces are highlighted with solid blue lines and dotted red lines, respectively. (d) Load vs. displacement curve obtained whit the chevron-notched three-point bend fracture toughness technique.

In fact, due to the iso-strain condition imposed by the test configuration σ is a linear function of FVC according with the linear rule of mixtures:

$$\sigma = \sigma_f \cdot V_f + \sigma_m \cdot (1 - V_f) \quad (3)$$

where V_f was FVC, σ_f and σ_m were the strength of the fibers (3.4 GPa) and the matrix (65 MPa [16]), respectively. The lack of fit of the linear regression between s and FVC (R^2 = 0.88) and the gap of about 80% between the experimental values and the predicted

ones by Eq. (3) can be mainly addressed to mixed failure mode (tensile + shear), which underestimates the apparent measured σ, and to the concomitance of others microstructural variables such as porosity, matrix and coating composition, fibers alignment, etc. Anyway, it is reasonable to say that σ depends more on FVC rather than fiber distribution degree. In fact, the correlation coefficient (r) indicates a strong agreement between σ and FVC both in the case we consider all the samples (r= +0.91) and in the case we exclude Z (r= +0.92). It is worth to remind that r = +1 indicates the strongest possible agreement, and r = -1 the strongest possible disagreement. As for the toughness, the striking difference the periodic Z baseline material, 7.7 $MPa \cdot m^{0.5}$, and the non-periodic (EPD derived) samples, about 11 $MPa \cdot m^{0.5}$, confirms the EPD-step effect on the mechanical properties. This large increment of toughness was attributed to the specific texture obtained, where the discrete distribution of carbon bundles inside the matrix (non-periodic distribution) allows the synergic activation of diverse toughening mechanisms that contributed to enhance the overall toughness and damage tolerance [2]. In particular the bundles, owing to the presence of weak C_f/C_f or C_f/ZrB_2 interfaces inside (as sketched in Fig. 5.11 (c)), allow a large pull-out length according to the adapted Kelly-Tyson model [2](Eq.1). In fact, contrary to the σ trend, K_{Ic} is strongly affected by the degree of fiber dispersion as proved by the increase of r from -0.32 to +0.68 with the Z value exclusion. In Fig. 5.5 (a), it can be seen how the fracture toughness increases with the increasing of FVC and is boosted by the so called “salami” structure [2] realized in the non-periodic sample. The toughness value of periodic Z sample appears as an outlier point 27% lower than the linear regression fitting of the non-periodic samples. The low r value of +0.68 reflects the dubious validity, in case of continuous-fiber-reinforced ceramic matrix composites, of the K_{Ic} values. Even if it is praxis to provide toughness values for CMCs, not always the crack-stability criterion is investigated, and the tests with CNBs could not simultaneously fulfill the plane-strain condition and limited crack tip plasticity (microcracking, fiber debonding, etc.). Moreover in the case of CMCs, the current standards do not establish any specimen-size criteria to take into account the crack wake plasticity (fiber/ boundless pull-out). These phenomena, typical belonging to the continuous-fiber-reinforced composites, are in contrast with the usual assumption of a flat crack-growth-resistance curve, and could lead to extend the stable crack growth beyond the maximum load. For the above reasons, giving a valid K_{Ic} determination method for UHTCMCs is challenging. To

avoid this tricky point, we performed a WoF analysis. The idea (sketched in Fig. 5.11 (d)) is to correlate the work spent to reach the maximum load (W_T), and the following work spent up to the ultimate displacement (W_W) to the toughening mechanisms activated ahead of the crack tip (microcracking, fiber debonding, etc.), and on crack wake (fiber/bundle pull-out), respectively. This analysis suggests that the toughening mechanisms ahead of the crack tip were enhanced by FVC, and were independent of fiber distribution degree (Fig. 5.11 (b)). In fact, r remains roughly the same (+0.98) whether we consider the periodic structure or not. On the contrary, W_W is strongly affected by the degree of fiber dispersion (Fig. 5.11 (c)) as proved by the increase of r from +0.24 to +0.997 with the Z value exclusion. The obtained value of r= +0.997, is in agreement with the expected behaviour of the toughening contributions, and reinforces the hypothesis behind the used WoF analysis. On the other hand, no strong correlations were identified between the investigated mechanical properties and the microstructural features, such as matrix and coating composition, coating thickness, and porosity. The mechanical properties of the investigated materials seem to be controlled by FVC and its distribution degree (periodic or non-periodic structure). A possible implication of the proposed WoF analysis is that to use it as test to evaluate pull-out toughening, which is proportional to W_W. The WoF analysis is easier to perform respect to push-in and push-out techniques which requires thin sample. In fact, the thickness should be less than one-tenth compared to the diameter of the fiber in order to avoid fiber buckling. Moreover, if high thermal residual stresses were present, as for the case of UHTCMCs, the machining can induce a stress releasing as a consequence of the matrix cracking [17].

5.4 Conclusions

The deposition of UHTC coating on carbon fabrics through EPD process is shown. The slurry infiltration of coated carbon fabric fills the intra-fiber woven regions without affects the outer EPD coating which successfully withstands subsequent manufacturing steps of UHTCMCs. The resulting microstructure consists in electrophoretic coated fabrics dispersed in a fully dense ceramic matrix. The fabrics were characterized by a functionally graded concentration of fibers that is higher at the outer periphery and where the bonding of the fibers with the sintered matrix is strong. The effect of such substructures obtained by EPD was assimilated to that of the salami-like particles in the PB-g-SAN polymer. The salami-inspired bundles increase flexural strength and enhances the extrinsic crack-tip-shielding mechanisms leading to very high fracture

toughness. Evaluation of the fiber volume content (FVC) on the UHTCMCs fracture resistance, including fracture strength (σ), fracture toughness (K_{Ic}), work of fracture (WoF) at the crack tip (W_T), and WoF at the crack wake (W_W), indicates that:

- higher FVC, in the range of 33-40%, generates higher σ, K_{Ic}, W_T, and W_W
- K_{Ic} and W_W were highly sensitive to the degree of fiber distribution, whereas σ and W_T were not.
- Non-periodic specimens, characterized by "salami" substructures, exhibit higher fracture resistance than periodic samples. Hence, the crack shielding can be enhanced by a non-periodic distribution of the fibers.

The unusual combination of low density ($\rho \sim 4$ g/cm^3), strength and high resistance against fracture allows the production of UHTCMC with high damage tolerance (c= 570 μm) that can improve the structural component for aerospace applications. Finally, results indicate that the combination of too strong (jagged) outer interfaces and too weak (inner) interfaces can be exploited as an alternative method to achieve an overall ideal weak fiber/matrix interface.

5.5 Reference

1. Heckmann, W., McKee, G. E. & Ramsteiner, F. Structure-property relationships in rubber-modified styrenic polymers. *Macromol. Symp.* **214**, 85–96 (2004).
2. Galizia, P., Failla, S., Zoli, L. & Sciti, D. Tough salami-inspired Cf/ZrB_2 UHTCMCs produced by electrophoretic deposition. *J. Eur. Ceram. Soc.* **38**, 403–409 (2018).
3. Wegst, U. G. K., Bai, H., Saiz, E., Tomsia, A. P. & Ritchie, R. O. Bioinspired structural materials. *Nat. Mater.* **14**, 23–36 (2015).
4. Monteverde, F., Guicciardi, S. & Bellosi, A. Advances in microstructure and mechanical properties of zirconium diboride based ceramics. *Mater. Sci. Eng. A* **346**, 310–319 (2003).
5. Pradere, C. & Sauder, C. Transverse and longitudinal coefficient of thermal expansion of carbon fibers at high temperatures (300-2500 K). *Carbon N. Y.* **46**, 1874–1884 (2008).
6. Caminero, M. A., Rodríguez, G. P. & Muñoz, V. Effect of stacking sequence on Charpy impact and flexural damage behavior of composite laminates. *Compos. Struct.* **136**, 345–357 (2016).
7. Agrawal, S., Singh, K. K. & Sarkar, P. K. Impact damage on fibre-reinforced polymer matrix composite - A review. *J. Compos. Mater.* **48**, 317–332 (2014).
8. Silvestroni, L., Sciti, D., Hilmas, G. E., Fahrenholtz, W. G. & Watts, J. Effect of a weak fiber interface coating in ZrB_2 reinforced with long SiC fibers. *Mater. Des.* **88**, 610–618 (2015).
9. Ritchie, R. O. The conflicts between strength and toughness. *Nat. Mater.* **10**, 817–822 (2011).
10. Kelly, A. & Tyson, W. Tensile Fibre-Reinforce and Metals: Copper / Tungsten

and Copper/Molybdenum. *J. Mech. Phys. solids* **13**, 329–350 (1965).
11. Demetriou, M. D. *et al.* A damage-tolerant glass. *Nat. Mater.* **10**, 123–128 (2011).
12. Fahrenholtz, W. G., Hilmas, G. E., Talmy, I. G. & Zaykoski, J. A. Refractory diborides of zirconium and hafnium. *J. Am. Ceram. Soc.* **90**, 1347–1364 (2007).
13. Wang, J., Hu, H., Zhang, Y., Wang, Q. & He, X. Preparation and characterization of C/SiC-ZrB_2 composites via precursor infiltration and pyrolysis process. *Ceram. Trans.* **210**, 467–472 (2010).
14. Yan, C., Liu, R., Zhang, C., Cao, Y. & Wang, Y. Effects of SiC/HfC ratios on the ablation and mechanical properties of 3D Cf/HfC-SiC composites. *J. Eur. Ceram. Soc.* **37**, 2343–2351 (2017).
15. Chen, S., Zhang, C., Zhang, Y. & Hu, H. Influence of pyrocarbon amount in C/C preform on the microstructure and properties of C/ZrC composites prepared via reactive melt infiltration. *Mater. Des.* **58**, 570–576 (2014).
16. Zoli, L., Vinci, A., Galizia, P., Melandri, C. & Sciti, Di. On the thermal shock resistance and mechanical properties of novel unidirectional UHTCMCs for extreme environments. *Sci. Rep.* **8**, 1–9 (2018).
17. Galizia, P., Zoli, L. & Sciti, D. Impact of residual stress on thermal damage accumulation, and Young's modulus of fiber-reinforced ultra-high temperature ceramics. *Mater. Des.* **160**, 803–809 (2018).

6. High entropy dibordies (HEMB) using Arc-melting technique

The aim of this work is to demonstrate the feasibility of high entropy borides (HEB), mixing equimolar composition of HfB_2, ZrB_2, TiB_2, TaB_2 and CrB_2, through the arc-melting technique. Moreover, since this technique allows rapid fabrication of large number of samples, we prepared 6 compositions (one quinary and five quaternaries) to study the effect of each single boride on the formation of HEB solid solutions.

6.1 Microstructural analysis

The produced six compositions are listed in Table 6.1 together with the obtained density and the relative abundance of transition metal diborides detected trough EDS analysis.

Table 6.1 Starting compositions, density values, and quantitative EDS mapping of samples core

			EDS analysis*				
Label	**Starting composition mol%**	**Bulk density g/cm^3**	**Hf**	**Zr**	**Ti**	**Ta**	**Cr**
			mol %				
1 - all	$(Hf_{0.20}, Zr_{0.20}, Ti_{0.20}, Ta_{0.20}, Cr_{0.20})B_2$	7.9 ± 0.2	25	22	23	27	1
2 - CrB_2	$(Hf_{0.25}, Zr_{0.25}, Ti_{0.25}, Ta_{0.25})B_2$	9.3 ± 0.5	27	24	22	25	-
3 - TaB_2	$(Hf_{0.25}, Zr_{0.25}, Ti_{0.25}, Cr_{0.25})B_2$	6.9 ± 0.2	39	30	30	-	1
4 - TiB_2	$(Hf_{0.25}, Zr_{0.25}, Cr_{0.25}, Ta_{0.25})B_2$	9.4 ± 0.2	32	30	-	36	0.8
5 - ZrB_2	$(Hf_{0.25}, Cr_{0.25}, Ti_{0.25}, Ta_{0.25})B_2$	8.5 ± 0.2	37	-	29	31	2
6 - HfB_2	$(Cr_{0.25}, Zr_{0.25}, Ti_{0.25}, Ta_{0.25})B_2$	5.6 ± 0.4	-	33	32	33	1

*error within 3% measured using EDS

Fig. 6.1 shows X-ray diffraction spectra: all samples display the primitive hexagonal unit cell typical of the isomorphous starting diborides. Principal diffractions are usually surrounded by small peaks (< 2% of highest peak, see bottom enlarged spectra below each diffraction pattern), which accounts for phase separation, as discussed in sections 6.4 and 6.4.1.

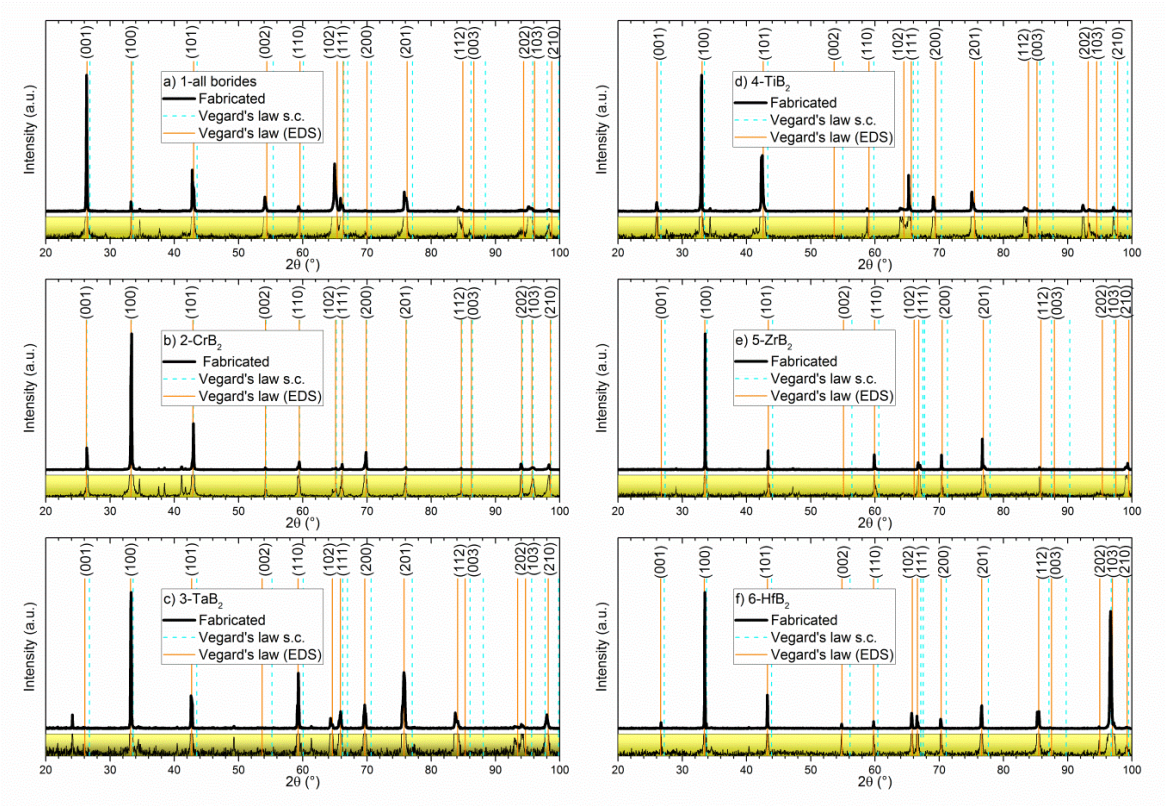

Figure 6.1 Normalized X-ray diffraction patterns for the 6 mixtures and expected peaks' position of high entropy metal diborides (HEMBs) calculated with the Vegard's law considering the starting compositions (s.c.) and the compositions detected by EDS. All scales of the insets zoom range from 0 to 0.02.

Nevertheless, considering main peaks ascribed to hexagonal phase, experimental lattice parameters obtained from XRD patterns are shown in Table 6.2 together with those calculated by means of Vegard's rule [1]. The calculation was done using powder diffraction files (PDF) n. 65-0878, 65-1073, 65-1883, 65-3389, and 65-3387 for TaB_2, TiB_2, CrB_2, HfB_2, ZrB_2, respectively, and the actual atomic percentage obtained using EDS analysis explained below. As it can be seen from Fig. 6.1, the deviation from Vegard's rule is minimized if compositions determined by EDS analysis are taken into account instead of the starting equimolar ones. In Fig. 6.2 we plotted a series of observed lattice parameters of various diborides and binary solid solutions taken from Ref. [2], along with those of the HEBs solutions developed in this work. As can be seen, there is an excellent agreement between a linear interpolation of observed c/a ratio vs. atomic radii of metal atom, r_m and the plotted values, the only unexpected outlier is 3-TaB_2.

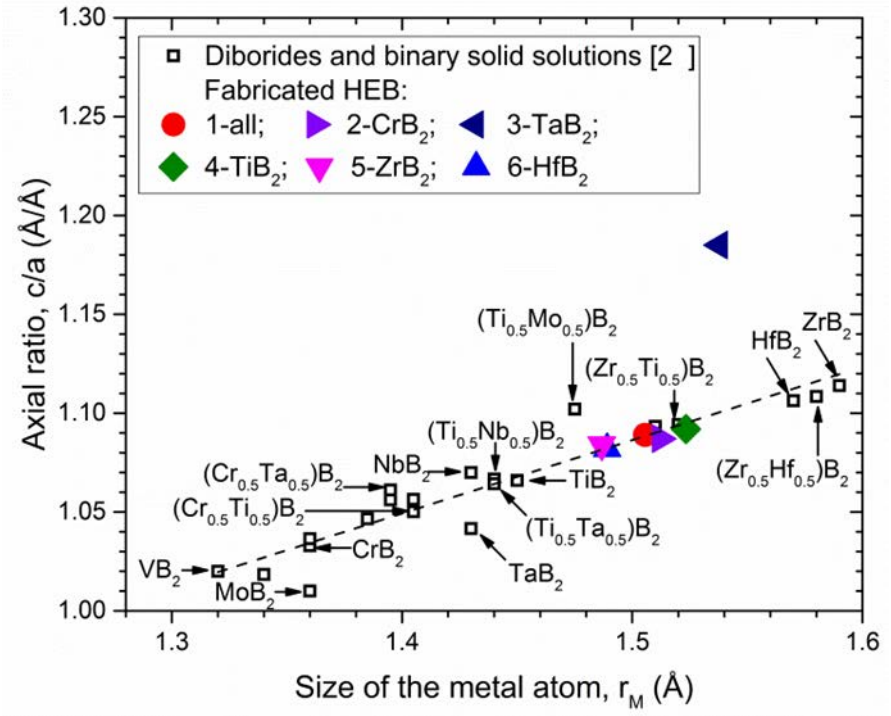

Figure 6.2 Observed tetragonality, c/a ratio, *vs.* atomic radii of metal atom, r_m, for diborides and binary solid solutions taken from Ref. [2], along with those of the high entropy metal diborides (HEBs) developed in this work. The dotted line was obtained by linear fitting (R^2 = 0.90) the values of diborides and binary solid solutions.

The reason for the large deviation (8%) in the length of the *c*-axis is not known, and to date, such anomalies were observed in other studies as well Ref. [2] but no explanation has been found so far. In summary, XRD results suggest that (i) there is a negligible or no amount of Cr in solid solution, and (ii) metal-to-metal replacement to form solid solution occurred readily in the Hf, Zr, Ti, and Ta diborides.

Table 6.2 Lattice constants *a*, and *c* (Å) obtained from observed (100) and (001) peaks, respectively, compared to the one calculated using Vegard's rule and the actual atomic percentage obtained using EDS analysis. *c* values of sample 5 were extrapolated from (101) peak.

Sample	*a* XRD	*a* Vegard	*c* XRD	*c* Vegard	*c/a* XRD	*c/a* Vegard
1- all	3.109	3.102	3.387	3.370	1.089	1.086
2-CrB_2	3.101	3.107	3.372	3.382	1.087	1.089
3-TaB_2	3.107	3.115	3.683	3.413	1.185	1.096
4-TiB_2	3.132	3.125	3.421	3.415	1.092	1.093
5-ZrB_2	3.082	3.085	3.340	3.330	1.084	1.080
6-HfB_2	3.086	3.091	3.338	3.344	1.082	1.082

Fig. 6.3 shows the cross section of the samples obtained from the arc-melting process of the six materials listed in Table 6.1. From SEM analyses of the microstructures it was ascertained that all materials reached a good level of densification, with the exception of 4-TiB_2, (missing TiB_2) that exhibited small distributed porosity in the center and voids in the edges. Bulk densities measured with the Archimede's method (Table 6.1) ranges from 5.6 to 9.4 g/cm^3, depending on the composition and residual porosity. Due to evaporation phenomena and new phase formation during arc-melting (section 3.4), the starting composition was strongly modified, therefore an exact calculation of theoretical and relative densities was not possible.

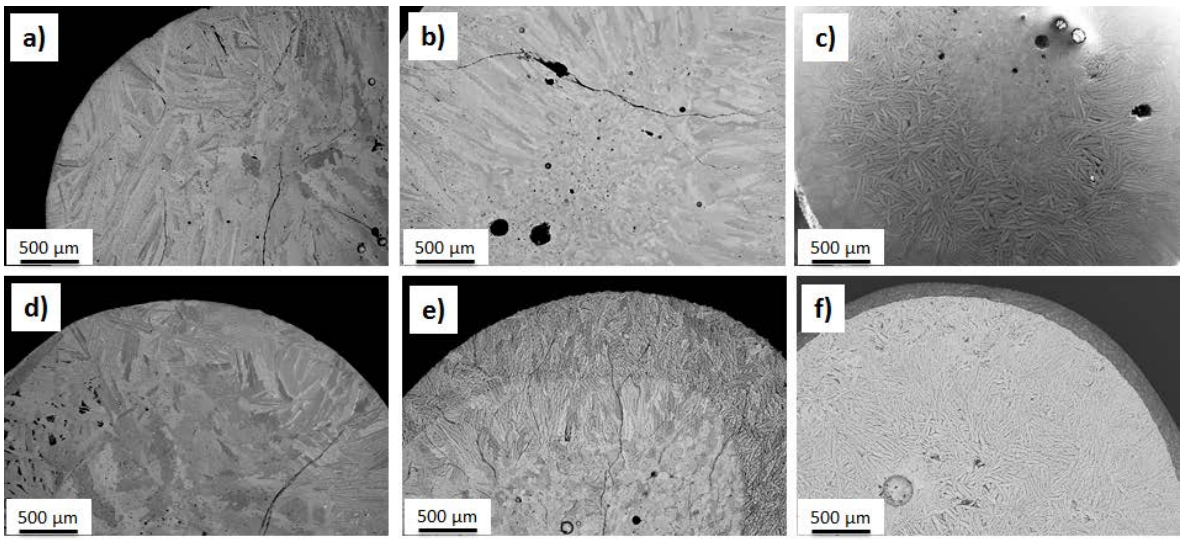

Figure 6.3 Cross section of spherical HEB samples: a) 1- all, b) 2- CrB_2, c) 3- TaB_2, d) 4-TiB_2, e) 5- ZrB_2, f) 6- HfB_2.

Dense specimens were often found to be affected by cracks due to thermal shock/strong temperature gradient experienced during arc-melting treatment. They all exhibited the typical anisotropic microstructure of metallic materials obtained from melting [3,4]. During cooling down, the surface cooled much faster than the core, which generated a strong radial temperature gradient. As a result, an anisotropic structure was created, with rounded/coarsened grains in the (hot) core that gradually changed to elongated and dendritic-like grains towards the rapidly cooling surface. Approximately, the transition from rounded to elongated grains occurred at a distance of 2 mm from the center. According to EDS analyses, a single solid solution phase was detected in the core grains constituting the inner part of the molten samples, in agreement with the phases detected

by X-ray diffraction and in agreement with the large mutual solubility range of diborides observed by other authors [5]. Moreover, grain boundaries were found to be clean in this portion of material, at least at SEM resolution. Shifting from the core to the edge, compositions and morphology of the grains changed and liquid phase separation was observed in the grain boundary regions. In all the compositions containing Cr, this element was preferentially detected along the grain boundaries as a secondary phase, though a tiny percentage was also found in solid solution (see quantitative analyses in Table 6.1). Indeed, observing the EDS compositional maps of sample 1-all ($Hf_{0.20}$, $Zr_{0.20}$, $Ti_{0.20}$, $Ta_{0.20}$, $Cr_{0.20}$)B_2, Fig. 6.4, and except those contain Cr, they presented a quasi-equimolar solid solution of HfB_2, ZrB_2 TiB_2 and TaB_2. This feature is even more evident in sample 2-CrB_2 where CrB_2 was not included the original mixture. Noteworthy, in sample 2-CrB_2 ($Hf_{0.25}$, $Zr_{0.25}$, $Ti_{0.25}$, $Ta_{0.25}$) B_2, missing Cr, Ta segregation between the grains was observed, as shown in Fig. 6.5 b).

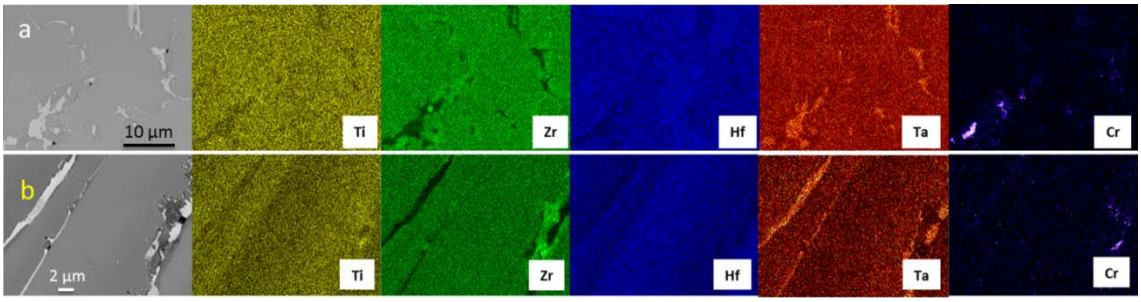

Figure 6.4 EDS compositional maps of a) inner part and b) external part of the sample 1-all b, containing all borides. CrB_2 phase separation was observed, the remaining borides formed a complete solid solution

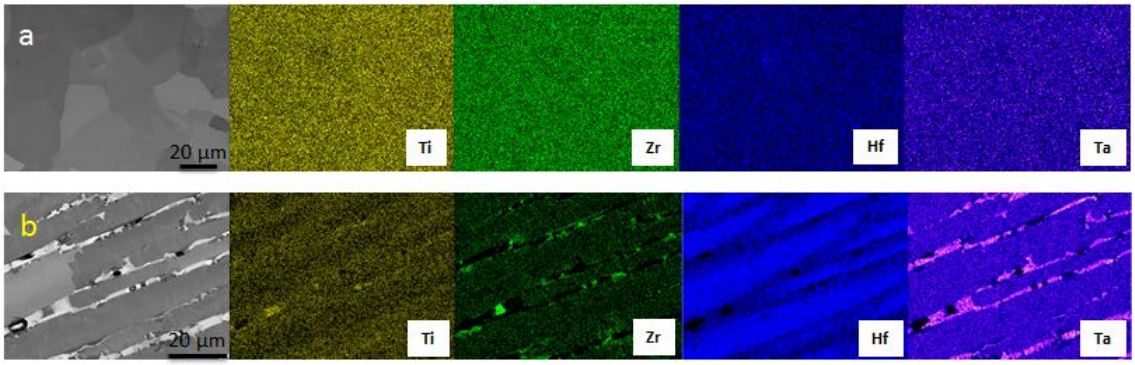

Figure 6.5 EDS compositional maps of a) inner part and b) external part of the sample 2-CrB_2.

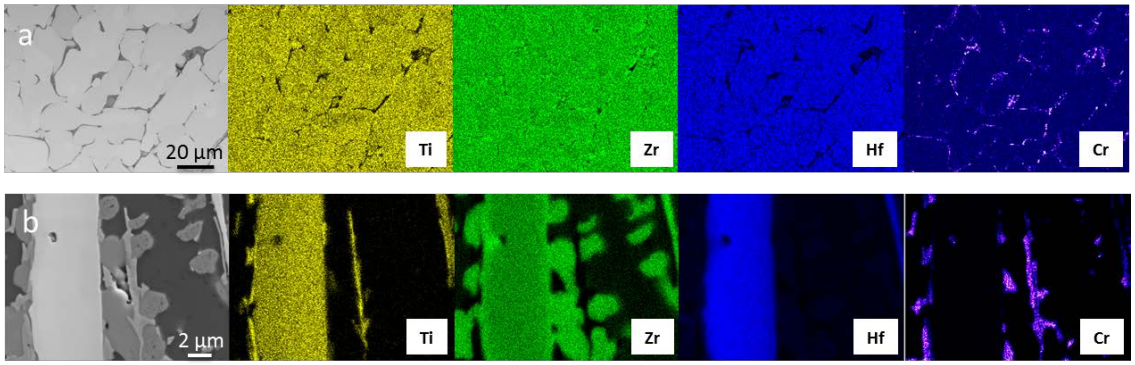

Figure 6.6 EDS compositional maps of a) inner part and b) external part of the sample 3-TaB_2

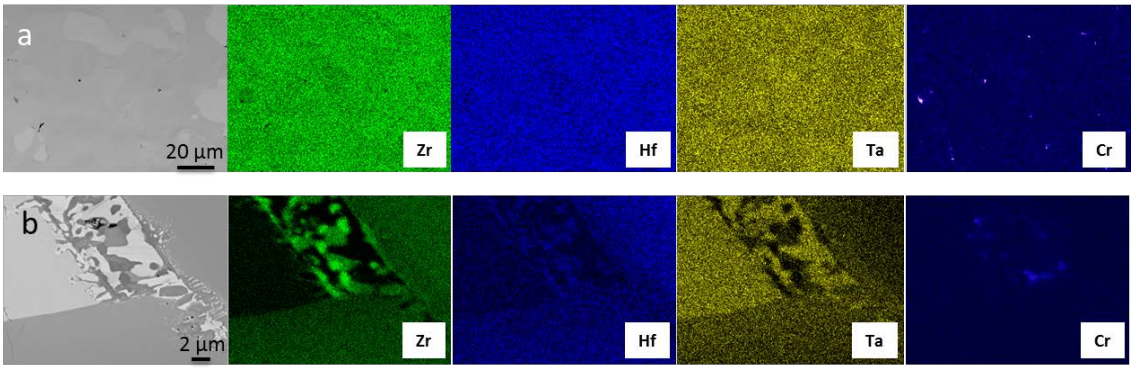

Figure 6.7 EDS compositional maps of a) inner part and b) external part of the sample 4-TiB_2

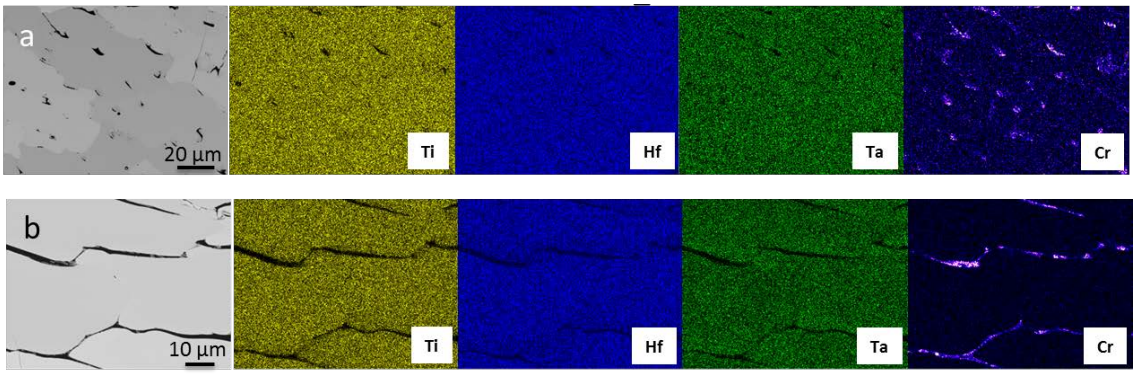

Figure 6.8 EDS compositional maps of a) inner part and b) external part of the sample 5-ZrB_2

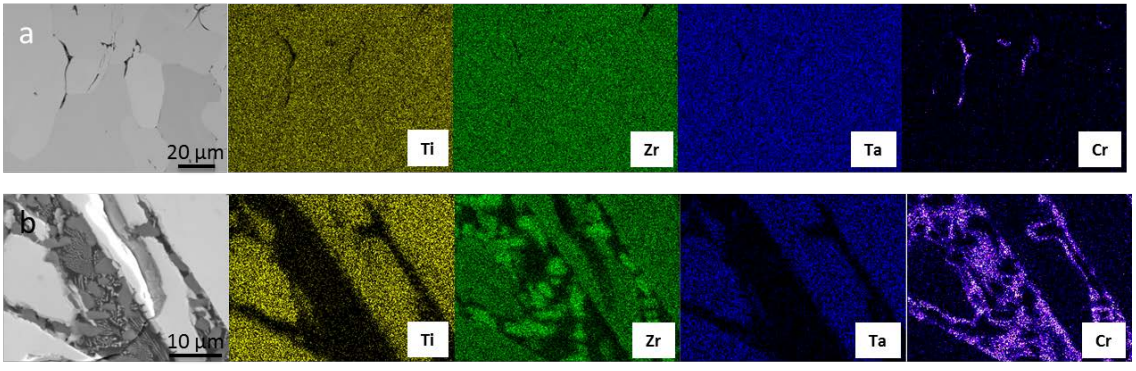

Figure 6.9 EDS compositional maps of a) inner part and b) external part of the sample 6-HfB_2

Sample 3, ($Hf_{0.25}$, $Zr_{0.25}$, $Ti_{0.25}$, $Cr_{0.25}$)B_2, was characterized by a solid solution with almost equal atomic content of Hf, Zr, and Ti, but much smaller content of Cr. Cr was preferentially detected at the grain boundaries. Towards the edge of the pellet, we noticed that elongated grains composed of Hf, Zr, and Ti were surrounded by ZrB_2 rounded agglomerates and CrB_2 phases (see Fig. 6.6 a) and b)). Similarly, sample 4 ($Hf_{0.25}$, $Zr_{0.25}$, $Cr_{0.25}$, $Ta_{0.25}$)B_2, displayed homogeneous distribution of Zr, Hf and Ta element in the center grains, with small segregated CrB_2 – based secondary phases at the grain boundaries On the contrary, going towards the edge, elongated grains were surrounded by mixed secondary phase with irregular morphology (see Fig. 6.7 a) and b)) containing inhomogeneous distribution of Zr, Hf, Ta mainly and Cr in small quantities. Samples 5 ($Hf_{0.25}$, $Cr_{0.25}$, $Ti_{0.25}$, $Ta_{0.25}$)B_2 and 6 ($Cr_{0.25}$, $Zr_{0.25}$, $Ti_{0.25}$, $Ta_{0.25}$)B_2, showed characteristics similar to sample 4 (see Fig. 6.8 a) and b) and Fig. 6.9 a) and b)).

6.2 Sintering behaviour

In their work, Gild et al. [6], demonstrated the formation of a high entropy phase including CrB_2 using the spark plasma sintering technique, despite the limited solid solubility of CrB_2 in both HfB_2 and ZrB_2 [2]. In our case, the formation of high entropy diboride should be easier because, in the molten state, the activation energy for diffusion is much smaller than in the solid state [7]. Compared to the starting compositions we observed a notable reduction of CrB_2 content in all mixtures and of TaB_2 in the case of 2-CrB_2, (e.g. the mixture missing CrB_2). Indeed, we hypothesized that in the arc melting process, formation of solid solutions is not only affected by melting points of each constituent material, but also by their vapor partial pressure. In this work, CrB_2 has the highest vapor partial pressure followed by TaB_2, as shown in Table 7.3. Therefore, in samples containing CrB_2 (1, 3, 4, 5, 6) the peculiar microstructure obtained is affected by the fast vaporization and evaporation of CrB_2 from the center towards the surface. To a lower extent, TaB_2 also experienced the same phenomenon, because of its high vapor partial pressure.

Table 6.3 Physical and chemical properties of metal and metal diborides: crystal structure, melting point (T_m), atomic radius, electronegativity, vapor pressure, lattice parameters

	Cristal structure	T_m	Atomic radius[c]	Electronegativity[d]	Vapor pressure of metal[e]	Lattice parameters [f] MB_2	
		°C	nm		mmHg	a, Å	c, Å
HfB_2		3380[a]	0.159	1.40	8.4×10^{-6}	3.139	3.473
ZrB_2		3245[a]	0.160	1.37	1×10^{-5}	3.170	3.533
TaB_2	hcp	3040[a]	0.146	1.74	5×10^{-3}	3.088	3.241
TiB_2		3225[a]	0.147	1.38	3.5×10^{-3}	3.038	3.220
CrB_2		1900[b]	0.128	1.69	7.4	2.969	3.066

a [8], b [2], c [6], d [9], e [10], f [11]

Broadly, microstructural evolution of compositions containing CrB_2 can be schematized as follows. During heating:

1) at least 2 melts form, with different melting points and composition. Since CrB_2 melting point << other borides, at temperature around 2000°C or below CrB_2 becomes liquid and partially dissolves other borides in the vicinity, forming the L1 liquid phase.

2) As the temperature continues to rise and melting proceeds towards the pellet interior, new L1 liquid phase is formed and evaporation of CrB_2 occurs on the surface.

3) Other molten liquids form (L2, with no CrB_2), with higher melting point than L1.

4) Progressive/fast extension of melting from the surface down to the core and progressive depletion of CrB_2 from the core.

During cooling:

1) the solid solution nuclei from L2 (most refractory) liquid type begin to solidify from the outer surface and grow forming columnar grains that develop in the direction of the temperature gradient present in the sample. These crystalline nuclei are mainly formed by solid solutions of the high melting elements, where HfB_2, ZrB_2, TiB_2 are quasi equimolar whilst TaB_2 is slightly lower due to partial evaporation.
2) CrB_2 vaporization is blocked in the proximity of the outer surface due to rapid closure of exit channels and the CrB_2-liquid phase (L1) remains trapped and solidifies along the grain boundaries, as observed by SEM-EDS.
3) CrB_2 secondary melt separation occurs because of different factors, including its reduced melting point compared to other borides, decreased solubility of other borides when the temperature decreases and extremely fast cooling (≈1000 ˚C/s).

Finally, in sample 2, missing CrB_2, TaB_2 is the lowest melting temperature phase, thus in this case, TaB_2 based liquid phase is formed and phase separation mainly involving TaB_2 occurs during cooling.

Mechanisms occurring during cooling are sketched in Fig. 6.10.

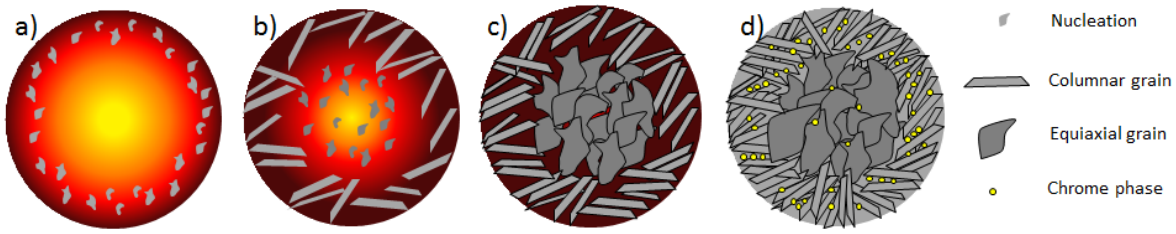

Figure 6.10 Solidification mechanism: a) first formation of crystalline nuclei in the outermost area formed by the high melting elements (HfB_2, ZrB_2, TiB_2, TaB_2), b) nuclei growth forming columnar grains that develop in the direction of the temperature gradient and formation of crystalline nuclei in the central part of the sample c) growth of the equiaxial grains in the innermost area of the material formed by an equimolar solid solution d) precipitation of Cr element among the grain boundary principally in the external part of the sample

Finally, future work is concerned with additional experiments to control the cooling rate. It is expected that producing larger samples has the effect to decrease the cooling rate, limiting or suppressing the formation of a core – shell structure, with the dense equiaxed core and elongated shell grains. This could be achieved by lowering the arc current gradually or using a heated stage.

6.3 Mechanical properties

Indentations were collected indistinctly both in the samples core and close to the sample surface. Values were in the range 19-20 GPa, and slightly increased to 20-23 GPa reducing the load from 1 to 0.5 and 0.2 Kg, as shown in Fig. 6.11 and Table 6.4, mainly due to the indentation size effect [12], [13].

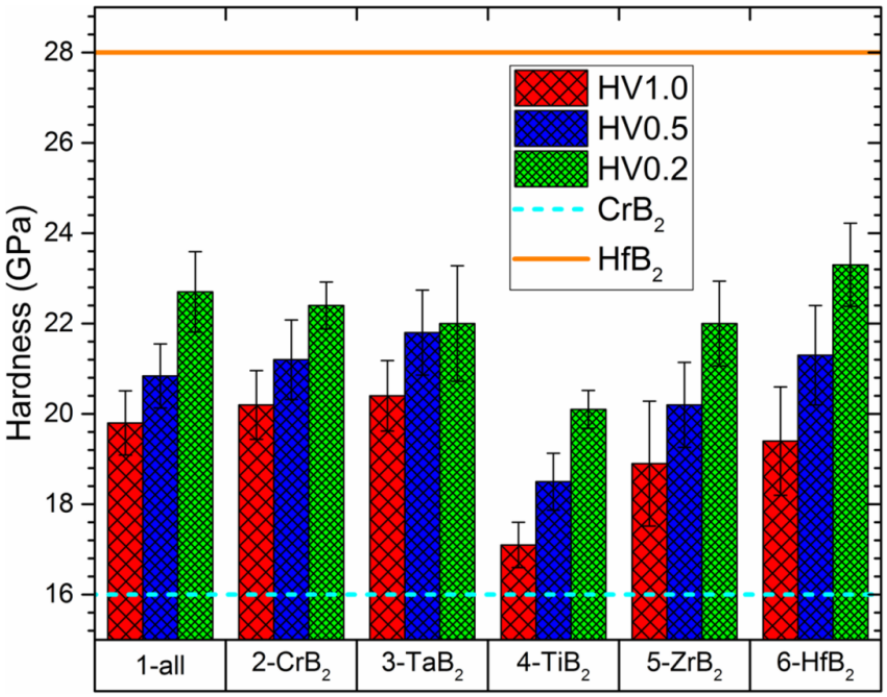

Figure 6.11 Hardness value measured with load 1, 0.5 and 0.2 Kg for quaternary and quinary borides. HfB_2 and CrB_2 lines are the hardest and softest borides as reference materials such indicated by Fahrenholtz et al. (HV1.0) [14] and Wang et al. (HV0.5) [15]

The lowest values were found for the mixture without TiB_2, a feature which can be attributed to residual porosity shown in Fig. 6.3 d). Amongst the other fully dense mixtures, the hardest one was sample 3, missing TaB_2 probably due to its finer microstructure.

Table 6.4 Hardness value obtained with load of 1, 0.5, 0.2 Kg

	Sample	HV GPa	Standard deviation
HV1	1- all	19.8	0.71
	2- CrB_2	20.2	0.76
	3-TaB_2	20.4	0.78
	4- TiB_2	17.1	0.5
	5- ZrB_2	18.9	1.38
	6- HfB_2	19.4	1.2
HV0.5	1- all	20.84	0.71
	2- CrB_2	21.2	0.88
	3-TaB_2	21.8	0.94
	4- TiB_2	18.5	0.63
	5- ZrB_2	20.2	0.94
	6- HfB_2	21.3	1.1
HV0.2	1- all	22.7	0.89
	2- CrB_2	22.4	0.52
	3-TaB_2	22.0	1.28
	4- TiB_2	20.1	0.42
	5- ZrB_2	22.0	0.94
	6- HfB_2	23.3	0.92

6.4 Conclusions

High entropy metal diborides were obtained using the arc-melting technique staring from a powder mixture. HfB_2, ZrB_2, TiB_2 and TaB_2 formed equimolar solid solutions as confirmed by EDS analysis. Unlike solid state processing, the similarity in melting point and vapor partial pressure of each individual diboride is an essential requirement to achieve homogenous samples using arc-melting technique. CrB_2 did not form a solid solution because during processing its low melting point contributed to phase separation while its high vapor partial pressure induced almost complete sublimation. The XRD analysis confirmed that oxide phases were not present and the values of lattice parameters were in agreement with theoretical values. The influence of each element on the hardness values showed no large variations and lowest value was for the sample without TiB_2. The results obtained in this work demonstrates as arc-melting technique could allow a rapid screening of hundreds of high entropy borides compositions avoiding long reaction times needed in solid state processing.

6.5 References

1. Denton, A. R. & Ashcroft, N. W. Vegard's law. *Phys. Rev. A* **43**, (1991).
2. Post, B., Glaser, F. W. & Moskowitz, D. Transition metal diborides. *Acta Metall.* **2**, 20–25 (1954).
3. Biloni, H. & Chalmers, B. Origin of the equiaxed zone in small ingots. *J. Mater. Sci.* **3**, 139–149 (1968).
4. Cole, G. S. Inhomogeneities and their control via solidification. *Metall. Trans.* **2**, 357–370 (1971).
5. Otani, S., Aizawa, T. & Kieda, N. Solid solution ranges of zirconium diboride with other refractory diborides: HfB_2, TiB_2, TaB_2, NbB_2, VB_2 and CrB_2. *J. Alloys Compd.* **475**, 273–275 (2009).
6. Gild, J. *et al.* High-Entropy Metal Diborides: A New Class of High-Entropy Materials and a New Type of Ultrahigh Temperature Ceramics. *Sci. Rep.* **6**, 2–11 (2016).
7. Cahoon, J. R. Modified 'hole' theory for solute impurity diffusion in liquid metals. *Metall. Mater. Trans. A Phys. Metall. Mater. Sci.* **28 A**, 583–593 (1997).
8. Fharenholtz, W. G., Wuchina, E. J., Lee, W. E. & Zhou, Y. *Ultra high temperature ceramics: material for extreme anvironment applications*. **53**, (2014).
9. Watson, R. E. & Bennet, L. H. Transition metals: d- band hybridization, electronegativities and structural stability of intermetallic compounds. *Phys. Rev. B - Condens. Matter Mater. Phys.* **18**, 6439–6449 (1978).
10. Gray, D. E. *American Institute of Physics Handbook*. (1972).
11. Zhou, Y., Xiang, H., Feng, Z. & Li, Z. General Trends in Electronic Structure, Stability, Chemical Bonding and Mechanical Properties of Ultrahigh Temperature Ceramics TMB_2 (TM=transition metal). *J. Mater. Sci. Technol.* **31**, 285–294 (2015).
12. Sangwal, K. Review: Indentation size effect, indentation cracks and microhardness measurement of brittle crystalline solids - some basic concepts and trends. *Cryst. Res. Technol.* **44**, 1019–1037 (2009).
13. Krell, A. A new look at grain size and load effects in the hardness of ceramics. *Mater. Sci. Eng. A* **245**, 277–284 (1998).
14. Fahrenholtz, W. G., Hilmas, G. E., Talmy, I. G. & Zaykoski, J. A. Refractory diborides of zirconium and hafnium. *J. Am. Ceram. Soc.* **90**, 1347–1364 (2007).
15. Wang, S. *et al.* Crystal structures, elastic properties, and hardness of high-pressure synthesized CrB_2 and CrB_4. *J. Superhard Mater.* **36**, 279–287 (2014).

7. Acknowledgements

In primo luogo ringrazio Diletta Sciti per avermi dato la possibilità di intraprendere questo percorso di dottorato. Lei mi ha dato piena fiducia e autonomia nella mia attività di ricerca dandomi sempre ottimi consigli. Ha supportato la mia passione nello studio e utilizzo delle tecniche di sinterizzazione facendomi crescere e affidandomi importanti responsabilità all'interno del nostro gruppo. La ringrazio soprattutto per avermi dato la possibilità di affrontare esperienze di lavoro all'estero che non dimenticherò.

Ringrazio Frédéric Monteverde per avermi assistito prima ancora di iniziare il dottorato di ricerca. Il suo approccio alla ricerca sui materiali ceramici è stato molto utile per me su come affrontare i vari problemi avuti durante il mio Ph.D. alla prime armi con i materiali ceramici UHTC.

Ringrazio Laura Silvestroni per essere stata un'amica e collega con cui potermi confidare sui problemi che ho avuto vivendo lontano da casa. Lei mi ha dato le basi su come sporcarmi le mani in laboratorio e su tutti i trucchi per preparare degli ottimi campioni per le analisi SEM. Mi ha sempre tirato su il morale tenendomi aggiornato su tutte le feste stagionali della Romagna con splendidi artisti musicali e ottimo cibo.

Ringrazio Pietro Galizia per aver revisionato questa tesi dalla prima all’ultima pagina riuscendo a dedicarmi tutto il tempo di cui avevo bisogno. Lo ringrazio per la sua immensa pazienza e precisione nell’aver preso il compito di revisore con molta serietà andando a curare i minimi dettagli di questo manoscritto.

Ringrazio Luca Zoli e Antonio Vinci per i consigli che mi hanno dato da quando ho iniziato a far parte di questo gruppo di ricerca. Li ringrazio per i preziosi consigli su come trattare e lavorare i materiali UHTCMC e per il loro tempo dedicatomi nei momenti di bisogno. La loro esperienza con questi materiali mi ha aiutato nel raggiungere in tempi brevi degli ottimi risultati.

Ringrazio Salvatore Grasso per avermi ospitato nei laboratori e alloggi della Southwest Jiaotong University di Chengdu e di avermi insegnato ad usare tecniche non convenzionali per la produzione dei materiali ceramici UHTC. Lo ringrazio per avermi dato la possibilità di scoprire la cucina e la cultura cinese dello Sichuan. Ringrazio lui, il

professor Chunfeng Hu e tutti i suoi studenti per aver compreso le mie difficoltà in un paese con usi e costumi molto diversi dai miei.

Ringrazio Daniele Dalle Fabbriche per i suoi discorsi da vecchio saggio e per la piena fiducia che ha riposto in me nell'utilizzo dei forni più grandi dell'istituto. Lo ringrazio per essere stato un'ottima guida su come prendersi cura e tenere ordinato un laboratorio di grandi dimensioni.

Ringrazio Cesare Melandri e Claudio Capiani per la disponibilità e il loro supporto in laboratorio. Mi hanno dimostrato come la precisione, l'esperienza e la pratica sono fondamentali per evitare la formazione di possibili difetti durante la produzione, la formatura e la caratterizzazione meccanica dei materiali ceramici.

Ringrazio Carlo Baldisserri per il prezioso supporto teorico e pratico che mi ha dato durante gli esperimenti nella deposizione elettroforetica.

Ringrazio Mauro Mazzocchi per i consigli al SEM e le analisi XRD.

Ringrazio Guia Guarini per le prove di granulometria.

Ringrazio Annalisa per essere ancora accanto a me nonostante le mie numerose esperienze di studio/lavoro a migliaia di chilometri di distanza. Ha sempre capito le mie esigenze e priorità nonostante le sue gravi condizioni di salute che fortunatamente si sono risolte nel migliore dei modi. Grazie a lei sono diventato un esperto nella logistica del trasporto ferroviario e ho capito che 12 ore di treno non sono niente di così terrificante.

Infine ringrazio la mia famiglia che mi ha sempre sostenuto in ogni mia scelta e ogni mia difficoltà non solo in questi tre anni di dottorato ma in questi sette anni lontano da casa. Mi ricordano sempre del posto chiamato "casa" dove posso tornare tutte le volte che ne ho voglia. Grazie a loro spariscono tutti i miei problemi lavorativi e di vita quotidiana e per un attimo posso rivivere la mia vita spensierata che ho lasciato andando via di casa sette anni fa.